2-15-2017

Modeling Enhancement and Intelligent Inference of Impedance-based Structural Health Monitoring

Qi Shuai
qi.shuai@engr.uconn.edu

Modeling Enhancement and Intelligent Inference of Impedance-based Structural Health Monitoring

Qi Shuai, Ph.D.

University of Connecticut, 2017

In impedance-based structural health monitoring, the electrical impedance or admittance of the transducer is coupled with the mechanical property (mass, stiffness and damping) of the monitored structure due to the interaction between multiple physical fields. The changes of local structural properties induced by fault can be reflected in the changes of the impedance or admittance of the transducer. In other words, the impedance changes or admittance changes of the transducer can be used as fault indicator. By comparing and analysing the impedance measurements before and after the fault occurrence, one can also identify the fault location/severity/ type. Recently, the so called electromagnetic acoustic transducer (EMAT) has been explored in the impedance-based fault detection. The coupling between the magnetic transducer and the structure monitored is based upon the interactive magnetic field between the transducer and the induced eddy current in the structure. There is no direct contact between the transducer and the structure. However, the lift-off distance may vary during the fault detection process due to various reasons. The magneto-mechanical interaction is directly related to the lift-off distance. Therefore, it is particularly important to develop an accurate mathematical model of the magnetic transducer that explicitly includes the lift-off distance effect. An important module in an SHM system is decision making. The essence of impedance/admittance-based fault detection is the examination of structural health condition through local, stationary responses, which holds the potential

of direct inverse analysis of structural faults using a first-principle model and online measurements. There are, however, noteworthy challenges in inverse-sensitivity-based fault identification. On one hand, the impedance-based sensing mechanism entertains high sensitivity because of the high-frequency responses induced/measured. On the other hand, high-frequency analysis requires high dimensionality in the model and the subsequent inverse analysis contains a very large number of unknowns which often renders the fault identification problem under-determined. In this dissertation research, the focus is on the enhancement of a promising impedance-based structural health monitoring approach. The electro-magnetic impedance-based fault detection method and the impedance-based fault identification method are both advanced and summarized in this dissertation research.

Modeling Enhancement and Intelligent Inference of Impedance-based Structural Health Monitoring

Qi Shuai

B.S., Chongqing University, 2008

M.S., Chongqing University, 2011

A Dissertation

Submitted in Partial Fulfilment of the

Requirements for the Degree of

Doctor of Philosophy

at the

University of Connecticut

2017

APPROVAL PAGE

Doctor of Philosophy Dissertation

Modeling Enhancement and Intelligent Inference of Impedance-based Structural Health Monitoring

Presented by

Qi Shuai

Major Advisor _____

Dr. Jiong Tang

Associate Advisor _____

Dr. Chengyu Cao

Associate Advisor _____

Dr. Richard Christenson

Associate Advisor _____

Dr. Robert Gao

Associate Advisor _____

Dr. Shinae Jang

University of Connecticut

2017

This work is dedicated to my beloved parents

for the infinite love they devoted to their son.

ACKNOWLEDGEMENT

First and foremost, I would like to express my sincere gratitude and respect to my major academic advisor Professor Jiong Tang. I appreciate his guidance, patience, encouragement, and support for my graduate career. Under the advisement of Professor Tang for almost 5 years, I have learned a lot of useful things that not only benefit my academic research, but also positively affect my attitude towards the challenges and barriers in real life. This is a most rewarding experience, which I will cherish and preserve in my mind.

I also would like to express my gratitude to my associated academic advisors, Professor Chengyu Cao, Professor Richard Christenson, Professor Robert Gao, Professor Shinae Jang, for their precious time serving on my committee. Their keen insight, helpful advice and critiques on my research project give a tremendous value to me throughout my entire graduate study.

I thank the following former and current labmates in the Structure and System Dynamic Research Laboratory, for their support during the time we were together – Kai Zhou, Ji Zhao, Arun Hedge, Jiawen Xu, Pei Cao, Shengli Zhang, David Yoo, Shilong Li, and Yuan Yuan. Also thanks to all my other friends in UConn. The friendship between us will be highly valued.

I would express my greatest gratitude to my parents for their unconditional love and constant support. Finally, I gratefully acknowledge the financial support provided by National Science Foundation and Air Force Office of Scientific Research.

Table of Contents

Chapter 1 Introduction and Research Overview

1.1 Background and State-of-the-Art review

1.1.1 Introduction to impedance-based structural health monitoring

Structural health monitoring (SHM) is a process of implementing fault detection and fault identification strategy for various structures. There are a variety of fault detection methods based on dynamic responses, such as vibration-based method (Naidu and Soh, 2004; Jiang, et al, 2006; Zhao, et al, 2008), wave propagation-based approaches (Giurgiutiu, 2005; Wang et al, 2008; Wandowski et al, 2011; Yu and Giurgiutiu, 2012; Yoon et al, 2012; Koduru and Rose, 2013), impedance-based method (Giurgiutiu, 1999; Park et al, 2008; Wang and Tang, 2010a; Madhav and Kiong, 2010; Zhou and Zuo, 2012; Annamdas and Radhika, 2013), etc. Among them, the impedance-based method has shown some promising aspects, such as easy integration, high detection sensitivity, and large detection/monitoring range (Park et al, 2003). In impedance-based method, the electrical impedance or admittance of the transducer is coupled with the mechanical property (mass, stiffness and damping) of the monitored structure due to the interaction between multiple physical fields, such as the two way electrical-mechanical coupling in the piezoelectric transducer. The changes of local structural properties induced by fault can be reflected in the changes of the impedance or admittance of the transducer. In other words, the impedance changes or admittance changes of the transducer can be used as fault indicator.

An important module in an SHM system is decision making. For impedance-based fault detection, various fault indices built upon the comparisons of measurements before and after fault occurrence have been employed in the past to analyze the fault type/location/severity (Zagrai and Giurgiutiu, 2001; Tseng and Naidu, 2002; Naidu et al, 2006; Min et al, 2012; Wang et al, 2013). These measurement data-based methods only provide phenomenological characterizations of the impedance/admittance changes under specific fault patterns, and oftentimes cannot accurately relate the fault indices to the changes of local

structural properties such as mass, stiffness, and damping ratio, etc (Wang and Tang, 2010b). The essence of impedance-based fault detection is the examination of structural health condition through local, stationary responses, which holds the potential of direct inverse analysis of structural faults using a first-principle model and online measurements. Therefore, alternatively, model-based methods have been formulated that use finite element or spectral element for discretization and employ inverse sensitivity analyses under the stationary condition (Wang and Tang, 2009; Kim and Wang, 2014). These model-based fault identification algorithms can result in the estimation of change of local, element-level structural properties such as mass and stiffness at the element level.

1.1.2 Magnetic impedance-based fault detection

An electrical coil inserted with a permanent magnet can be considered as a magnetic transducer, which is generally referred to as an electromagnetic acoustic transducer (EMAT) (Wilcox et al, 2005; Jian et al, 2006; Thomas et al, 2009). Alternating current flowing through the electrical coil creates a magnetic field. When the coil is placed near a structure made of electrically conductive material, eddy current is induced in the structure because of the time-varying magnetic field of the coil. The coil impedance is in turn influenced by the magnetic field of the eddy current induced. Meanwhile, as the eddy current flows in the static magnetic field of the permanent magnet, a Lorentz force is generated and acts on the structure as an external excitation/actuation. These EMAT-type magnetic transducers can be used as actuators in NDE and structural fault detection, as well as in active damping/control (Sodano et al, 2005; Sodano and Inman, 2008). Recently, the EMAT-type magnetic transducers have been explored in the so-called impedance-based fault detection (Zagrai, 2009), in which they are employed as actuators (to excite the dynamic response in the structure being monitored) and sensors (to sense the change of dynamic response) simultaneously. The impedance of the magnetic transducer is coupled with the structural impedance due to the two-way magneto-mechanical interaction. Qualitatively, the two-way magneto-mechanical interaction in this magnetic impedance method is analogous to the two-way electrical-mechanical coupling in piezoelectric impedance method (Wang and Tang, 2010a). It should be noted that the piezoelectric

transducers employed need to be attached/bonded to the host structure monitored, while the magnetic transducers are non-contact in nature. This non-contact feature can yield advantage in monitoring large-scale structures using only a small number of moveable sensor units. It also yields the possibility of monitoring moving/rotating parts of a structure using a sensory system fixed to the stationary base.

1.1.3 Model-based fault identification

In general, the impedance -based fault identification can be divided into two major categories: data-oriented method and model-based method. In data-oriented algorithms, various fault indices (Raju et al, 1998; Park et al, 1999; Zagrai and Giurgiutiu, 2001; Tseng and Naidu, 2002) and artificial neural networks (Min et al, 2012; Rosado et al, 2013) are frequently used in the classification and identification of fault location/severity/types. These algorithms are mostly based on phenomenological characterization of the impedance signature, and oftentimes cannot accurately relate the fault indices to the changes of local structural properties such as mass, stiffness, and damping ratio, etc. Alternatively, in model-based method, fault identification can be achieved by combining the impedance/admittance signatures with mathematical model of the structure and the sensor (Yong and Hao, 2003; Wang and Tang, 2009). Structural fault can be modeled as the change of a local structural property in the model. In general, the finite element model is widely used in the model based method and the fault is modeled as elemental property changes (elemental stiffness decrease or elemental density increase). A sensitivity matrix is derived to characterize the linearized relationship between the impedance/admittance signatures (e.g., resonant frequencies shift or response amplitudes changes) and the fault index (location and severity). Then the observed impedance/admittance signatures induced by fault are then used as input to an inverse analysis process to predict the unknown fault index. However, the fault identification problem is underdetermined in most cases, since the useful impedance/admittance information are far less than unknowns (Kim and Wang, 2014). Mathematically speaking, there are infinitely many solutions for an underdetermined problem. There are some mathematical methods that may give out one possible solution, such as least squares, singular value decomposition and so on. The solution from these methods maybe mathematically correct,

but no guarantee that is the right result for a specific fault identification case. Some effects have been made to overcome such limitation of the inverse analysis. Tunable inductance is integrated into the piezoelectric transducer circuitry to increase available impedance/admittance measurements (Jiang, et al, 2006, 2008). By tuning the inductance to different values, a family of impedance/admittance information can be obtained. This is helpful to increase the useful impedance/admittance information, but the unknown fault index is still far more than the known inputs. Spectral element model (SEM) is employed to reduce the unknowns since SEM analysis entertains high efficiency in mesh size (Lee et al., 2000; Wang and Tang, 2009). Nevertheless, this method that is strictly subject to wave propagation theory may not be feasible for the structure with complex geometry and boundary.

1.2 Problem Statement

For the magnetic impedance-based fault detection, the coupling between the magnetic transducer and the structure monitored is based upon the interactive magnetic field between the transducer and the induced eddy current in the structure. In other words, there is no direct contact between the transducer and the structure. However, the lift-off distance, i.e., the distance between the transducer and the monitored structure, may vary during the fault detection process either due to the specific sensing scheme or simply due to environmental/operational uncertainty. The magneto-mechanical interaction is directly related to the lift-off distance (Mandache and Lefebvre, 2006; Huang et al, 2009). As explained, the impedance changes of the magnetic transducer are used as the indicator of fault occurrence. However, the lift-off distance variation can also alter the impedance of the transducer, which will be appeared as the noise effect and may bury the impedance changes induced by the fault. Therefore, it is particularly important to develop an accurate mathematical model of the magnetic transducer that explicitly includes the lift-off distance effect, i.e., a model capable of characterizing the transducer-structure interaction under given lift-off distance that can be measured real-time. Indeed, there have been on-going efforts on the mathematical modeling of magneto-mechanical interaction between a magnetic transducer and the structure. In one type of methods, the reciprocity eddy current analysis was performed (Sodano et al, 2005; Sodano and Inman,

2008; Wang and Tang, 2012). In these studies, the magnetic field, the eddy current, the Lorentz force and the varied magnetic flux density in the electrical coil were modeled in detail. However, when the eddy current was analyzed, only the energy dissipated by the resistance of the metallic structure was taken into account. The magnetic energy stored in the structure that was neglected in such analysis actually has considerable influence to the impedance of the magnetic transducer. Experimental data under a given lift-off distance were used to extract the coupling coefficient and then to normalize the computed impedance curve (Wang and Tang, 2011). In another type of methods, the magnetic transducer and the structure monitored were treated as primary and secondary circuits, respectively, and the coupling between them was characterized as the mutual inductance of a voltage transformer (Dominique and Isabelle, 1997; Xu et al, 2010; Zagarai and Hakan, 2010). Typically in these studies, the structural impedance was modeled as a serially connected resistance in the secondary circuit, and the fault was modeled as a change of the equivalent resistance. This transformer model can describe the magneto-mechanical coupling interaction. However, the structural impedance may be overestimated since the eddy current is treated as a lumped parameter that is independent of the spatial coordinates. Moreover, the mutual inductance in this type of methods is extracted from experimental measurement. As can be seen, a common drawback of current modeling methods in relevant studies is that experimental testing is required to extract key parameters. Since these parameters are lift-off distance dependent, a large database would need to be established for a given magnetic transducer, to record these parameters under different lift-off distance values.

Recently, a novel fault identification strategy is proposed, which is based on Bayesian inference framework (Kai, et al, 2014). This proposed algorithm necessitates employing forward analysis-based instead of inverse-based identification procedures. Bayesian inference is a statistical inference method which employ Bays' theorem to update the probability of a hypothesis as more information or evidence is available. Bayesian inference has been widely employed in model updating due to its potential advantages. It can specify the model parameters with prior information in the form of probability density function (PDF), which may be viewed as imposing soft physical constraints to enable a unique and stable solution.

Moreover, this approach allows the computation of any type of statistics of the model parameters to be identified (Antoni, et al, 2011). Several pioneering studies first employed Bayesian probabilistic framework to estimate the model parameters, and clearly demonstrated its applicability for simplified numerical models (Katafygiotis and Beck, 1998a; Katafygiotis and Beck, 1998b). Subsequent research has illustrated the effectiveness of this approach in the field of robust structural health assessment (Katafygiotis, et al, 1998). More recently, a wide range of research tasks utilizing this approach have been explored, such as prognosis of fatigue crack growth, model selection, etc. (Zarate, et al, 2012; Mthembu, et al, 2011). In impedance-based fault identification, the probability density function (PDF) of uncertain model parameters (fault location and fault severity) can be first assumed based on the prior knowledge and engineering judgment, and then can be updated using conditional PDF derived from sets of measured impedance/admittance information based on Bayesian theorem. It is worth noting that, despite its promising attributes, the application of Bayesian inference to impedance based fault identification with finite element discretization remains to be challenging. Bayesian inference is a sampling-based approach, which requires repeated finite element analyses for all possible fault scenarios. Meanwhile, structural fault is continuous in nature. As such, in order to precisely quantify the severity of fault in one single segment, one would need to use a very large number of fault severity levels (Zhou et al, 2014). Combining the large number of fault severity levels with the usually large number of finite elements needed for high-frequency impedance/admittance analysis leads to a very large parameter space, and the computational cost involved for the repeated finite element analyses in this parameter space is simply prohibitive.

1.3 Research Objective and Approach overview

The objective of this dissertation research is on the enhancement of a promising structural heath monitoring approach. Specifically address above issues on the electro-magnetic impedance-based fault detection method and the piezoelectric impedance-based fault identification method. To fulfill the objective, this research is separated into four major sections.

The first research task is to formulate detailed first-principle-based modeling of a magnetic impedance transducer. The objective is to overcome current limitation by developing an accurate mathematical model of the magnetic transducer interacting with the structure, in which the dynamic interaction due to magneto-mechanical coupling is explicitly expressed as a function of the lift-off distance. We specifically study the EMAT-type magnetic transducer employed in impedance-based fault detection. As the lift-off distance between the transducer and the structure can be easily measured in practice, this modeling strategy will provide the predictive capability in model-based fault detection and identification. It will further help elucidate the underlying physics in sensor-structure interaction and yield guidelines for impedance sensor optimization.

The second research task is to explore the possibility of directly compensating the lift-off effect in magnetic impedance measurements by elucidating the intrinsic relation between the magnetic impedance and the lift-off distance. This work is based on the relation between both the imaginary part and real part of the impedance of the magnetic transducer and the lift-off distance, which is explicitly identified in the modeling effort of the first research task. The new method uses a scale factor to transform the transducer impedance. A properly chosen scale factor can make the transformed impedance immune to the lift-off variation. Moreover, it is identified that a constant scale factor can be reached, which makes the compensation procedure simple and efficient.

The third research task is to develop a new approach that can identify structural fault, including its location and severity, by using piezoelectric impedance sensing. The novelty lies in that the fault identification algorithm is built upon the combination of inverse sensitivity formulation and the Bayesian inference technique. Bayesian inference is adopted in the identification procedure to avoid the usual drawback of direct inversion being under-determined and to deal with the inherent noise/uncertainties. A pre-screening scheme, which can drastically reduce the fault parameter space, is devised by taking advantage of the algebraic relation between the sensitivity matrix and the admittance change measurement.

A Bayesian inference approach is then incorporated to pinpoint the fault location and severity with high computational efficiency.

The fourth research task is to enhance the model-based fault identification approach developed in the third task by taking effort to alleviate the influence of the inevitable model error. The novelty lies in that the sensitivity matrix is built upon experimentally measured admittance changes and implemented by the Gaussian process (GP) for regression. First, only a few columns of the sensitivity matrix are experimentally extracted. The Gaussian process is then employed to predict the sensitivity at all possible fault location. Next, Bayesian inference approach is incorporated to pinpoint the fault location and severity by taking advantage of the algebraic relation between the sensitivity matrix and the admittance change measurement. Since no mathematic model is involved in the fault identification procedure, one may not only bypass the onerous job of building an accurately finite element model, but also intuitively avoid the discrepancies between the mathematic model prediction and the experimental measurement.

Chapter 2 Enhanced Modeling of Magnetic Impedance Sensing System for Fault Detection

There has been recent interest in utilizing the magneto-mechanical coupling characteristics of a magnetic transducer to perform impedance-based fault detection of electrically conductive structures. This approach is non-contact in nature, and has potential advantages in many applications. One important parameter in this approach is the lift-off distance, i.e., the distance from the transducer to the structure monitored, the change of which changes the magneto-mechanical coupling. In the past, the magneto-mechanical coupling is extracted completely or partially from experiment in an ad hoc manner. A predictive capability of magneto-mechanical coupling under given lift-off distance would play a significant role in fault detection practice and in sensor design/optimization. In this research, we formulate detailed first-principle-based modeling of a magnetic impedance transducer. In particular, the complete electrical effect of the structure is explicitly taken into consideration. Comprehensive analyses and experiments are carried out, which validate the underlying hypothesis as well as the accuracy of the new model proposed for impedance response prediction.

2.1 Introduction

An electrical coil can be considered as a magnetic transducer, due to the magnetic field it can produce. Such type of magnetic transducers has been applied in non-destructive evaluation (NDE), in which they can facilitate the eddy current testing (ECT) (Hashizume et al, 1992; Auld and Moulder 1999; Javier et al, 2011). Alternating current flowing through the electrical coil creates a magnetic field. When the coil is placed near a structure made of electrically conductive material, eddy current is induced in the structure because of the time-varying magnetic field of the coil. The coil impedance is in turn influenced by the magnetic field of the eddy current induced. Fault conditions, such as cracks, change the eddy current flow, which thus change its magnetic field and eventually affect the coil impedance to reveal the fault occurrence.

The eddy current testing requires point-by-point measurement, as the sensing range is limited to the vicinity of the coil where eddy current is induced. An electrical coil inserted with a permanent magnet forms a different type of magnetic transducer, which is generally referred to as an electromagnetic acoustic transducer (EMAT) (Wilcox et al, 2005; Jian et al, 2006; Thomas et al, 2009). Similar to that in ECT, eddy current is induced when the coil subjected to alternating current is placed near a structure made of electrically conductive material. Meanwhile, as the eddy current flows in the static magnetic field of the permanent magnet, a Lorentz force is generated and acts on the structure as an external excitation/actuation. These EMAT-type magnetic transducers can be used as actuators in NDE and structural fault detection, as well as in active damping/control (Sodano et al, 2005; Sodano and Inman, 2008). For example, when excited in high frequency range, the Lorentz force can induce ultrasonic wave propagation in the structure inspected. The changes in wave propagation pattern, such as wave reflection and mode transformation upon wave passing through the fault sites, can be used as fault indicator. Usually, additional sensors are needed to pick up the information of wave pattern change (Dixon and Palmer, 2004).

Recently, the EMAT-type magnetic transducers have been explored in the so-called impedance-based fault detection (Zagrai, 2009), in which they are employed as actuators (to excite the dynamic response in the structure being monitored) and sensors (to sense the change of dynamic response) simultaneously. Typically, harmonic actuation/excitation is applied in impedance-based fault detection. The physical mechanism of the actuation follows that of a standard EMAT as described above, which is due to the combined effect of the eddy current induced and the static magnetic field of the permanent magnet. The eddy current, meanwhile, generates another magnetic field which influences the magnetic flux density in the electrical coil. The impedance of this magnetic transducer thus includes the electrical information of the structure. Moreover, as the structure vibrates under the aforementioned harmonic Lorentz force, the eddy current will be re-distributed. The magnetic flux density in the electrical coil will vary correspondingly. This means that the impedance of the magnetic transducer also includes the mechanical information of the structure. In other words, the impedance of the magnetic transducer is coupled with the

structural impedance due to the two-way magneto-mechanical interaction. This sensing mechanism is different from that in conventional ECT in which the change of the coil impedance is caused by the change of eddy current flow due to fault condition. In this impedance-based method, the change of the transducer impedance is caused by the fault-induced change of the structural vibratory response. As the Lorentz force can excite structural vibration far away from the transducer vicinity, the impedance-based method has much larger sensing range compared to ECT. Qualitatively, the two-way magneto-mechanical interaction in this magnetic impedance method is analogous to the two-way electrical-mechanical coupling in piezoelectric impedance method (Wang and Tang, 2010a). The class of impedance-based methods has shown promising aspects in fault detection (Giurgiutiu, 1999; Park et al, 2003; Park et al, 2006), including easy integration, high detection sensitivity, and large detection/monitoring range. Latest advancements in these impedance-based methods include the enhancement of detection sensitivity and robustness based on circuitry integration to the transducers (Peairs et al, 2007; Wang and Tang, 2010a; Wang and Tang, 2010b). It should be noted that the piezoelectric transducers employed need to be attached/bonded to the host structure monitored, while the magnetic transducers are non-contact in nature.

Intuitively, the change of the transducer impedance can be used as an indicator to detect whether there is fault occurrence. The impedance change may be further employed in fault identification, i.e., identifying fault location and severity. Fault identification algorithms can generally be classified into two categories: data-oriented and model-based. In data-oriented algorithms, various fault indices (Raju et al, 1998; Park et al, 1999; Zagrai and Giurgiutiu, 2001; Tseng and Naidu, 2002) and artificial neural networks (Min et al, 2012; Rosado et al, 2013) are frequently used in the classification and identification of fault location/severity/types. These algorithms are mostly based on phenomenological characterization of the impedance signature, and oftentimes cannot accurately relate the fault indices to the changes of local structural properties such as mass, stiffness, and damping ratio, etc. Alternatively, in model-based algorithms, fault identification can be realized by correlating the impedance signatures with a first principle-based mathematical model of the structure and the sensor. The fault is generally assumed to cause change

of a local structural property in finite element model or spectral element model (Wang and Tang, 2009). The changes of the impedance signature (e.g., resonant frequencies or response magnitudes) are then used as input to an inverse analysis process to analyze the location and severity of the fault. Obviously, an accurate mathematic model is essential in fault identification. It is worth emphasizing that, as the magnetic transducers feature the non-contact advantage, the lift-off distance, i.e., the distance between the transducer and the structure, may vary during the fault detection process either due to the specific sensing scheme (i.e., movable sensor) or simply due to environmental/operational uncertainty. The magneto-mechanical interaction is directly related to the lift-off distance (Mandache and Lefebvre, 2006; Huang et al, 2009). Therefore, it is particularly important to develop an accurate mathematical model of the magnetic transducer that explicitly includes the lift-off distance effect, i.e., a model capable of characterizing the transducer-structure interaction under given lift-off distance that can be measured real-time.

Indeed, there have been on-going efforts on the mathematical modeling of magneto-mechanical interaction between a magnetic transducer and the structure. In one type of methods, the reciprocity eddy current analysis was performed (Sodano et al, 2005; Sodano and Inman, 2008; Wang and Tang, 2012). In these studies, the magnetic field, the eddy current, the Lorentz force and the varied magnetic flux density in the electrical coil were modeled in detail. However, when the eddy current was analyzed, only the energy dissipated by the resistance of the metallic structure was taken into account. The magnetic energy stored in the structure that was neglected in such analysis actually has considerable influence to the impedance of the magnetic transducer. Experimental data under a given lift-off distance were used to extract the coupling coefficient and then to normalize the computed impedance curve (Wang and Tang, 2011). In another type of methods, the magnetic transducer and the structure monitored were treated as primary and secondary circuits, respectively, and the coupling between them was characterized as the mutual inductance of a voltage transformer (Dominique and Isabelle, 1997; Xu et al, 2010; Zagarai and Hakan, 2010). Typically in these studies, the structural impedance was modeled as a serially connected resistance in the secondary circuit, and the fault was modeled as a change of the equivalent resistance. This transformer model can

describe the magneto-mechanical coupling interaction. However, the structural impedance may be overestimated since the eddy current is treated as a lumped parameter that is independent of the spatial coordinates. Moreover, the mutual inductance in this type of methods is extracted from experimental measurement.

2.2 Research Overview

As can be seen, a common drawback of current modeling methods in relevant studies is that experimental testing is required to extract key parameters. Since these parameters are lift-off distance dependent, a large database would need to be established for a given magnetic transducer, to record these parameters under different lift-off distance values. The objective of this research is to overcome such limitation by developing an accurate mathematical model of the magnetic transducer interacting with the structure, in which the dynamic interaction due to magneto-mechanical coupling is explicitly expressed as a function of the lift-off distance. We specifically study the EMAT-type magnetic transducer employed in impedance-based fault detection. As the lift-off distance between the transducer and the structure can be easily measured in practice, this modeling strategy will provide the predictive capability in model-based fault detection and identification. It will further help elucidate the underlying physics in sensor-structure interaction and yield guidelines for impedance sensor optimization. The rest of this paper is arranged as follows. Section 2.3 provides the detailed modeling formulations concerning the impedance-based fault detection using an EMAT-type magnetic transducer. In both the actuation and sensing analyses, the complete structural impedance information and the spatial-dependency of structural vibratory motion excited are taken into consideration explicitly. While the concept of mutual inductance is employed in analyzing the magneto-mechanical coupling, our key hypothesis here is that the eddy current induced by the coil, that forms closed circular loops in the structure, will act as flowing in fictitious coils embedded in the structure with different radii. This allows us to directly extract the mutual inductance information under any lift-off distance. In Section 2.4, the modeling improvement is validated by experimental study and

highlighted by comparing with traditional eddy current analysis-based modeling. Section 2.5 summarizes the research progress.

2.3 System modeling

To illustrate the modeling formulation, here we consider the setup shown in Figure 2-1. A coil with N turns of wire is placed above a cantilever beam (length l_b, width w_b, thickness t_b) made of aluminum. The wire is winded in p layers along the axial direction of the coil with n turns in each layer. It has an average radius r_M, and the diameter of the copper wire is d_w. A cylindrical permanent magnet (length l_P, radius r_P) is inserted in the center of the coil, which has axial magnetization M_0. The coil and the permanent magnet form an EMAT-type magnetic transducer. The distance between the bottom surface of the coil and the top surface of the cantilever beam is the lift-off distance h. The origin of the coordinate system is located at the geometric center of the bottom surface of the coil, and the x axis and the z axis are in the length direction and the thickness direction of the beam, respectively, as shown in Figure 2-1(b). The relevant parameters of the beam and the transducer are listed in Table 2-1.

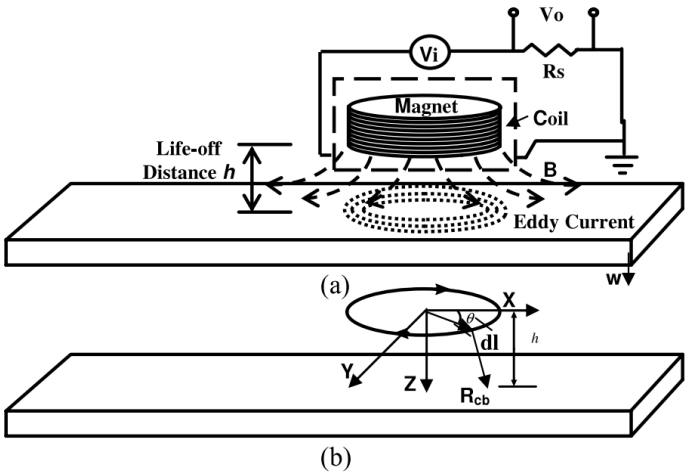

Figure 2-1. Schematic of magnetic transducer: (a) system configuration; (b) coordinate system

2.3.1 Actuation analysis

First, the magnetic transducer is employed as an actuator in the impedance-based fault detection, and therefore is subjected to harmonic voltage excitation. When the harmonic current goes through the electrical coil, a harmonic magnetic field is generated. According to Faraday's law, eddy current $\mathbf{J}$ is

Table 2-1. Material properties and geometric parameters of beam and magnetic transducer

Beam	E_b (Nm^{-2})	ρ_b (kg m^{-3})	σ_b (Sm^{-1})	μ_0 (NA^{-2})	$l_b \times w_b \times t_b$ (mm^3)
Al-2024	73.1×10^9	2780	37.8×10^6	12.56×10^{-7}	$508\times25.4\times3.25$
Coil	r_o (mm)	$n\times p$ ($turns\times layers$)		h (mm)	$r_M \times d_W \times x_M$ (mm^3)
Copper	10	26×384		1	$11.4\times0.04\times403.4$
Magnet	B (Tesla)			$l_P \times r_P$ (mm^2)	
NdFeB	0.6			25×9.5	

induced into the beam underneath the transducer coil. The eddy current can generate a Lorentz force $\mathbf{F}_L$ under the static magnetic field of the permanent magnet (Cheng, 1992).

$$\mathbf{F}_L = \delta(x - x_0)\iiint(\mathbf{J}\times\mathbf{B}_P)dV \tag{2-1}$$

Here the Lorentz force is treated as a point force acting at x_0 which is the location of the center of the eddy current loop, and δ is the Dirac delta function. In this research we consider its vertical component along the z direction, denoted as F_L. As the beam structure considered here is thin and has small width, the induced eddy currents can penetrate the thickness of the beam and cover a circular area with a maximum diameter equal to the beam width. Therefore, the volume of integration in Eq. (2-1) is a cylinder with radius $w_b/2$ and height t_b. $\mathbf{B}_P$ is the static magnetic flux density of the permanent magnet. Since the magnetic field is symmetrical with respect to the z axis, a cylindrical coordinate system (r,θ,z) is used (Figure 2-1(b)). According to Biot-Savart law (Cheng, 1992), for a differential element dz of the magnet along the

z direction, its magnetic flux density at an arbitrary point (r',θ',z') on the beam can be derived as (Cheng, 1992),

$$\mathbf{B}_P'(r',z') = \frac{\mu_0 M_0 dz}{4\pi} \oint \frac{d\mathbf{l}_{Pr} \times \mathbf{R}_{Pb}}{2\|\mathbf{R}_{Pb}\|^3} \tag{2-2}$$

where

$$d\mathbf{l}_{Pr} = -r_P \sin\theta d\theta \mathbf{i} + r_P \cos\theta d\theta \mathbf{j}$$

$$\mathbf{R}_{Pb} = (r'\cos\theta' - r_P\cos\theta)\mathbf{i} + (r'\sin\theta' - r_P\sin\theta)\mathbf{j} + (z'-z)\mathbf{k}$$

Here μ_0 is the vacuum permeability. $d\mathbf{l}_{Pr}$ is a differential element of the circumference of the cylindrical magnet. $\mathbf{R}_{Pb}$ is a vector directed from $d\mathbf{l}_{Pr}$ to the point (r',θ',z') on the beam structure. The magnetic flux density $\mathbf{B}_P$ of the entire permanent magnet can be derived by integrating $\mathbf{B}_P'$ along the z direction from $-l_P$ to 0. Because of the symmetry, the static magnetic flux density $\mathbf{B}_P$ is independent of θ. The static magnetic flux density only includes components in the r and z directions, respectively, which are expressed as

$$B_{Pr}(r',z') = \frac{\mu_0 M_0}{4\pi} \int_{-l_P}^{0} dz \int_0^{2\pi} (z'-z) r_P \cos\theta d\theta / [r'^2 + r_P{}^2 - 2r' r_P \cos\theta + (z'-z)^2]^{\frac{3}{2}} \tag{2-3}$$

$$B_{Pz}(r',z') = \frac{\mu_0 M_0}{4\pi} \int_{-l_P}^{0} dz \int_0^{2\pi} (r_P - r'\cos\theta) r_P d\theta / [r'^2 + r_P{}^2 - 2r' r_P \cos\theta + (z'-z)^2]^{\frac{3}{2}} \tag{2-4}$$

The harmonic Lorentz force excitation leads to the harmonic dynamic response of the beam structure. In general, a structure being monitored is a continuum. Without loss of generality, here we employ the assumed mode method to discretize the continuum into a discrete model (Tang and Wang, 2001). Let $W(x,t)$ be the transversal displacement of the beam which can be expressed as

$$W(x,t) = \sum_{i=1}^{n_m} \phi_i(x) q_i(t) \tag{2-5}$$

where $\phi_i(x)$ is the *i*-th beam vibration mode, and $q_i(t)$ is the corresponding generalized displacement. Impedance-based fault detection is often carried out in frequency ranges around the structural natural frequencies. Around a given natural frequency, the structural vibration is dominated by the specific mode associated with that natural frequency. Thus here we use one vibration mode in Eq. (2-5) for simplicity. Based on Hamilton's principle, the equation of motion of the beam structure can be obtained as (Tang and Wang, 2001)

$$m\ddot{q} + c\dot{q} + kq = f_L \tag{2-6}$$

where

$$m = \int_0^{l_b} \rho_b t_b w_b \phi(x)^2 dx, \quad c = \int_0^{l_b} c_b \phi(x)^2 dx, \quad k = \int_0^{l_b} E_b I_b [\phi(x)"]^2 dx \tag{2-7}$$

$$f_L = \int_0^{l_b} F_L \phi(x) dx \tag{2-8}$$

m, c, and k are the equivalent mass, damping, and stiffness corresponding to the vibration mode of interest, respectively. f_L is the generalized Lorentz force corresponding to the specific vibration mode. ρ_b is the mass density of the beam structure, c_b is the uniform damping constant, E_b is the Young's modulus, and I_b is the moment of inertia.

From Eq. (2-1), we know that the Lorentz force is related to the eddy current $\mathbf{J}$. The analysis of the eddy current is explained in the next sub-section.

2.3.2 Sensing analysis

The magnetic transducer is simultaneously used as a sensing element. The mutual effect between the electrical coil and the eddy currents can be treated as a mutual inductance between the primary circuit and the secondary circuit in a voltage transformer. According to Biot-Savart law (Cheng, 1992), the induced eddy currents will form closed circular loops in the structure. The time-varying magnetic field that causes

the eddy current has spatial-dependency and thus is a continuous function of the spatial coordinates. According to Faraday's Law, the induced eddy currents are continuously distributed in the structure, and in our case cover a cylindrical volume with radius and height . As the magnetic flux encircled by an eddy current loop changes with the loop radius, the eddy currents are not uniform in the beam structure.

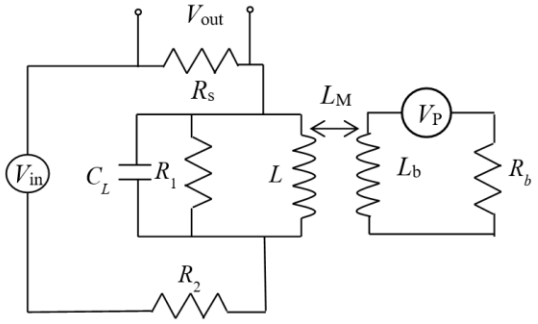

Figure 2-2. Equivalent circuit of the transducer-structure coupled system

Here we assume that there exists a group of fictitious coils within the structure with continuously varying radius and each coil has one turn. The wires that form these fictitious coils have infinitesimally small cross section, and there is no mutual influence between these eddy current coils. In such a situation, a voltage transformer model shown in Figure 2-2 can be used to characterize the magnetic sensing system. The left circuit is the primary circuit that represents the electrical coil of the magnetic transducer. Electrically, the coil has inherent inductance L, parasitic capacitance C_L and parasitic resistance. R_1 is the equivalent resistance that represents the magnetic loss of the inductor core, and R_2 is the resistance of the wire. This circuitry configuration has been used in previous studies to characterize the dynamics of the coil with a core (Brauer, 2006). As will be indicated in Section 4, our experiment on the magnetic transducer employed in this research confirms that this equivalent circuit can accurately reflect the electrical

behavior of the magnetic transducer under the stand-alone status. R_s is a small resistance used to experimentally extract the current information ($I = V_{out} / R_s$) in the primary circuit.

The right circuit shown in Figure 2-2 is the secondary circuit that represents one of the aforementioned fictitious coils. Without loss of generality, here we choose an arbitrary fictitious coil for illustration, which has radius r_f and cross sectional area $drdz$. R_{bi} is the resistance of the coil, and L_{bi} is its inductance. Due to the time-varying magnetic field of the primary circuit, a voltage is induced in the secondary circuit,

$$V_{Lbi} = L_{Mi}\dot{I} - L_{bi}\dot{J}_i = V_{Pi} + R_{bi}J_i \tag{2-9}$$

$$V_{Pi} = \oint (\dot{W} \times \mathbf{B}_P) \cdot d\mathbf{l} = \oint \phi(x) B_{Pr} dl \cdot \dot{q} \tag{2-10}$$

where V_{Pi} is due to the electrical field induced by the structural vibration under the static magnetic field $\mathbf{B}_P$, $\dot{W}$ is the velocity of the beam, and $d\hat{l}$ is a differential element of the fictitious coil. Eq. (2-10) indicates that the mechanical impedance of the structure is coupled with the electrical property of the structure. L_{bi} is the inductance of the fictitious coil. For a single turn coil, its inductance can be derived as (Cheng, 1992),

$$L_{bi} = \iint [\frac{\mu_0}{4\pi} \int_0^{2\pi} (\frac{{r_f}^2 - r_f r\cos\theta}{r^2 + {r_f}^2 - 2r_f r\cos\theta}) d\theta] ds \tag{2-11}$$

where ds is a differential element of the area encircled by the fictitious coil. According to Ohm's law, the resistance R_{bi} is,

$$R_{bi} = \frac{2\pi r_f}{\sigma drdz} \tag{2-12}$$

In Eq. (2-12), σ is the conductivity of the material (i.e., aluminum in this research). For the mutual inductance L_{Mi} between the electrical coil of the magnetic transducer and the fictitious coil, we can first derive the magnetic field generated by the electrical coil as (Cheng, 1992),

$$\mathbf{B}_c(r,z,t) = \sum_{kc=1}^{p} n \frac{\mu_0 I}{4\pi} \oint \frac{d\mathbf{l}_c \times \mathbf{R}_{cb}}{\left\|\mathbf{R}_{cb}\right\|^3} \tag{2-13}$$

where

$$\mathbf{R}_{cb} = (r'\cos\theta' - r_M \cos\theta)\mathbf{i} + (r'\sin\theta' - r_M \sin\theta)\mathbf{j} + (z' + kc \cdot d_w)\mathbf{k} \tag{2-14}$$

$$d\mathbf{l}_c = -r_M \sin\theta d\theta \mathbf{i} + r_M \cos\theta d\theta \mathbf{j} \tag{2-15}$$

p is the number of layers of the wire winded, and n is the number of turns in each layer. $d\mathbf{l}_c$ is a differential element of one turn of wire in the *kc*-th coil layer. $\mathbf{R}_{cb}$ is the distance between $d\mathbf{l}_c$ and an arbitrary point (r', θ', z') of the beam structure. It is worth mentioning that the z components of $\mathbf{R}_{cb}$ are different for coils in different layers, and therefore $\mathbf{R}_{cb}$ is indeed a function of the layer number *kc* (shown in Eqs. (2-13) and (2-14)). I is the excitation current. Similar to the static magnetic flux density $\mathbf{B}_P$, the harmonic magnetic flux $\mathbf{B}_c$ is independent of θ'. We therefore obtain the components of $\mathbf{B}_c$ in the r and z directions, respectively,

$$B_{cr}(r,z) = \sum_{kc=1}^{p} n \frac{\mu_0 I}{4\pi} \int_0^{2\pi} (z' + kc \cdot d_w) r_M \cos\theta d\theta / [r'^2 + {r_M}^2 - 2r' r_M \cos\theta + (z' + kc \cdot d_w)^2]^{\frac{3}{2}} \tag{2-16}$$

$$B_{cz}(r,z) = \sum_{kc=1}^{p} n \frac{\mu_0 I}{4\pi} \int_0^{2\pi} (r_M - r'\cos\theta) r_M d\theta / [r'^2 + {r_M}^2 - 2r' r_M \cos\theta + (z' + kc \cdot d_w)^2]^{\frac{3}{2}} \tag{2-17}$$

Based upon the definition of the mutual inductance (Cheng, 1992), we obtain

$$L_{Mi} = \iint \mathbf{B}_c \cdot d\mathbf{s} / I \tag{2-18}$$

As the lift-off distance increases, the coordinate z' will also increase. Correspondingly, the magnetic flux density in the structure decreases, and the mutual inductance also decreases.

Under harmonic excitation at frequency ω, from Eqs. (2-9) and (2-10) we can obtain the magnitude of eddy current flow in the fictitious coil as:

$$\bar{J}_i = \frac{L_{Mi}}{L_{bi}\omega j + R_{bi}} j\omega\bar{I} - \frac{\oint \phi(x) B_{Pr} dl}{L_{bi}\omega j + R_{bi}} j\omega\bar{q} \tag{2-19}$$

Hereafter the bar notation is used to indicate Laplace/frequency domain quantities, and $j = \sqrt{-1}$. In a previous study (Wang and Tang, 2012), while the resistance R_{bi} of the structure was considered in the modeling and analysis, the inductance L_{bi} was neglected. In general, neglecting the inductance part will overestimate the eddy current, which eventually leads to overestimating the coupling strength.

The above derivation is applied to all fictitious coils to obtain the eddy currents. As explained, the eddy currents are continuous functions of r and z. Recall the force expression given in Eq. (2-8) and the Lorentz force expression given in Eq. (2-1). The magnitude of Lorentz force applied to the beam can be obtained as

$$\bar{f}_L = k_1 j\omega\bar{I} + k_2 j\omega\bar{q} \tag{2-20}$$

where we define

$$k_1 = \int_0^{l_b} \delta(x - x_0) \iiint \left(\frac{L_{Mi}}{L_b\omega j + R_b} B_{Pr}\right) dV \phi(x) dx$$

$$k_2 = \int_0^{l_b} \delta(x - x_0) \iiint \left(-\frac{\oint \phi(x) B_{Pr} dl}{L_b\omega j + R_b} B_{Pr}\right) dV \phi(x) dx$$

Once the Lorentz force is derived, the dynamic response of the beam structure can be obtained based on Eq. (2-6). The magnitude of the displacement is

$$\bar{q} = \frac{k_1 j\omega\bar{I}}{-m\omega^2 + j\omega c + k - j\omega k_2} \tag{2-21}$$

Finally, we can derive the expression of the eddy current magnitude,

$$\bar{J}_i = \frac{L_{Mi}}{L_{bi}\omega j + R_{bi}} j\omega\bar{I} + \frac{\oint \phi(x) B_{Pr} dl}{L_{bi}\omega j + R_{bi}} \frac{k_1}{-m\omega^2 + j\omega c + k - j\omega k_2} \omega^2\bar{I} \tag{2-22}$$

The eddy currents J_i in turn generate a magnetic field that will affect the magnetic field inside the electrical coil and eventually affect the output voltage of the magnetic transducer. In the voltage transformer model, this process is characterized by the mutual inductance between the primary circuit and the secondary circuit. The output voltage is

$$V_L = L\dot{I} - \iint L_{Mi}\dot{J}_i drdz \tag{2-23}$$

In Eq. (2-23), the integration represents taking summation of the magnetic effect of all the eddy currents in the cylindrical volume formed by the fictitious coils. We now consider the electrical property of the magnetic transducer, and observe Figure 2-2. The magnetic transducer has inherent inductance L, parasitic capacitance C_L and parasitic resistance R_1 which are in parallel. The wire has resistance R_2 that is in series with the coil. We can then derive the impedance of the transducer as

$$Z = \frac{1}{1/Z_L + 1/R_1 + \omega j / k_C} + R_2$$

which further yields

$$Z = \frac{Z_L k_c R_1}{k_c R_1 + Z_L k_c + j\omega Z_L R_1} + R_2 \tag{2-24}$$

where

$$Z_L = \frac{\bar{V}_L}{\bar{I}} = L\omega j + P_1\omega^2 - P_2\omega j \frac{k_1\omega^2}{-m\omega^2 + j\omega c + k - j\omega k_2} \tag{2-25}$$

In Eq. (2-25) we have defined

$$P_1 = \iint \frac{{L_{Mi}}^2}{L_{bi}\omega j + R_{bi}} drdz\,, \qquad P_2 = \iint L_{Mi} \frac{\oint \phi(x) B_{Pr} dl}{L_{bi}\omega j + R_{bi}} drdz$$

Here k_C is the inverse of the parasitic capacitance C_L. We can observe that the output voltage is not only related to the electrical properties (as P_1 and P_2 are functions of the inductance L_{bi} and resistance R_{bi} of

the fictitious coil in the structure), it is also related to the mechanical impedance of the structure (i.e., the last term in Eq. (2-25)). This allows us to use the impedance measurement of the magnetic transducer to infer the health status of the structure excited/monitored.

2.4 Comparison and Validation

In this section, the enhancement of the new model proposed in this research is validated by experimental investigations and further highlighted by comparing with an existing model. In structural fault detection using impedance measurement, the change of impedance due to fault occurrence is most observable around the resonant peaks, e.g., shift of peak frequency and/or change of peak amplitude due to fault occurrence. As such change is usually employed as fault indicator in practice, the accurate prediction of the baseline characteristics has obvious significance. We therefore focus our attention on the peak frequency/magnitude in the impedance versus excitation frequency curve.

In order to facilitate the correlation of analytical/numerical results and experimental results, the setup of the experiment is consistent with that employed in the preceding section (Figure 2-1). The geometrical and material properties of the magnetic transducer and the beam structure are listed in Table 2-1. To extract experimentally the impedance of the magnetic transducer, a small resistor R_s (100 Ω) is used to measure the voltage drop across it (Figure 2-2), and thus the electrical current in the circuit can be obtained which then yields the impedance information. A signal analyzer (Agilent 35670A) with a source channel and the sweep sine capability is employed. The source channel is used to generate the sinusoidal voltage V_{in} sent to the magnetic transducer, and the output voltage across the resistor V_{out} is recorded. Therefore, the experimentally exacted impedance is given as

$$Z_{\text{exp}} = \frac{V_{\text{in}}}{I} = \frac{V_{\text{in}}}{V_{\text{out}}} R_s \tag{2-26}$$

Table 2-2. Electrical parameters of magnetic transducer

L	C_L	R_1	R_2
1.995 H	0.1977 nF	251.4 kΩ	11.11 kΩ

Before they are coupled together, both the magnetic transducer and the beam monitored have their respective resonant frequencies. For the magnetic transducer studied in this research, the coil inductance, the parasitic capacitance and the parasitic resistance are extracted experimentally and listed in Table 2-2. Indeed, under the assumed equivalent circuitry configuration shown in Figure 2-2, we can directly solve the values of the respective circuitry elements by using the experimental impedance curve. Simple simulation using the circuitry element values obtained in such a manner shows that this circuitry model can reflect the transducer characteristics under the stand alone status very well. Owing to the parasitic capacitance and the coil inductance, the stand-alone magnetic transducer has an undamped natural frequency that is equal to $\sqrt{k_C / L}$, i.e., 8035 Hz for the magnetic transducer studied. Meanwhile, we use the assumed-mode method to discretize the beam. In order to effectively detect/identify small-sized fault, generally we need to extract the impedance information in relatively high frequency range. Without loss of generality, here we mainly consider the 9th transversal vibration mode of the beam, and the corresponding undamped natural frequency for the beam studied in this research is calculated as 2066 Hz.

We now analyze the coupled dynamic characteristics of the magnetic transducer and the beam monitored, i.e., placing the magnetic transducer on top of the beam structure (Figure 2-1) in both numerical analysis and in actual experiment. Based upon the new model proposed, the impedance of the magnetic transducer coupled with the beam structure is given by Eq. (2-24). Figure 2-3 shows the impedance curves computed (using parameters given in Table 2-1) under 3 different lift-off distances, 1 mm, 3 mm, and 5 mm. Apparently, each curve has two distinct peaks. Figure 2-4 shows the zoom-in view of the first peaks. The frequencies of the first peaks are all close to the 9th undamped natural frequency of the beam (2066 Hz). This indicates that the beam resonant effect can be observed from the magnetic impedance curve owing to the two-way magneto-mechanical coupling between the transducer and the structure. Observe

Eqs. (2-24) and (2-25). The last term in Eq. (2-25) is the contribution of the mechanical impedance. Corresponding to this term, similar to Wang and Tang (2012) we can then define a coupling coefficient K_M,

$$K_M = P_2 k_1 = \iint (L_{Mi} \frac{\oint \phi(x) B_{Pr} dl}{L_{bi}\omega j + R_{bi}}) dr dz \iiint (\frac{L_{Mi}}{L_{bi}\omega j + R_b} B_{Pr}) dV \tag{2-27}$$

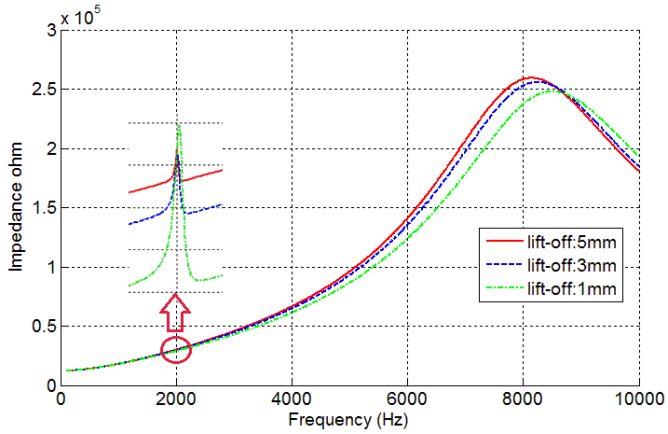

Figure 2-3. Numerical prediction of the impedance of the magnetic transducer using the proposed model

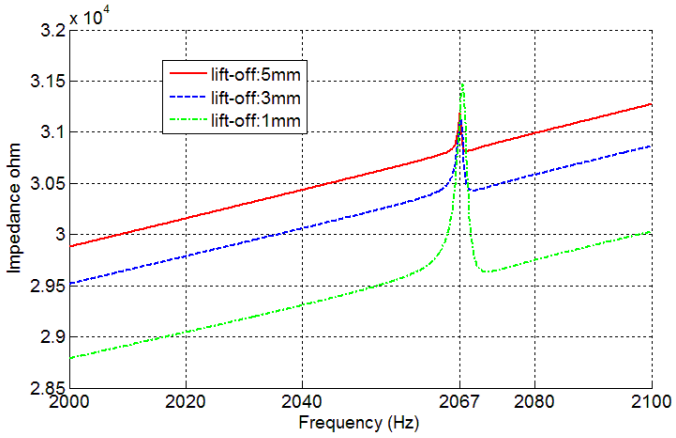

Figure 2-4. Numerical prediction of the impedance of the magnetic transducer using the proposed model: results around the first peak

Recall Eq. (2-18). When one moves the magnetic transducer closer to the beam and thus the lift-off distance decreases, the mutual inductance L_{Mi} increases and so does the coupling coefficient given by Eq. (2-27). As the increase of the mutual inductance reduces the apparent inductance of the magnetic transducer, the off-peak impedance (i.e., the impedance away from resonant peaks) generally decreases (Figure 2-4). Meanwhile, as the coupling increases, the contribution of the mechanical impedance to the transducer impedance becomes more significant. From Figure 2-4 one can observe that the relative peak in the impedance curve, i.e., the resonant peak (due to mechanical resonance) with respect to the off-peak impedance, increases consequently. The peak frequencies become lower and farther away from the beam natural frequency, as the lift-off distance increases

Table 2-3. Impedance peak frequencies corresponding to the first ten beam modes

	1st	2nd	3rd	4th	5th	6th	7th	8th	9th	10th
Numerical results (Hz)	10.21	64.30	178.8	350.1	579.0	865.4	1208.4	1609.2	2066	2581.9
Experiment results (Hz)		61.88	173.3	343.0	562.5	841	1175.25	1582.5	2046.5	2576.5

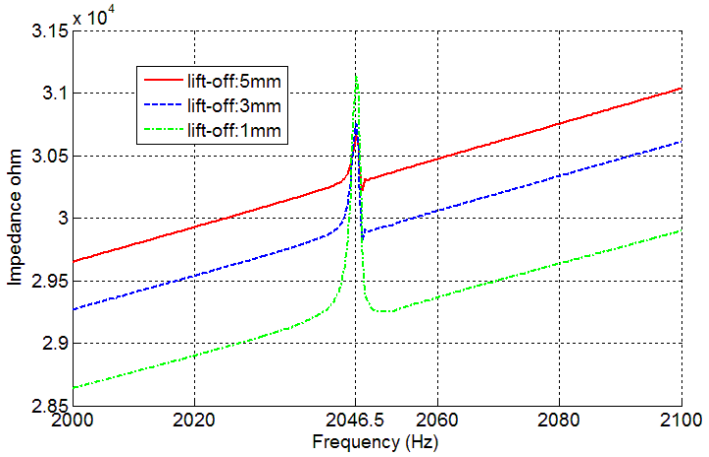

Figure 2-5. Experimental results of the impedance of the magnetic transducer around the first peak

Figure 2-5 shows the experimental results of impedance measurement in the frequency range around the above-mentioned 9th undamped natural frequency of the beam. The results have very good agreement with those from the model prediction (Figure 2-4). The peak frequencies under different lift-off distances are slightly lower than the numerical results but follow the same trend. Indeed, we have performed experiments and numerical simulations of the coupled beam-transducer system for the first ten beam modes under 3 mm lift-off distance. The peak frequencies due to beam resonance (i.e., the peak frequencies in the impedance curves) are listed in Table 2-3 for comparison. The two sets of results are very close to each other, and the experimental results are generally slightly lower than the numerical results, most likely due to the imperfect boundary conditions in the experiment. In Figure 2-5, the experimentally extracted off-peak impedance decreases while the relative peak increases, as the lift-off distance decreases, which matches well with the numerical predictions. Table 2-4 gives the comparison of the relative peak impedance values, in which the errors between the model and experiment are smaller than 5%.

To highlight the model improvement, here we also plot the results of the first peaks obtained by using the eddy current modeling by Wang and Tang (2012). In that model, only the resistance of the beam is taken into account, and the inductance of the beam is neglected. If we directly use such model under various lift-off distances, as shown in Figure 2-6 we can observe that there is no apparent difference in the off-peak impedances as the lift-off distance changes. Furthermore, since the beam inductance is neglected, the coupling coefficient in that model is larger than the one obtained from this research (Eq. (2-27)). As a result, the relative peak impedance values are larger than the actual experimental values. As suggested (Wang, 2010; Wang and Tang, 2012), one way to address this issue is to experimentally measure the impedance curves; the impedance peaks under structural resonances can then be used to extract the magneto-mechanical coupling coefficient, and the off-peak impedance values can be used to extract/calibrate the apparent inductance of the transducer. This procedure, however, has to be conducted for all possible lift-off distances for the same structure monitored. Moreover, as the apparent inductance and the magneto-mechanical coupling are both dependent upon the specific structure, one would need to

carry out such calibration for all different structures monitored. Obviously, these modeling limitations have been effectively overcome by the proposed new model.

Table 2-4. Relative peak values of the first peak under different lift-off distances

	Lift-off 5mm	Lift-off 3mm	Lift-off 1mm
Numerical results (kΩ)	0.38	0.74	1.83
Experiment results (kΩ)	0.40	0.78	1.89

We then investigate the second peak frequencies shown in Figure 2-3 that are obtained by numerical simulation based on the proposed model. While the peaks are not sharp due to the transducer resistance, these peak frequencies are generally close to the undamped natural frequency of the transducer when it is stand-alone (i.e., 8035 Hz), which indicates that these peaks are due to the transducer resonance. When the lift-off distance decreases and thus the mutual inductance L_{Mi} increases, the apparent inductance of the magnetic transducer decreases, and consequently the overall impedance curve becomes lower while the peak frequency becomes larger. The peak frequencies and the impedance peak values under different lift-off distances are listed in Tables 2-5 and 2-6, respectively.

Table 2-5. Second peak frequencies under different lift-off distances

	Lift-off ∞	Lift-off 5mm	Lift-off 3mm	Lift-off 1mm
Numerical results	8035 Hz	8144 Hz	8255 Hz	8401 Hz
Experiment results	8035 Hz	8175 Hz	8270 Hz	8414 Hz

Table 2-6. Second peak values under different lift-off distances

	Lift-off ∞	Lift-off 5mm	Lift-off 3mm	Lift-off 1mm
Numerical results (kΩ)	263.5	259.2	257.6	252.1
Experiment results (kΩ)	263.5	258.8	256.1	250.6

Figure 2-7 shows the experimental results of the second peaks under various lift-off distances. For comparison, the impedance curve of the stand-alone magnetic transducer is also plotted. As the lift-off distance decreases from ∞ (i.e., the magnetic transducer being stand-alone) to 1mm, the peak frequency increases from 8035 Hz to 8414 Hz. Meanwhile, the impedance peaks decrease from $263.5\ \text{k}\Omega$ to $250.6\ \text{k}\Omega$. Comparison of Figure 2-7 and Figure 2-3 shows that the numerical predictions based on the proposed model have very good agreement with the experimental results. The experimental peak frequencies and peak values are also listed in Tables 2-5 and 2-6. The errors in peak frequencies are less than 0.5%, and those in peak values are less than 3%.

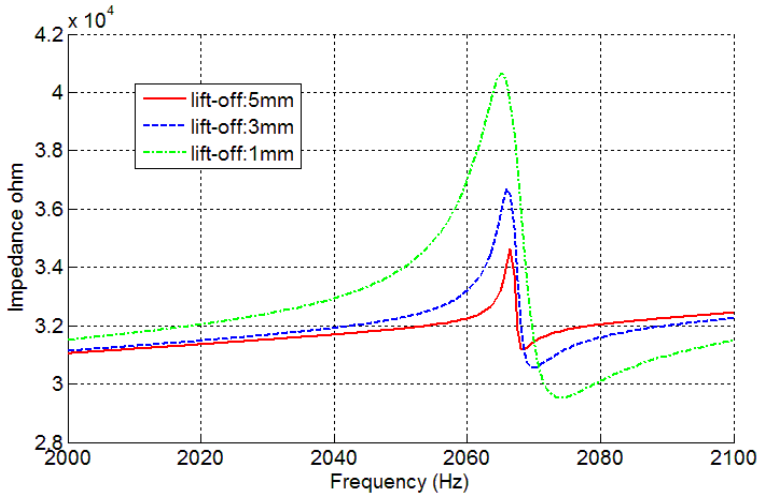

Figure 2-6. Numerical prediction of the impedance of the magnetic transducer using existing model (Wang and Tang, 2012): results around the first peak

The numerical results of the second peaks based on the eddy current modeling by Wang and Tang (2012) are shown in Figure 2-8. Similar to the preceding analysis, since the beam inductance is neglected in that model, the peak frequencies and the peak values around the transducer resonant frequency do not exhibit changes as the lift-off distance changes.

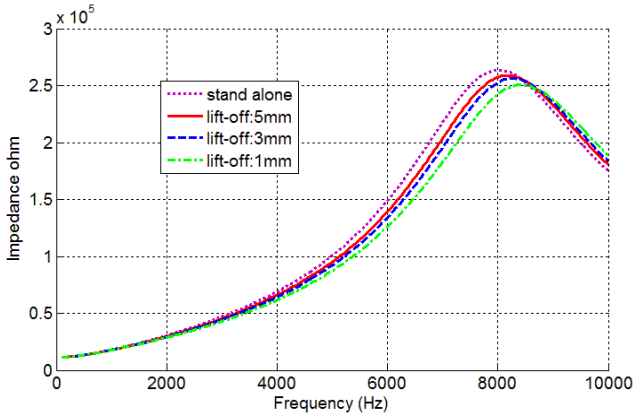

Figure 2-7. Experimental results of the impedance of the magnetic transducer

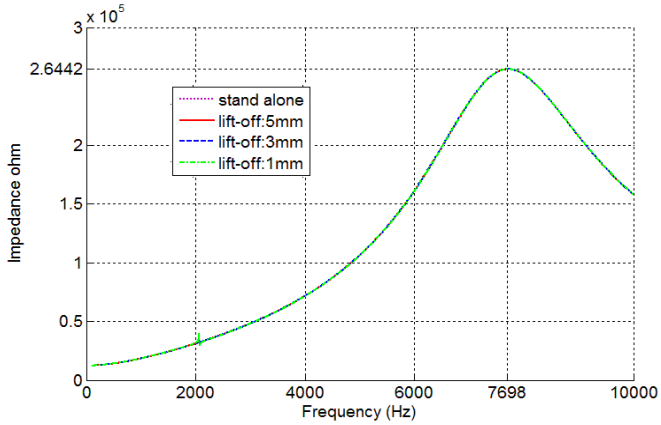

Figure 2-8. Numerical prediction of the impedance of the magnetic transducer using existing model (Wang and Tang, 2012)

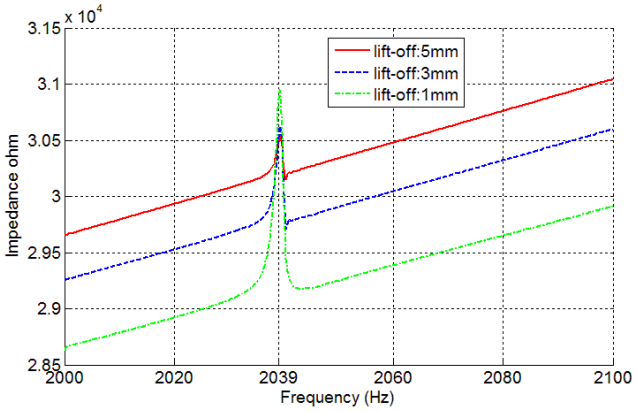

Figure 2-9. Experimental results of the impedance of the magnetic transducer around the first peak when fault is introduced

Finally, we examine the model prediction performance when structural fault is introduced. In experiment, a small added mass (1 gram) is attached onto the beam (130 mm from the left end of the beam) to emulate the fault effect. For the 9th beam natural frequency, this added mass causes the same frequency change as that due to a 0.5% modal stiffness loss. The experimental impedances around the 9th beam natural frequency when the fault is introduced are shown in Figure 2-9. Comparing with the healthy experimental results shown in Figure 2-5, we can observe that the peak frequency is reduced from 2046.5 Hz to 2039 Hz. Under different lift-off distances, the frequency shifts are almost the same. The fault scenario is then introduced to the numerical model, and the results of impedance prediction around the 9th beam frequency are shown in Figure 2-10. Comparing with the numerical results under healthy situation shown in Figure 2-4, we can observe that the peak frequency is reduced from 2066.4 Hz to 2059.5 Hz. The frequency reduction agrees very well with the experiment. Similar to experimental results, under different lift-off distances, the frequency shifts are almost the same. Meanwhile, comparing Figure 2-9 with Figure 2-10, we can see that the model prediction with fault occurrence has very good agreement with experiment in impedance magnitudes under all lift-off distances.

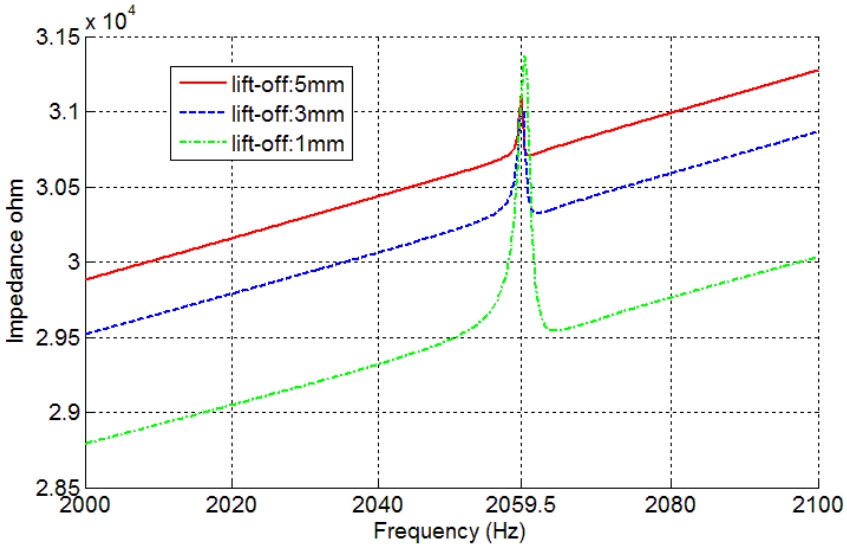

Figure 10. Numerical prediction of the impedance of the magnetic transducer around the first peak when fault is introduced

In summary, from the comparisons on both the peak frequencies and the peak values in impedance curves, we can find that the new model proposed in this research can directly describe the magneto-mechanical coupling under different lift-off distances, and accurately predict the impedance responses. Furthermore, the model prediction matches well with experiment when fault is introduced into the beam.

2.5 Concluding Remarks

In this research, we develop the mathematical model of a magnetic transducer used in impedance-based structural fault detection. The particular magnetic transducer consists of a coil inserted with a permanent magnetic known as an EMAT. As the magneto-mechanical coupling is lift-off distance-dependent, our focus is on the capability of directly predicting impedance response under given lift-off distance. A key hypothesis made is that the eddy current induced by the coil, that forms closed circular loops in the structure, will act as flowing in fictitious coils embedded in the structure with different radii. Building upon this hypothesis, a complete mathematical model describing the sensor-structure interaction is formulated which includes the mutual inductance prediction under given lift-off distance. The model predictions are then compared with experimental results and with simulations of an existing model. Our case analyses indicate that the new model developed can accurately predict the peak frequencies and peak values in impedance curves which are critical to fault detection practice.

Chapter 3 Direct Compensation of Lift-Off Oscillation Effect in Magnetic Impedance-Based Fault Detection

Owing to its magneto-mechanical coupling characteristics, a magnetic transducer such as the electro-magnetic acoustic transducer can excite a metallic structure by means of the Lorenz force, and its electrical impedance is actually directly related to the mechanical impedance of the structure. Therefore, the change of electrical impedance measured can be used as an indicator of fault occurrence. As such, this type of magnetic transducer can be used in impedance-based structural fault detection, which features a non-contact advantage. Nevertheless, one key issue is that the coupling between the magnetic transducer and the structure monitored is strongly influenced by the lift-off distance (i.e. the distance from the transducer to the structure) which oscillates as the structure is oftentimes subject to oscillation/movement due to environment disturbance. In this research, we propose a new data analysis approach of transformed impedance that is immune to the lift-off distance oscillation during measurements. This data analysis approach takes advantage of the lift-off distance information embedded in the impedance measurement, and is capable of removing the lift-off oscillation effect without explicitly measuring it. By doing so, the fault signature can be highlighted directly. Numerical simulations and experimental validations are carried out to demonstrate the effectiveness.

3.1 Introduction

Magnetic transducers have been applied in non-destructive evaluation (NDE), as they can facilitate for example eddy current testing (ECT) (Hashizume et al, 1992; Auld and Moulder, 1999; Javier et al, 2011). In this research we consider a type of magnetic transducer that is an electrical coil inserted with a permanent magnet. In literature it is commonly referred to as an electro-magnetic acoustic transducer (EMAT) typically employed as an actuator (Wilcox et al, 2005; Jian et al, 2006; Thomas et al, 2009). Owing to the two-way magneto-mechanical coupling between the transducer and metallic structures, an EMAT-type

magnetic transducer has recently been explored in the so-called impedance-based structural fault detection (Zagrai, 2009; Wang and Tang, 2012), in which it is employed as actuator (to excite the dynamic response in the structure monitored) and sensor (to sense the change of dynamic response) simultaneously. In this approach, the change of the transducer impedance, which is caused by the fault-induced change of the structural response, is employed as fault indicator. As the information carrier is the dynamic response excited, this approach has much broader detection range than traditional NDE methods and thus can be used for real-time fault detection. The coupling between the transducer and the structure monitored is based upon the interactive magnetic field between the magnetic transducer and the induced eddy current in the structure. In other words, there is no direct contact between the transducer and the structure. This non-contact feature can yield advantage in monitoring large-scale structures using only a small number of moveable sensor units. It also yields the possibility of monitoring moving/rotating parts of a structure using a sensory system fixed to the stationary base. One important issue, however, is that the coupling between the magnetic transducer and the structure is significantly influenced by the lift-off distance (i.e. the distance from the transducer to the structure monitored) which may be subject to oscillation induced by environmental disturbances.

In traditional ECT, the lift-off oscillations change the mutual-inductance between the magnetic transducer and the test sample, which may cause false alarms (Tian and Sophian, 2005). Some attempts have been made to compensate such oscillations. Lift-off point of intersection (LOI), which is the time at which different transient time responses of the magnetic transducer intersect when there are only lift-off distances changes, is one of the most used signal feature extraction method applied to reduce the unwanted lift-off oscillation influence (Mandache and Lefebvre, 2006). If the structure monitored has defect, the voltage amplitude at the lift-off point of intersection will vary from the value under the healthy condition. By using a calibration specimen, it is possible to generate a look-up table providing voltage amplitudes versus material loss (Giguere et al, 2001). However, the LOI relies heavily on the structure of the probe and the conductivity of the specimen (Shu et al, 2008). The LOI method also requires the direct

measurement of lift-off distance (Lefebvre and Mandache, 2006). Different probe designs are also studied. For example, an eddy current surface probe, in which the pick-up coil is perpendicular to the excitation coil, is proposed to cancel the lift-off noise (Hoshikawa and Koyama, 2001). This probe is suitable for eddy current testing at a very small lift-off distance. For another example, two-stage differential probes are also widely used in ECT, which generally consist of four pick up coils used to acquire two types of reference signals. These signals are then used in a two-stage subtraction and normalization process to compensate the lift-off effect. The two-stage differential probes are capable of self-calibration and only reflect the voltage changes caused by defect (Shu et al, 2008). There are however requirements to make all pick up coils same in the two-stage differential probe and to guarantee all the probes are parallel to the surface of the structure. Much less work has been done regarding lift-off oscillation in EMAT method. It has been noticed that in a pitch–catch type ultrasonic detection system with two EMATs, the apparent arrival times of the ultrasonic waves change with oscillation in lift-off distances. By investigating the impedance behavior of the inductive coil and establishing the received signal profile according to different lift-off distances, the arrival times of the dominant peaks of the Lamb wave observed can be treated as a predictable function of lift-off distance (Morrison et al, 2006). If the lift-off distance at the time of measurement is known, the observed response signal can be calibrated to the value expected at a standard lift-off.

In the magnetic impedance-based fault detection, the issue of lift-off distance oscillation during fault detection measurement is at least equally concerning, because in such application the same transducer performs the function of actuation and sensing simultaneously. The problem, furthermore, appears to be actually more challenging. Since structural dynamic response is excited and measured in this type of methods, inferring fault occurrence usually requires solving an inverse dynamic problem utilizing either model-based approach or data-oriented approach, both of which are subject to on-going research (Wang and Tang, 2009; Zagrai and Giurgiutiu, 2001; Rosado et al, 2013). In model-based approach, the lift-off distance is needed as input information for the model to compute or predict the transducer impedance. Thus

a high precision displacement sensor would be needed to accurately record the exact lift-off distance at every single frequency point during impedance measurements. In data-oriented approach, an extremely large database would be required in order to calibrate the impedance measured under different lift-off distances at each frequency point. This requires precisely measure and record the baseline impedance information in advance at all possible lift-off distances and also requires the accurate measurement of lift-off distance during fault detection.

3.2 Research Overview

It is worth noting that magnetic transducer can also be used as eddy current-based displacement sensor. In such an application, it measures the displacement by detecting variation in the transducer impedance which varies as a result of the change in distance between the magnetic transducer and the monitored structure (Wang and Feng, 2013). In other words, the lift-off distances information is implicitly embedded in the impedance measurement of the magnetic transducer. In a recent modeling effort of magnetic impedance sensor for fault detection, the relation between both the imaginary part and real part of transducer impedance and the lift-off distance is explicitly identified. These studies inspire the underlying idea of this research which is to explore the possibility of directly compensating the lift-off effect in impedance measurements by elucidating the intrinsic relation between the impedance and the lift-off distance. The rest of this paper is arranged as follows. In Section 3.3, a new lift-off effect compensation method based on data analysis is proposed. The new method uses a scale factor to transform the transducer impedance. A properly chosen scale factor can make the transformed impedance immune to the lift-off variation. Moreover, it is identified that a constant scale factor can be reached, which makes the compensation procedure simple and efficient. In Sections 3.4 and 3.5, numerical case studies and experimental validations are reported, respectively, to illustrate the proposed approach. Section 3.6 summarizes the research progress.

3.3 Approach Formulation

Here we consider the setup shown in Figure1. A magnetic transducer, which is an electrical coil inserted with a cylindrical permanent magnet (with length l_P and radius r_P), is placed above a cantilever beam made of aluminum (with length l_b, width w_b, and thickness t_b). The distance between the bottom surface of the coil and the top surface of the cantilever beam is the lift-off distance *h*. This EMAT-type magnetic transducer is employed as an actuator in the impedance-based fault detection, and therefore is subjected to harmonic voltage excitation. When the harmonic current I goes through the electrical coil, a harmonic magnetic field is generated. According to Faraday's law, eddy current $\mathbf{J}$ is induced into the beam underneath. The eddy current can generate a Lorentz force $\mathbf{F}_L$ under the static magnetic field of the permanent magnet. The harmonic Lorentz force excitation leads to the harmonic dynamic response of the beam structure governed by (Shuai and Tang, 2014),

$$m\ddot{q} + c\dot{q} + kq = f_L \tag{3-1}$$

where,

$$f_L = \int_0^{l_b} [\delta(x - x_0) \iiint (\mathbf{J} \times \mathbf{B}_P) dV] \phi(x) dx \tag{3-2}$$

m, c, and k are the equivalent mass, damping, and stiffness corresponding to the vibration mode of interest, respectively. A standard assumed mode approach is used in model discretization in which the beam response is expressed as $w(x,t) = \phi(x)q(t)$. $\phi(x)$ is the structural mode of interest and used in model discretization, and $q(t)$ is the corresponding generalized displacement. f_L is the generalized Lorentz force corresponding to the specific mode. For simple illustration, we only consider one mode in the analysis. Here the Lorentz force is treated as a point force acting at x_0 which is the location of the center of the eddy current loop, and δ is the Dirac delta function. $\mathbf{B}_P$ is the static magnetic flux density of the permanent magnet.

At the same time, this EMAT-type magnetic transducer is also used as a sensing element. It is assumed that the eddy currents run in a group of fictitious coils within the structure, which have continuously varying radius and each coil has one turn. The wires that form these fictitious coils have infinitesimally small cross section, and there is no mutual influence between these eddy current coils. Each fictitious eddy current coil has resistance R_{bi} and inductance L_{bi}. The mutual effect between the magnetic transducer and the eddy currents can be treated as a mutual inductance between the primary circuit and the secondary circuit in a voltage transformer. Due to the time-varying magnetic field of the primary circuit (the magnetic transducer), a voltage V_{Lbi} is induced in the secondary circuit (one fictitious eddy current coil). The structural vibration under the static magnetic field $\mathbf{B}_P$ induces another voltage V_{Pi}. We then have

$$V_{Lbi} = L_{Mi}\dot{I} - L_{bi}\dot{J}_i = V_{Pi} + R_{bi}J_i \tag{3-3}$$

$$V_{Pi} = \oint \phi(x) B_{Pr} dl \cdot \dot{q} \tag{3-4}$$

where L_{Mi} is the mutual inductance between the magnetic transducer and one fictitious eddy current coil. B_{Pr} is the component of the static magnetic flux density in the r direction. The eddy current J_i in turn generates a magnetic field that will affect the magnetic field inside the electrical coil and eventually affect the output voltage of the magnetic transducer. In the voltage transformer model, this process is characterized by the mutual inductance between the primary circuit and the secondary circuit. The output voltage V_L of the magnetic transducer is

$$V_L = L\dot{I} - \iint L_{Mi}\dot{J}_i dr dz \tag{3-5}$$

From Equation (3-1) to Equation (3-5), the impedance of the magnetic transducer can be derived as,

$$Z = \frac{Z_L k_c R_1}{k_c R_1 + Z_L k_c + j\omega Z_L R_1} + R_2 \tag{3-6}$$

where

$$Z_L = L\omega j + I_1 + I_2 j = (L\omega + I_2) j + I_1 \tag{3-7}$$

$$I_1 + I_2 j = P_1\omega^2 - P_2\omega j \frac{k_1\omega^2}{-m\omega^2 + j\omega c + k - j\omega k_2} \tag{3-8}$$

$$k_1 = \int_0^{l_b} \delta(x - x_0) \iiint (\frac{L_{Mi}}{L_b\omega j + R_b} B_{Pr}) dV\phi(x)dx \tag{3-9}$$

$$k_2 = \int_0^{l_b} \delta(x - x_0) \iiint (-\frac{\oint \phi(x) B_{Pr} dl}{L_b\omega j + R_b} B_{Pr}) dV\phi(x)dx \tag{3-10}$$

$$P_1 = \iint \frac{{L_{Mi}}^2}{L_{bi}\omega j + R_{bi}} drdz \tag{3-11}$$

$$P_2 = \iint L_{Mi} \frac{\oint \phi(x) B_{Pr} dl}{L_{bi}\omega j + R_{bi}} drdz \tag{3-12}$$

Here ω is the excitation frequency. L is the magnetic transducer's inherent inductance. k_c is the inverse of its parasitic capacitance in parallel with the coil inductance element. R_1 is its parasitic resistance that is in parallel with the coil as well. R_2 is the wire's resistance in series with the coil (Shuai and Tang, 2014). The absolute value, real part and imaginary part of the complex impedance of the magnetic transducer can be written as, respectively,

$$|Z|^2 = \frac{[k_c(R_1 + R_2)I_1 + k_c R_1 R_2 - (L\omega + I_2)\omega R_1 R_2]^2 + [k_c(R_1 + R_2)(L\omega + I_2) + \omega R_1 R_2 I_1]^2}{[k_c R_1 + I_1 k_c - (L\omega + I_2)R_1\omega]^2 + [k_c(L\omega + I_2) + I_1 R_1\omega]^2} \tag{3-13}$$

$$Z_{\text{real}} = \frac{k_c R_1 I_1[k_c R_1 + I_1 k_c - (L\omega + I_2)R_1\omega] + k_c R_1(L\omega + I_2)[k_c(L\omega + I_2) + I_1 R_1\omega]}{[k_c R_1 + I_1 k_c - (L\omega + I_2)R_1\omega]^2 + [k_c(L\omega + I_2) + I_1 R_1\omega]^2} + R_2 \tag{3-14}$$

$$Z_{\text{imag}} = \frac{{k_c}^2 {R_1}^2 (L\omega + I_2) - k_c {R_1}^2 \omega[(L\omega + I_2)^2 + {I_1}^2]}{[k_c R_1 + I_1 k_c - (L\omega + I_2)R_1\omega]^2 + [k_c(L\omega + I_2) + I_1 R_1\omega]^2} \tag{3-15}$$

It is worth emphasizing that P_1, P_2, k_1 and k_2 in Equation (3-8) are dependent on the lift-off distance. In other words, I_1 and I_2 will vary with the lift-off distance. We can observe that $|Z|^2$, Z_{real} and Z_{imag} are

all influenced by I_1 and I_2. This means the square of the absolute value, the real part and the imaginary part of the impedance of the magnetic transducer all contain the lift-off information. We now define a Transformed Impedance TI_2 as,

$$\mathrm{TI}_2 = |Z|^2 - \alpha Z_{\mathrm{imag}} = \frac{a_1(L\omega + I_2)^2 + a_2(L\omega + I_2) + a_1 I_1^{\,2} + a_3 I_1 + a_4}{[k_c R_1 + I_1 k_c - (L\omega + I_2)R_1\omega]^2 + [k_c(L\omega + I_2) + I_1 R_1 \omega]^2} \tag{3-16}$$

where

$$a_1 = k_c^{\,2}(R_1 + R_2)^2 + R_1^{\,2}R_2^{\,2}\omega^2 + \alpha k_c R_1^{\,2}\omega, \quad a_2 = -2kcR_1^{\,2}R_2^{\,2}\omega - \alpha k_c^{\,2}R_1^{\,2}$$

$$a_3 = 2k_c^{\,2}R_1R_2(R_1 + R_2), \quad a_4 = k_c^{\,2}R_1^{\,2}R_2^{\,2}$$

α is a scale factor to be determined. Here the subscript 2 simply indicates that the Transformed Impedance defined has actually the dimension of the square of usual impedance. Apparently, the Transformed Impedance is coupled with the mechanical impedance of the monitored structure, since I_1 and I_2 contain the mechanical impedance information (Equation (3-8)). In the discussion provided in Section 3.4, it will be further illustrated that the Transformed Impedance has the same peak frequencies as those in the original magnetic impedance curve, and these peak frequencies coincide with the structural resonant frequencies. Therefore, the changes of the Transformed Impedance caused by fault can be employed as fault indicator, in basically the same way as the changes of the original magnetic impedance. Our goal is to find a proper α such that TI_2 can be immune to the change of the lift-off distance.

When the lift-off distance has variation Δh, we can write I_1 and I_2 as,

$$I_1 = I_{1s} + \Delta I_1 \tag{3-17}$$

$$I_2 = I_{2s} + \Delta I_2 \tag{3-18}$$

where I_{1s} and I_{2s} represent the un-perturbed, nominal values at a given lift-off distance *h*. ΔI_1 and ΔI_2 are their variation quantities corresponding to the lift-off variation Δh. Substitute Equations (3-17) and (3-18) back to Equation (3-16), we have

$$\mathrm{TI}_2 = \frac{f + \Delta f}{g + \Delta g} \tag{3-19}$$

where

$$f = a_1(L\omega + I_{2s})^2 + a_2(L\omega + I_{2s}) + a_1 {I_{1s}}^2 + a_3 I_{1s} + a_4 \tag{3-20}$$

$$\Delta f = a_1 {\Delta I_2}^2 + [2a_1(L\omega + I_{2s}) + a_2]\Delta I_2 + a_1 {\Delta I_1}^2 + (2a_1 I_{1s} + a_3)\Delta I_1 \tag{3-21}$$

$$g = b_1(L\omega + I_{2s})^2 + b_2(L\omega + I_{2s}) + b_1 {I_{1s}}^2 + b_3 I_{1s} + b_4 \tag{3-22}$$

$$\Delta g = b_1 {\Delta I_2}^2 + [2b_1(L\omega + I_{2s}) + b_2]\Delta I_2 + b_1 {\Delta I_1}^2 + (2b_1 I_{1s} + b_3)\Delta I_1 \tag{3-23}$$

$$b_1 = {k_c}^2 + {R_1}^2\omega^2, \quad b_2 = -2{k_c}{R_1}^2\omega, \quad b_3 = 2{k_c}^2 R_1, \quad b_4 = {k_c}^2 {R_1}^2 \tag{3-24}$$

f is the un-perturbed part of the numerator of TI_2, and g is the un-perturbed part of the denominator. f / g represents the un-perturbed Transformed Impedance when there is no lift-off oscillation. Δf and Δg represent the changing part of the numerator and the denominator that are caused by the lift-off distance variation Δh. We intend to cancel the effects of Δf and Δg in the Transformed Impedance.

The fundamental idea of our approach then becomes: if we can find a proper scale factor α that can make $f / g = \Delta f / \Delta g$, then the Transformed Impedance TI_2 will always be equal to the un-perturbed Transformed Impedance f / g no matter how the lift-off distance varies, i.e.,

$$\frac{f}{g} = \frac{\Delta f}{\Delta g} \tag{3-25}$$

Solving Equation (25), we can obtain α as

$$\alpha = \frac{\beta_1 + \Delta g \beta_2}{\beta_3 + \Delta g \beta_4} \tag{3-26}$$

where

$$\begin{aligned}\beta_1 = &-2k_c{}^2 R_1 R_2 (R_1 + R_2)\Delta I_1 - [\Delta I_2{}^2 + 2L\omega\Delta I_2 + 2I_{2s}\Delta I_2 + 2I_{1s}\Delta I_1 + \Delta I_1{}^2] \\ &\times [k_c{}^2 (R_1 + R_2)^2 + R_1{}^2 R_2{}^2 \omega^2] + 2k_c R_1{}^2 R_2{}^2 \omega \Delta I_2\end{aligned} \tag{3-27}$$

$$\begin{aligned}\beta_2 = &\{2k_c{}^2 R_1 R_2 (R_1 + R_2) I_{1s} + k_c{}^2 R_1{}^2 R_2{}^2 + [(L\omega + I_{2s})^2 + I_{1s}{}^2][k_c{}^2 (R_1 + R_2)^2 + R_1{}^2 R_2{}^2 \omega^2] \\ &-2k_c R_1{}^2 R_2{}^2 \omega (L\omega + I_{1s})\} / \{(k_c{}^2 + R_1{}^2 \omega^2)(L\omega + I_{2s})^2 - 2k_c R_1{}^2 \omega (L\omega + I_{2s}) \\ &+(k_c{}^2 + R_1{}^2 \omega^2) I_{1s}{}^2 + 2k_c{}^2 R_1 I_{1s} + k_c{}^2 R_1{}^2\}\end{aligned} \tag{3-28}$$

$$\beta_3 = (\Delta I_2{}^2 + 2L\omega\Delta I_2 + 2I_{2s}\Delta I_2 + 2I_{1s}\Delta I_1 + \Delta I_1{}^2) k_c R_1{}^2 \omega - \Delta I_2 k_c{}^2 R_1{}^2 \tag{3-29}$$

$$\begin{aligned}\beta_4 = &\{(L\omega + I_{2s}) k_c{}^2 R_1{}^2 - [(L\omega + I_{2s})^2 + I_{1s}{}^2] k_c R_1{}^2 \omega\} / \{(k_c{}^2 + R_1{}^2 \omega^2)(L\omega + I_{2s})^2 \\ &-2k_c R_1{}^2 \omega (L\omega + I_{2s}) + (k_c{}^2 + R_1{}^2 \omega^2) I_{1s}{}^2 + 2k_c{}^2 R_1 I_{1s} + k_c{}^2 R_1{}^2\}\end{aligned} \tag{3-30}$$

From Equations (3-26) to (3-30), we can observe that the scale factor α is related to the lift-off variation Δh and the excitation frequency ω. If we can accurately measure the lift-off distance at each frequency point during the impedance measurement procedure, we can possibly obtain a series of scale factor α based on Equation (3-26) and then obtain the Transformed Impedance from Equation (3-16). However, our hope here is to find a scale factor α that itself is independent of the changes of lift-off distance and frequency in certain range, so that we can use a constant scale factor in the analysis. In Equation (3-26), β_1, β_3 and Δg are related to the lift-off variation, since ΔI_1 and ΔI_2 are the corresponding impedance variations caused by the lift-off variations Δh. From Equation (3-7), we can see that $I_1 + I_2 j$ is the impedance term due to the magnetic coupling between the magnetic transducer and the structure. Compared with the impedance of the coil inductor, I_{1s} and I_{2s} are small in general especially at frequencies away from the structural resonance. Their variations ΔI_1 and ΔI_2 are thus much smaller than $L\omega$, so ΔI_1 and ΔI_2 can be treated as small quantities. Recall Equations (3-8) to (3-12). The mechanical impedance of the structure

($-m\omega^2 + j\omega c + k$) is generally large at frequencies away from the resonance. We can then rewrite Equation (3-8) as,

$$I_1 + I_2 j = P_1\omega^2 - P_2\omega j \frac{k_1\omega^2}{-m\omega^2 + j\omega c + k - j\omega k_2} \approx P_1\omega^2 \tag{3-31}$$

Substituting Equation (3-11) into Equation (3-31) and separating the real and imaginary parts, we can obtain,

$$I_1 = \omega^2 \int_0^{w_b/2} (\int_h^{h+t_b} {L_{Mi}}^2 dz) \frac{R_{bi}}{(L_{bi}\omega)^2 + {R_{bi}}^2} dr \tag{3-32}$$

$$I_2 = -\omega^2 \int_0^{w_b/2} (\int_h^{h+t_b} {L_{Mi}}^2 dz) \frac{L_{bi}\omega}{(L_{bi}\omega)^2 + {R_{bi}}^2} dr \tag{3-33}$$

The eddy currents are continuously distributed in the structure, and in our case cover a cylindrical volume with radius $w_b/2$ and height t_b, where w_b and t_b are the width and thickness of the beam respectively. When there is lift-off variation Δh, I_1 can be rewritten as,

$$\begin{aligned} I_1 &= \omega^2 \int_0^{w_b/2} (\int_{h+\Delta h}^{h+t_b+\Delta h} {L_{Mi}}^2 dz) \frac{R_{bi}}{(L_{bi}\omega)^2 + {R_{bi}}^2} dr \\ &= \omega^2 \int_0^{w_b/2} (\int_{h+\Delta h}^{h} {L_{Mi}}^2 dz + \int_h^{h+t_b} {L_{Mi}}^2 dz + \int_{h+t_b}^{h+t_b+\Delta h} {L_{Mi}}^2 dz) \frac{R_{bi}}{(L_{bi}\omega)^2 + {R_{bi}}^2} dr \\ &= \omega^2 \int_0^{w_b/2} (\int_h^{h+t_b} {L_{Mi}}^2 dz) \frac{R_{bi}}{(L_{bi}\omega)^2 + {R_{bi}}^2} dr + \omega^2 \int_0^{w_b/2} (\int_{h+\Delta h}^{h} {L_{Mi}}^2 dz + \int_{h+t_b}^{h+t_b+\Delta h} {L_{Mi}}^2 dz) \frac{R_{bi}}{(L_{bi}\omega)^2 + {R_{bi}}^2} dr \end{aligned} \tag{3-34}$$

We can observe that the first term in the above expression is not affected by the lift-off variation, which is then denoted as I_{1s}, while the second term quantifies the influence due to the lift-off variation and is denoted as ΔI_1,

$$I_{1s} = \omega^2 \int_0^{w_b/2} (\int_h^{h+t_b} {L_{Mi}}^2 dz) \frac{R_{bi}}{(L_{bi}\omega)^2 + {R_{bi}}^2} dr \tag{3-35}$$

$$\Delta I_1 = \omega^2 \int_0^{w_b/2} (\int_{h+\Delta h}^{h} {L_{Mi}}^2 dz + \int_{h+t_b}^{h+t_b+\Delta h} {L_{Mi}}^2 dz) \frac{R_{bi}}{(L_{bi}\omega)^2 + {R_{bi}}^2} dr \tag{3-36}$$

Similarly, we can obtain the expressions of I_{2s} and ΔI_2 as

$$I_{2s} = -\omega^2 \int_0^{w_b/2} (\int_{h}^{h+t_b} {L_{Mi}}^2 dz) \frac{L_{bi}\omega}{(L_{bi}\omega)^2 + {R_{bi}}^2} dr \tag{3-37}$$

$$\Delta I_2 = -\omega^2 \int_0^{w_b/2} (\int_{h+\Delta h}^{h} {L_{Mi}}^2 dz + \int_{h+t_b}^{h+t_b+\Delta h} {L_{Mi}}^2 dz) \frac{L_{bi}\omega}{(L_{bi}\omega)^2 + {R_{bi}}^2} dr \tag{3-38}$$

Here L_{Mi} is the mutual inductance between the magnetic transducer and a single fictitious coil in the structure. When the integral interval which is the penetration depth in our case is small, we can assume that ${L_{Mi}}^2$ is a linear function of the *z* coordinate mathematically, and therefore ΔI_1 and ΔI_2 can be expressed as

$$\Delta I_1 = \omega^2 \int_0^{w_b/2} \Delta h \Delta({L_{Mi}}^2) \frac{R_{bi}}{(L_{bi}\omega)^2 + {R_{bi}}^2} dr = \omega^2 \Delta h^2 t_b \int_0^{w_b/2} \Upsilon \frac{R_{bi}}{(L_{bi}\omega)^2 + {R_{bi}}^2} dr \tag{3-39}$$

$$\Delta I_2 = -\omega^2 \int_0^{w_b/2} \Delta h \Delta({L_{Mi}}^2) \frac{L_{bi}\omega}{(L_{bi}\omega)^2 + {R_{bi}}^2} dr = -\omega^2 \Delta h^2 t_b \int_0^{w_b/2} \Upsilon \frac{L_{bi}\omega}{(L_{bi}\omega)^2 + {R_{bi}}^2} dr \tag{3-40}$$

where Υ is the slope of ${L_{Mi}}^2$. Combining Equations (3-39) and (3-40), we can derive that $\Delta I_1 / \Delta I_2$ is independent of the lift-off variation Δh. Let both the numerator and the denominator in Equation (3-26) be divided by ΔI_2, and neglect the small quantities ΔI_2 and ${\Delta I_1}^2 / \Delta I_2$. We can obtain

$$\frac{\beta_1}{\Delta I_2} = -2{k_c}^2 R_1 R_2 (R_1 + R_2) \frac{\Delta I_1}{\Delta I_2} - [2L\omega + 2I_{2s} + 2I_{1s} \frac{\Delta I_1}{\Delta I_2}][{k_c}^2 (R_1 + R_2)^2 + {R_1}^2 {R_2}^2 \omega^2] \\ +2k_c {R_1}^2 {R_2}^2 \omega \tag{3-41}$$

$$\frac{\beta_3}{\Delta I_2} = (2L\omega + 2I_{2s} + 2I_{1s} \frac{\Delta I_1}{\Delta I_2}) k_c {R_1}^2 \omega - {k_c}^2 {R_1}^2 \tag{3-42}$$

$$\frac{\Delta g}{\Delta I_2} = b_1 (2L\omega + 2I_{2s} + 2I_{1s} \frac{\Delta I_1}{\Delta I_2}) + b_2 + b_3 \frac{\Delta I_1}{\Delta I_2} \tag{3-43}$$

We can see that all those terms in Equation (3-26) that are related to the lift-off variation have been canceled. Finally, we can conclude that the scale factor α selected is indeed independent of the lift-off variation Δh. Since the scale factor α can be considered as lift-off variation independent, there is no need to measure and record the lift-off distances during impedance measurements. Furthermore, throughout the above derivation of the scale factor α, the information of the mechanical properties of the structure is not involved. In other words, this scale factor α is determined by the electrical properties of the magnetic transducer and the structure, the nominal lift-off distance, and the frequency range of interest. As no assumption of lift-off variation is made, this scale factor is applicable to random variation of lift-off distance.

3.4 Numerical Analysis

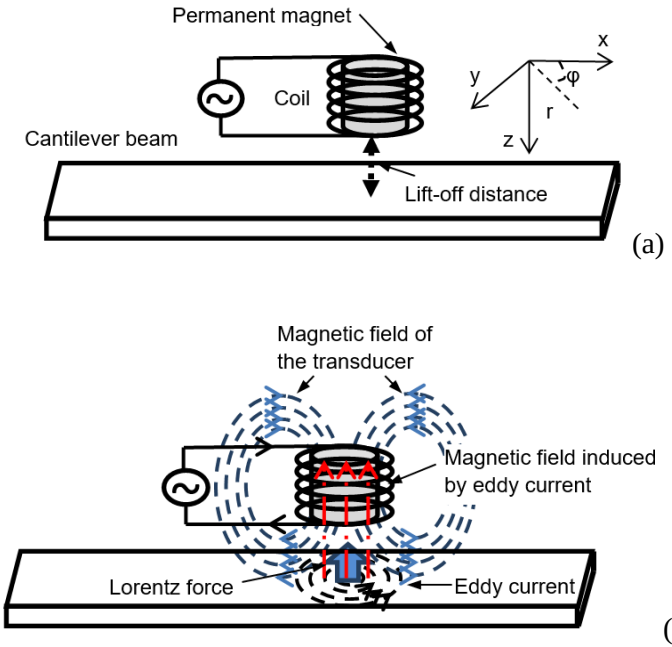

Figure 3-1. Magnetic impedance sensing illustration: (a) system configuration; (b) electro-magnetic interaction effects.

In this section we illustrate the proposed data analysis approach through numerical studies. The setup of the system is shown in Figure 3-1. A coil is placed above a cantilever beam (length 508 mm, width 25.4 mm, thickness 3.25 mm) made of aluminum (Al-2024, mass density 2780 Kg/m^3, Young's modulus 73

Gpa , conductivity 37.8 MS/m , permeability 1.256×10^{-6} H/m). The wire is winded in 384 layers along the axial direction of the coil with 26 turns in each layer. It has an average radius11.4 mm, and the diameter of the copper wire is 0.04 mm. A cylindrical permanent magnet (length 25 mm, radius 9.5 mm) is inserted in the center of the coil, which has axial magnetization 6.13×10^{5} A/m .

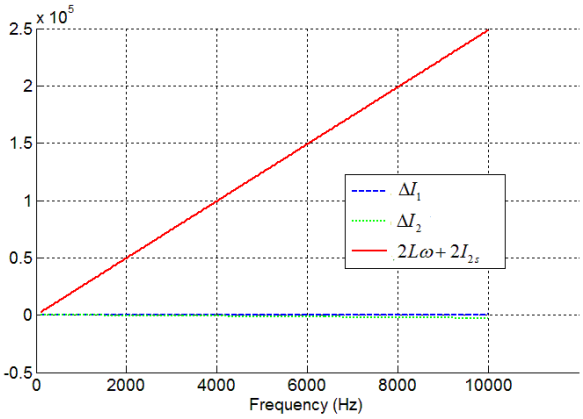

Figure 3-2. Comparison of the scales of ΔI_1 , ΔI_2 and $2L\omega + 2I_{2s}$.

In structural fault detection using impedance measurement, the change of impedance due to fault occurrence is most observable around the resonant peaks, e.g., shift of peak frequency and/or change of peak magnitude due to fault occurrence. Therefore, for illustration, we compute the scale factor α around the 9th resonant frequency of the beam which is 2046 Hz. The center of the transducer is located at 285 mm to the fixed end of the cantilever beam. The initial lift-off distance *h* is 10 mm, which is measured from the bottom surface of the coil to the top surface of the cantilever beam. The lift-off variation in this case illustration is a sinusoidal oscillation with 1.5 Hz frequency. In order to illustrate that the scale factor α is independent of the lift-off variation Δh , the results are obtained when the magnitude of the lift-off variation is set to different values, from 1 mm to 5 mm. Figure 3-2 shows that when the lift-off oscillation magnitude is 5 mm, ΔI_1 and ΔI_2 are very small compared to $2L\omega + 2I_{2s}$. It is worth pointing out that in this specific setup a 5 mm lift-off variation is quite large, as the initial lift-off distance is 10 mm. Therefore, this confirms our assumption that ΔI_1 and ΔI_2 are small quantities and can be neglected in Equation (3-26). Figure 3-3

shows that $\Delta I_1 / \Delta I_2$ remains almost constant as the lift-off variation magnitude changes from 1mm to 5mm. This shows that $\Delta I_1 / \Delta I_2$ can be treated as a constant when one computes the scale factor α. Figure 3-4 plots the derived scale factor α under different lift-off variations. We can observe that the scale factor α remains constant under different lift-off variation Δh.

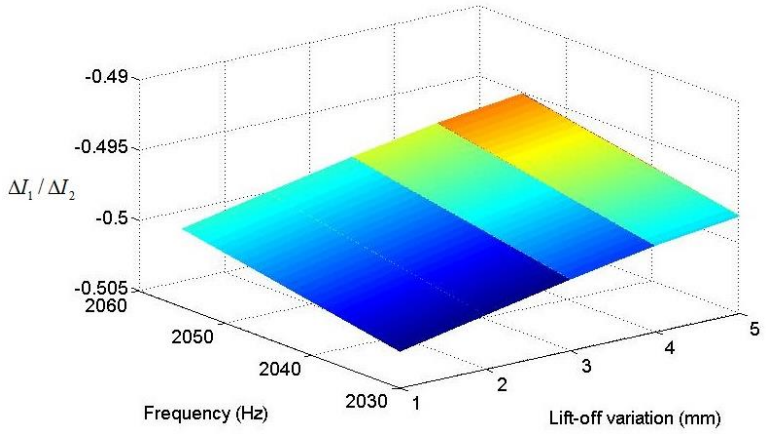

Figure 3-3. Relation of $\Delta I_1 / \Delta I_2$ with respect to excitation frequency and lift-off variation magnitude.

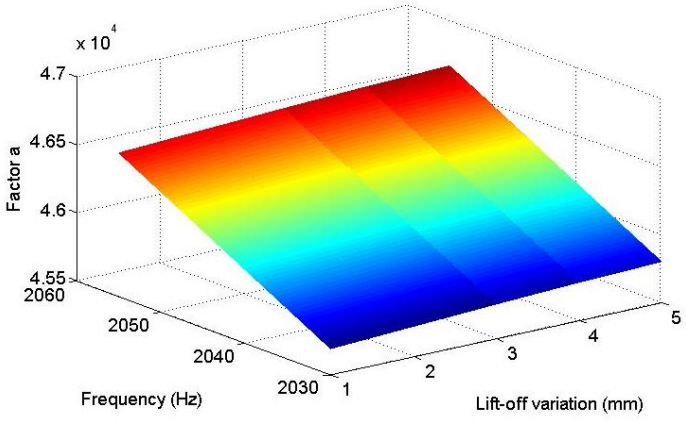

Figure 3-4. Relation of the scale factor with respect to excitation frequency and lift-off variation magnitude.

As fault detection is usually carried out by frequency-sweeping around resonances, the frequency ranges of interest are generally small, i.e., at the vicinity of resonant frequencies. From Figure 3-4, we can observe that the changes of factor α is small, from 4.55×10^4 to 4.65×10^4, when the swept frequency

range is around the 9th beam frequency, from 2030 Hz to 2055 Hz. Indeed, as will be shown later in Figure 3-6, when the scale factor is set as 4.58×10^4 or 4.66×10^4, the noise cancellation performances of the Transformed Impedance are similar. This indicates that the scale factor α can also be regarded as frequency independent at the vicinity of each resonant frequency.

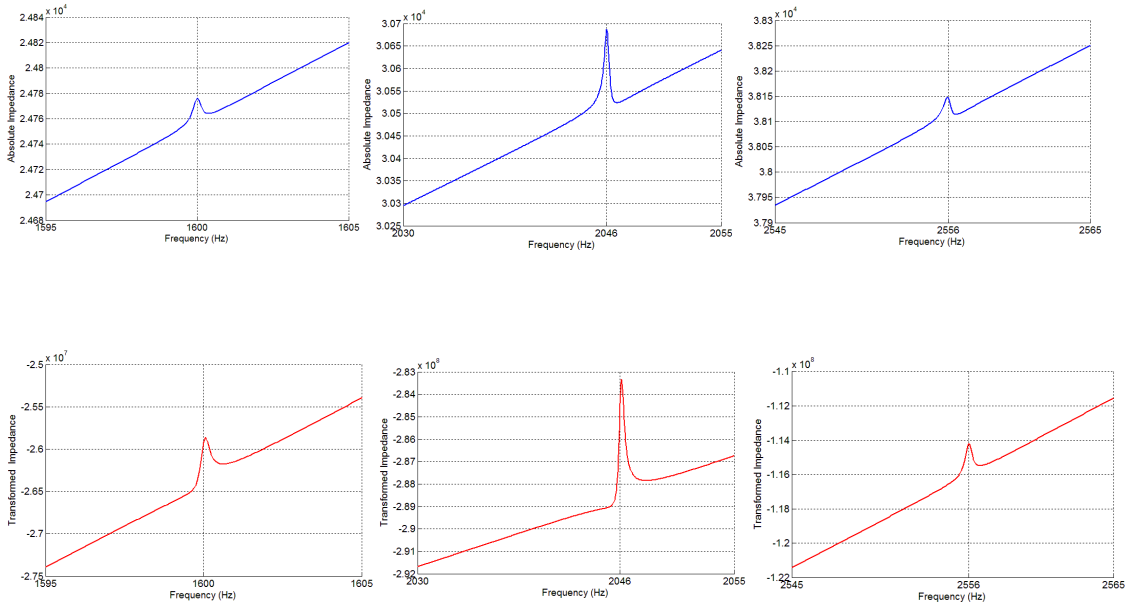

Figure 3-5. Comparison of magnetic impedance and Transform Impedance results (a) Absolute value of magnetic impedance (unit: ohm) around beam's 8th, 9th, and 10th resonant frequencies; (b) Transformed Impedance (unit: ohm^2) curves around beam's 8th, 9th, and 10th resonant frequencies.

For the 8th, 9th and 10th resonant frequencies, the scale factors are computed as 3.12×10^5, 4.61×10^5, and 6.09×10^4, respectively. The corresponding Transformed Impedance curves are shown in Figure 3-5. Comparing them with the original impedance curves, we can find that they have the same peak frequencies which coincide with the resonant frequencies, respectively, 1600 Hz, 2046 Hz, and 2556 Hz. This illustrates that Transformed Impedance is related to the structural mechanical impedance in a way that's very similar to the original magnetic impedance.

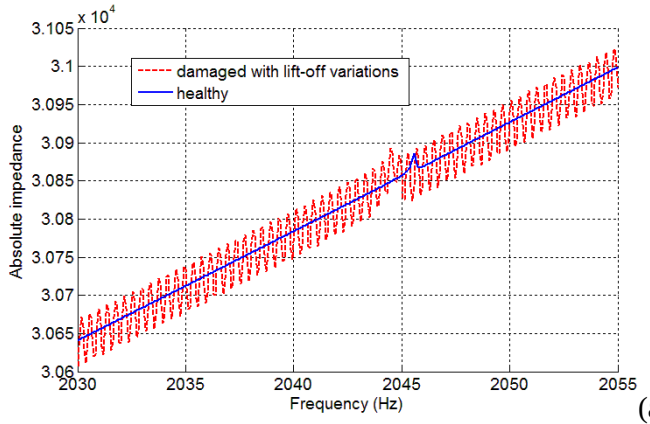

(a)

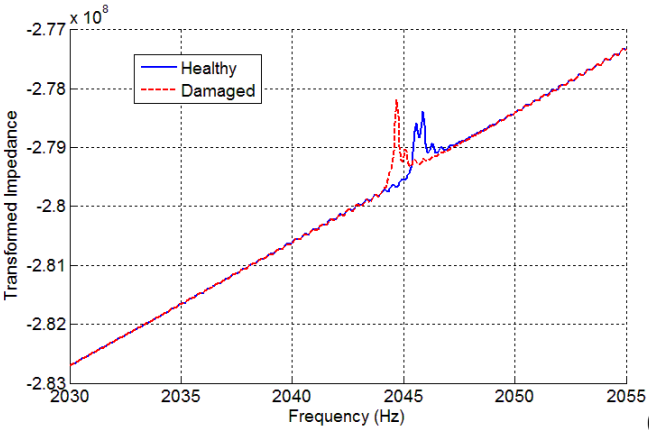

(b)

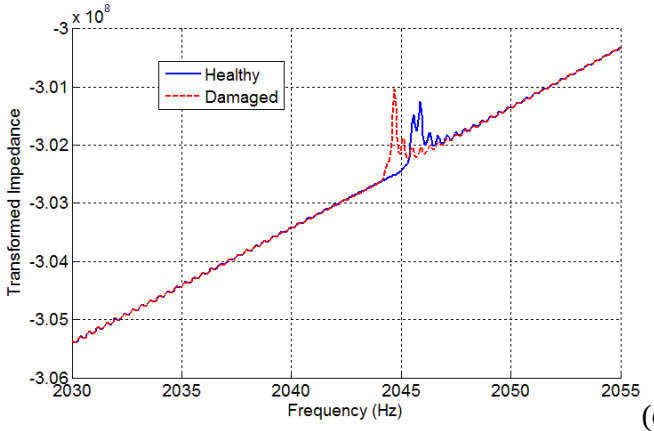

(c)

Figure 3-6. Comparison of magnetic impedance and Transform Impedance results: (a) absolute value of magnetic impedance (unit: ohm); (b) Transformed Impedance (unit: ohm^2) with scale factor 4.58×10^4;(c) Transformed Impedance (unit: ohm^2) with scale factor 4.66×10^4.

Figure 3-6 illustrates a simulated scenario of fault detection. A structural fault is introduced to the system, where the fault is quantified as causing a 0.1% change of the 9th structural resonant frequency. The

healthy impedance curve is shown in Figure 3-6(a). As the lift-off distance is subject to a sinusoidal oscillation with magnitude 1 mm, the impedance curve with fault exhibits significant noise, also plotted in Figure 3-6(a). Two slightly different scale factors are then used, 4.58×10^4, and 4.66×10^4, respectively, and the corresponding Transformed Impedances are plotted in Figure 3-6(b) and 3-6(c). We can clearly observe that the noise effects due to the lift-off oscillation are removed, and the Transformed Impedance exhibits changes in resonances, indicating fault occurrence.

3.5 Experimental Validation

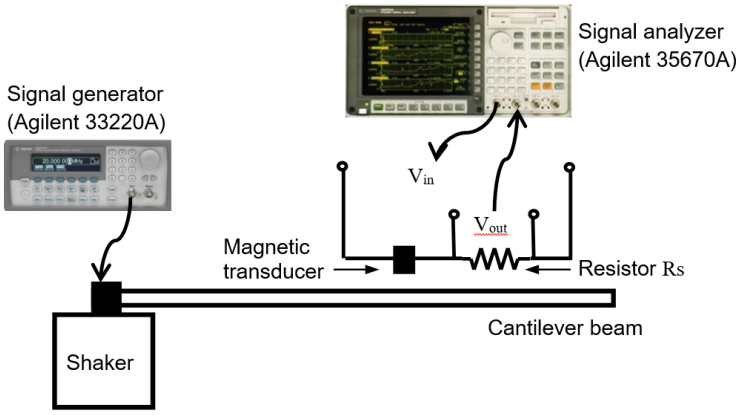

Figure 3-7. Experimental setup

The setup of the experiment is consistent with that employed in the numerical simulation. All related parameters are the same. The cantilever beam is mounted on a shaker that is commanded by a signal generator to emulate different lift-off oscillation scenarios (Figure 3-7). To extract experimentally the impedance of the magnetic transducer, a small resistor R_s (100 Ω) is used to measure the voltage drop across it, and thus the electrical current in the circuit can be obtained which then yields the impedance information. A signal analyzer (Agilent 35670A) is used in the experiment. The source channel generates the sinusoidal voltage V_{in} sent to the magnetic transducer, and the output voltage across the resistor V_{out} is recorded. Therefore, the experimentally extracted impedance is given as

$$Z_{\exp} = \frac{V_{\text{in}}}{I} = \frac{V_{\text{in}}}{V_{\text{out}}} R_s \tag{3-44}$$

In order to demonstrate the proposed Transformed Impedance method, we study a series of cases. The first case is around the 9th resonant frequency of the beam (2043 Hz). The measured resonant frequency is slightly lower than the numerical result, most likely due to the imperfect boundary conditions in the experiment. The initial lift-off distance *h* is 10 mm. The swept frequency range is from 2030 Hz to 2055 Hz. The computed scale factor at the resonant frequency in this case is 4.61×10^4. A small mass is attached onto the beam to simulate the fault effect, which causes the same resonant frequency change as that due to a 0.15% beam modal stiffness loss. Two types of signal are generated to excite two different lift-off oscillations. One signal is sinusoidal wave and the other signal is square wave. Their frequencies are both set as 1.5 Hz, and their magnitudes are 1 mm. Figure 3-8 shows the absolute, real and imaginary impedance curves under lift-off oscillations. We can find that it is hard to directly figure out the impedance changes induced by fault in these three impedance curve. However, in the Transformed Impedance curves plotted in Figures 3-9 and 3-10, the results are much smoother and most of the noise is cancelled. The important fault indicator, resonant frequency shift (from 2043.3 Hz to 2041.9 Hz), can be clearly observed.

In the second case, we examine the measurements around the 10th resonant frequency of the beam (2551 Hz). The initial lift-off distance *h* is changed to 5 mm. The center of the transducer is located at 360 mm to the fixed end of the cantilever beam. The swept frequency range is from 2535 Hz to 2565 Hz. The scale factor computed in this case is about 6.09×10^4. The same mass is attached to simulate fault case, which causes the 10th resonant frequency change as that due to 0.25% beam modal stiffness loss. The two different lift-off oscillations used in the first case are again employed here. From Figures 3-11 and 3-12, we can find that with this different initial lift-off distance and under a different resonant frequency (and hence a different scale factor), the noise effect in the original magnetic impedance measurements can be successfully removed in the Transformed Impedance curves. Indeed, the Transformed Impedance clearly indicates the resonant frequency shift (from 2549 Hz to 2545.8 Hz) and highlights the fault occurrence.

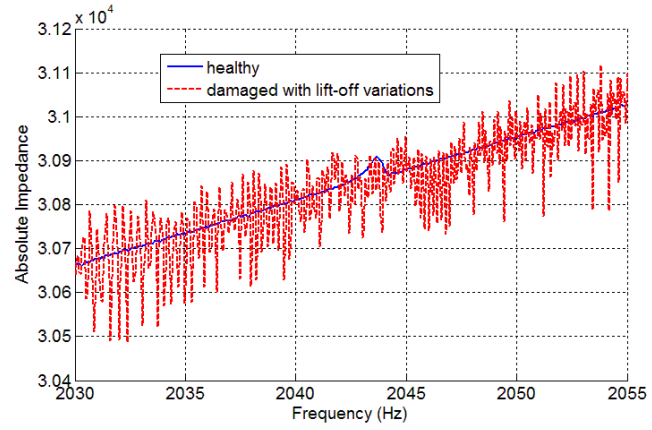

(a)

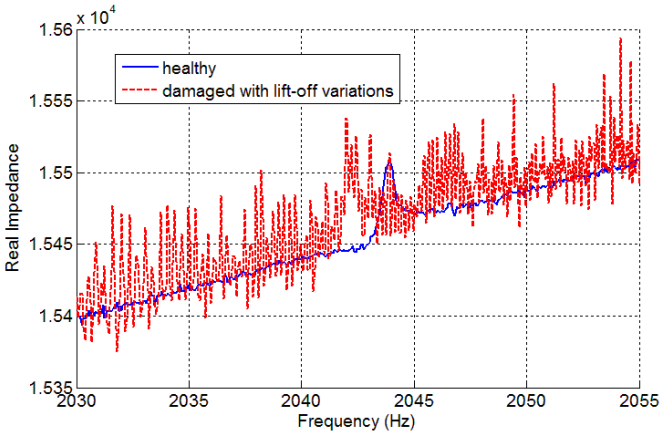

(b)

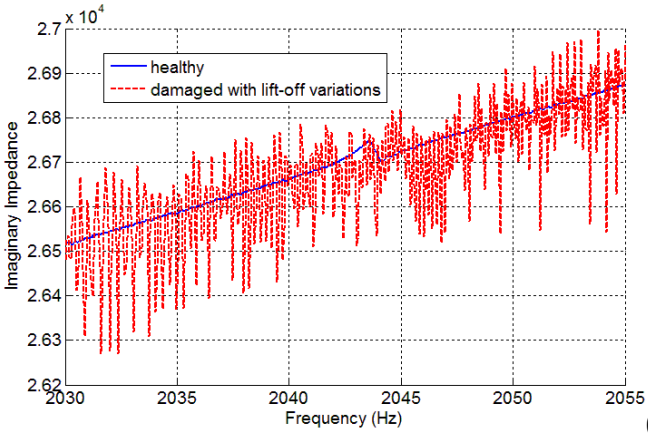

(c)

Figure 3-8. Experimentally measured magnetic impedances (unit: ohm) of healthy and faultd structure: (a) absolute value; (b) real part; (c) imaginary part.

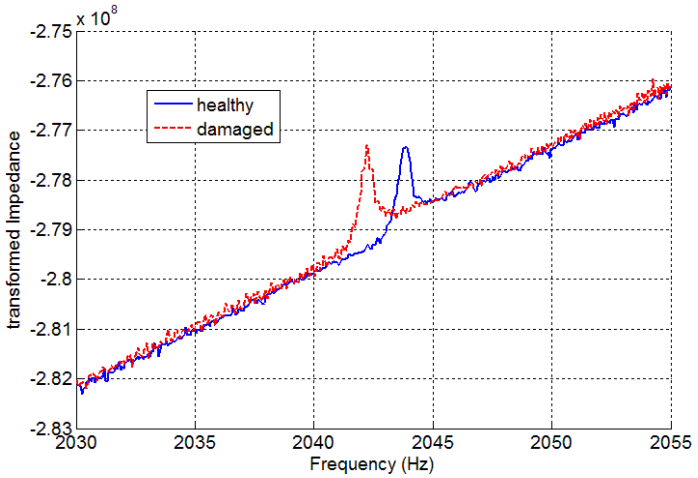

Figure 3-9. Transformed Impedance (unit; ohm^2) results when lift-off oscillation is a sinusoidal wave. Initial lift-off is 10 mm.

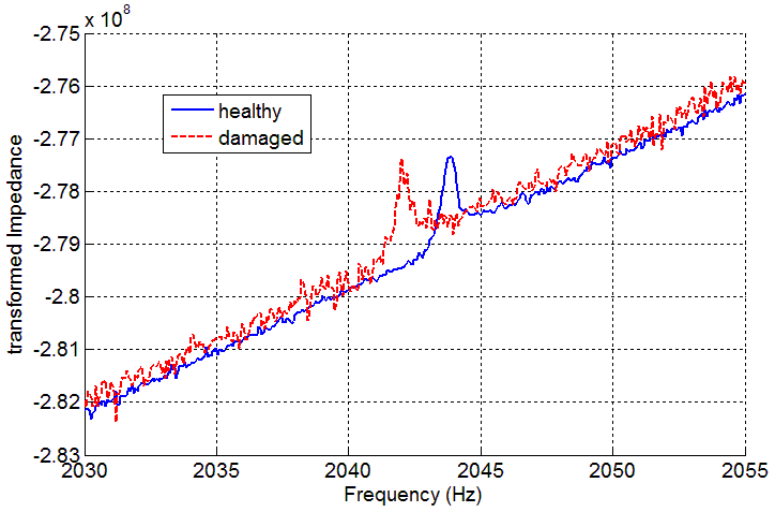

Figure 3-10. Transformed Impedance (unit: ohm^2) results when lift-off oscillation is a square wave. Initial lift-off is 10 mm.

In the third case, we examine the effectiveness of the proposed data analysis when the frequency and magnitude of the lift-off oscillations are not constant during one single measurement. The setup used in the first case is employed here. The initial lift-off distance *h* is 10 mm. The center of the transducer is

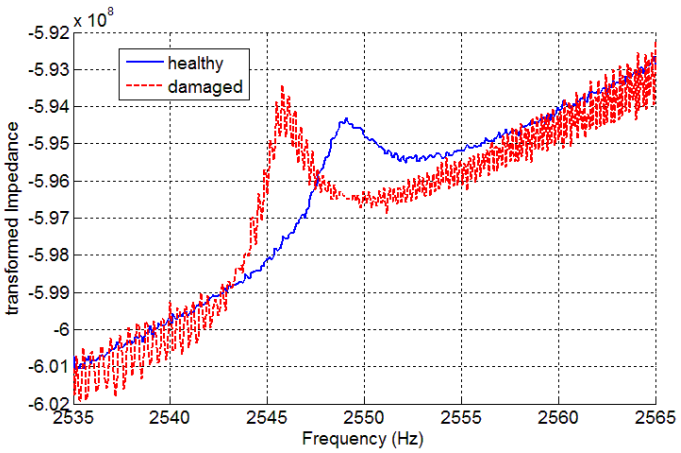

Figure 3-11. Transformed Impedance (unit: ohm^2) results when lift-off oscillation is a sinusoidal wave. Initial lift-off is 5 mm.

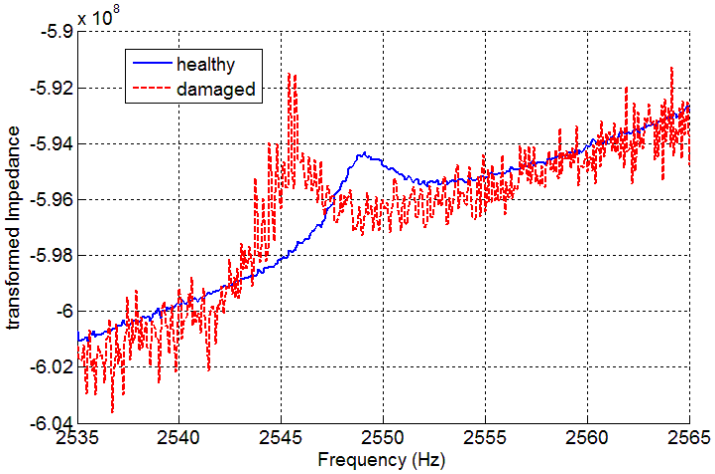

Figure 3-12. Transformed Impedance (unit: ohm^2) results when lift-off oscillation is a square wave. Initial lift-off is 5 mm.

located at 285 mm to the fixed end of the cantilever beam. The swept frequency range is from 2030 Hz to 2055 Hz. As mentioned, the scale factor computed is 4.61×10^4. The sine function is used to excite the lift-off oscillation. At first, the magnitude of the lift-off oscillation is kept as 1 mm, and its frequency is changed from 1.5 Hz to 11 Hz. From Figure 3-13, we can observe that while the frequencies of lift-off

oscillation are different, similar results of Transformed Impedances are obtained by using the same scale factor. Next, the frequency of the lift-off oscillation is kept as 1.5 Hz, and its magnitude is changed from 1 mm to 2 mm. From Figure 3-14, we can find that again the results of the Transformed Impedances are very similar, both achieving good performance of noise cancellation.

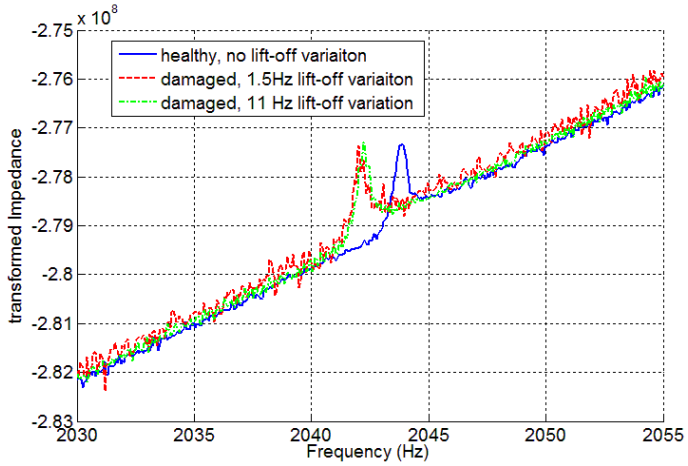

Figure 3-13. Transformed Impedance (unit: ohm^2) results under different lift-off oscillation frequencies using the same scale factor.

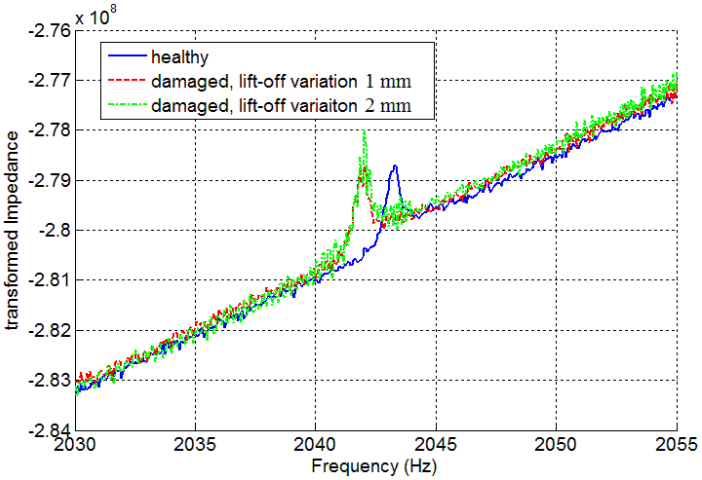

Figure 3-14. Transformed Impedance (unit: ohm^2) results under different lift-off oscillation magnitudes using the same scale factor.

In summary, in all the experimental cases under different lift-off variation conditions, we can observe that the proposed Transformed Impedance method can effectively to cancel the unwanted lift-off effect in magnetic impedance based fault detection.

3.6 Concluding Remarks

In this research, we propose a new data analysis method to compensate the lift-off effect in magnetic impedance based fault detection. We define a Transformed Impedance that essentially transforms the original magnetic impedance measured into a quantity that is immune to lift-off distance oscillation under a properly chosen scale factor. It is illustrated that this scale factor can be a constant which is determined by the electrical properties of the magnetic transducer and the structure, the initial given lift-off distance and the interested frequency range. Since the scale factor is independent of the lift-off oscillation, there is no need to measure and record the lift-off distances throughout measurements. Numerical analyses and experimental investigations are carried out to demonstrate the effectiveness of the proposed new approach.

Chapter 4 Fault Identification Using Piezoelectric Impedance Measurement and Model-based Intelligent Inference with Pre-screening

While piezoelectric impedance/admittance measurements have been used for fault detection and identification, the actual identification of fault location and severity remains to be a challenging topic. On one hand, the approach that uses these measurements entertains high detection sensitivity owing to the high-frequency actuation/sensing nature. On the other hand, high-frequency analysis requires high dimensionality in the model and the subsequent inverse analysis contains a very large number of unknowns which often renders the identification problem under-determined. A new fault identification algorithm is developed in this research for piezoelectric impedance/admittance based measurement. Taking advantage of the algebraic relation between the sensitivity matrix and the admittance change measurement, we devise a pre-screening scheme that can drastically reduce the fault parameter space. A Bayesian inference approach is then incorporated to pinpoint the fault location and severity with high computational efficiency. The proposed approach is examined and validated through case studies.

4.1 Introduction

The research on structural health monitoring (SHM) has attracted significant attention in engineering community, since unexpected structural failure may lead to catastrophic consequences. Piezoelectric transducers are widely adopted as sensors and actuators to facilitate fault detection and identification, primarily because of their advantages including high bandwidth, mostly linear property, and easy embedment within the host structures (Park et al, 2003). While they have been used in vibration-based approaches (Naidu and Soh, 2004; Jiang, et al, 2006; Zhao, et al, 2008) and wave propagation-based approaches (Giurgiutiu, 2005; Wang et al, 2008; Wandowski et al, 2011; Yu and Giurgiutiu, 2012; Yoon et al, 2012; Koduru and Rose, 2013), piezoelectric transducers have also been explored for

impedance/admittance-based methods (Giurgiutiu, 1999; Park et al, 2008; Wang and Tang, 2010a; Madhav and Kiong, 2010; Zhou and Zuo, 2012; Annamdas and Radhika, 2013). Owing to the electro-mechanical coupling, when we integrate (bond/embed) a piezoelectric transducer to a structure, the electrical impedance/admittance of the transducer is directly coupled with the impedance of the underlying structure. In an impedance/admittance-based fault detection scheme, a piezoelectric transducer is driven by a sinusoidal voltage sweep, and the electrical response (i.e., the resulted current) is measured to extract the impedance/admittance information. The change of piezoelectric impedance/admittance signature with respect to that under the healthy baseline state can be used as the fault indicator. This approach is based upon self-sensing interrogation, i.e., the piezoelectric transducer serves as the actuator and sensor simultaneously, thereby leading to highly sensitive fault detection.

An important module in an SHM system is decision making. For impedance/admittance-based fault detection, various fault indices built upon the comparisons of measurements before and after fault occurrence have been employed in the past to analyze the fault type/location/severity (Zagrai and Giurgiutiu, 2001; Tseng and Naidu, 2002; Naidu et al, 2006; Min et al, 2012; Wang et al, 2013). These measurement data-based methods only provide phenomenological characterizations of the impedance/admittance changes under specific fault patterns, and oftentimes cannot accurately relate the fault indices to the changes of local structural properties such as mass, stiffness, and damping ratio, etc (Wang and Tang, 2010b). The essence of impedance/admittance-based fault detection is the examination of structural health condition through local, stationary responses, which holds the potential of direct inverse analysis of structural faults using a first-principle model and online measurements. Therefore, alternatively, model-based methods have been formulated that use finite element or spectral element for discretization and employ inverse sensitivity analyses under the stationary condition (Wang and Tang, 2009; Kim and Wang, 2014). These model-based fault identification algorithms can result in the estimation of change of local, element-level structural properties such as mass and stiffness at the element level.

There are, however, noteworthy challenges in inverse-sensitivity-based fault identification. While the piezoelectric impedance/admittance-based sensing mechanism entertains high sensitivity because of the high-frequency responses induced/measured, the modeling and analysis of high-frequency responses in the context of fault identification is non-trivial. Although the spectral element method can be efficient theoretically in modeling high-frequency responses, it cannot be applied to structures with complex geometry and boundary conditions that are associated with complex wave motions. In a more conventional way of discretization using finite element, a very large number of elements are needed to establish the baseline model for credible prediction of high-frequency responses. On one hand, the structural properties of each segment in the first-principle model have to be identified because each segment or even each element is susceptible of fault occurrence, which yields a large number of unknowns. On the other hand, structural faults generally manifest themselves around the peaks of the piezoelectric impedance/admittance curves only, which means the input measurement information is relatively limited in practice. Additionally, it is mathematically challenging to select frequency points in impedance/admittance measurement to ensure the full rank of the sensitivity matrix (that relates fault location/severity with measurement) even if the number of frequency points is large. In such a situation, the inverse identification formulation may become under-determined (Kim and Wang, 2014). Although one may apply artificial constraints to seek for such as the least square solutions, these solutions may not reflect the true fault scenario. The inevitable measurement noise and modeling uncertainty further compound the difficulty in inverse analysis.

In recent years, there has been a stream of research efforts on utilizing Bayesian inference for parametric identification and model updating (Katafygiotis and Beck, 1998a and 1998b; Antoni et al, 2011). A typical Bayesian inference starts from pre-specifying the model parameters to be identified/updated with prior information in the form of probability density function (PDF). Then, by introducing measured response data, the assumed prior PDF is updated to the so-called posterior PDF that will be analyzed to yield the optimal model parameters. This avoids the problematic step of inverting the rank-deficient sensitivity matrix mentioned above, since the Bayesian model updating is facilitated through comparison of forward

analysis results under certain model parameter sample. Moreover, the inference is built upon the probabilistic framework that can naturally incorporate various sources of uncertainties. Katafygiotis and Beck (1998a) first formulated a Bayesian probabilistic procedure for model updating of a simple structure, followed by a number of studies that expand the formulation to tackle more complicated problems in finite element model updating (Becker et al, 2012; DiazDelao and Adhikari, 2012; Zhou and Tang, 2016). This type of methods has also been applied to the diagnosis of the fatigue crack growth and the model class selection (Mthembu et al, 2011； Zarate et al, 2012). It is worth noting that, despite its promising attributes, the application of Bayesian inference to piezoelectric impedance fault identification with finite element discretization remains to be challenging. Bayesian inference is a sampling-based approach, which requires repeated finite element analyses for all possible fault scenarios. Meanwhile, structural fault is continuous in nature. As such, in order to precisely quantify the severity of fault in one single segment, one would need to use a very large number of fault severity levels (Zhou et al, 2014). Combining the large number of fault severity levels with the usually large number of finite elements needed for high-frequency impedance/admittance analysis leads to a very large parameter space, and the computational cost involved for the repeated finite element analyses in this parameter space is simply prohibitive.

4.2 Research Overview

The goal of this research is to develop a new approach that can identify structural fault, including its location and severity, by using piezoelectric impedance sensing. In order for the approach to be applicable to general structures, finite element discretization is used in establishing the mathematical model. The novelty lies in that the fault identification algorithm is built upon the combination of inverse sensitivity formulation and the Bayesian inference technique. Bayesian inference is adopted in the identification procedure to avoid the usual drawback of direct inversion being under-determined and to deal with the inherent noise/uncertainties. Specifically, we take advantage of the mathematical relation between the sensitivity matrix and the impedance measurements in the presence of structural fault. Indeed, as will be shown later, when a structural fault occurs, the impedance change vector in theory must be proportional to

a column vector of the sensitivity matrix, and the ratio between these two vectors represents the fault severity. While the actual result may be complicated by measurement noise and uncertainties, this feature can reduce dramatically the size of the parameter space involved in Bayesian inference. To facilitate this new approach, proper vector similarity index is identified and employed in Bayesian inference formulation. The rest of this paper is organized as follows. Section 4.3 outlines the mathematical model of piezoelectric impedance/admittance sensing as well as the new identification algorithm. Section 4.4 provides numerical case studies and computational insights. Experimental validation is presented in Section 4.5. Section 4.6 summarizes the new findings.

4.3 Approach Formulation

4.3.1 Modeling of piezoelectric impedance/admittance sensing

The linear constitutive relation for the piezoelectric transducer used in this research is expressed as (IEEE 1987),

$$T_{ij} = c_{ijkl} S_{kl} - h_{kij} D_k \tag{4-1a}$$

$$E_i = -h_{ikl} S_{kl} + \beta_{ik} D_k \tag{4-1b}$$

where T_{ij}, S_{kl}, E_i and D_k are, respectively, the stress component, the strain component, the electrical field, and the electrical displacement. c_{ijkl} is the elastic constant, β_{ik} is the impermittivity, and h_{kij} is the piezoelectric constant that couples the mechanical domain with the electrical domain. In this research, for illustration purpose a single piezoelectric transducer is bonded to a structure to facilitate impedance/admittance sensing. Following the usual finite element discretization built upon the above constitutive relation, we can obtain the equations of motion of the transducer-structure integrated system (Junior et al, 2009; Zhou et al, 2014),

$$\mathbf{M}\ddot{\mathbf{q}} + \mathbf{C}\dot{\mathbf{q}} + \mathbf{K}\mathbf{q} + \mathbf{K}_{12} Q = \mathbf{0} \tag{4-2}$$

$$k_c Q + \mathbf{K}_{12}^T \mathbf{q} = V_{\text{in}} \tag{4-3}$$

where **q** is the structural displacement, Q is the electrical charge on the surface of the piezoelectric transducer, **M**, **K** and **C** are, respectively, the mass, stiffness, and damping matrices, k_c is the inverse of the capacitance of the piezoelectric transducer, and $\mathbf{K}_{12}$ is the coupling vector between the mechanical and electrical responses. Here V_{in} is the input excitation voltage.

Under harmonic excitation, Equations (4-2) and (4-3) can be readily transferred to the frequency domain. While the impedance and the admittance are inverse with each other, in this research without loss of generality we use the admittance measurement to formulate the new approach. The piezoelectric admittance can be derived as (Wang and Tang, 2009)

$$Y(\omega) = \frac{\dot{Q}}{V_{\text{in}}} = \frac{\omega i}{k_c - \mathbf{K}_{12}^T (\mathbf{K} - \omega^2 \mathbf{M} + i\omega \mathbf{C})^{-1} \mathbf{K}_{12}} \tag{4-4}$$

where ω is the voltage excitation frequency, and i is the imaginary unit. From Equation (4-4), one may observe that the piezoelectric admittance is coupled with the mechanical properties, i.e., the mass, stiffness and damping matrices, of the host structure. Therefore, the change of admittance information can be used to infer structural property changes. The admittance is a function of excitation frequency. In SHM practice, one applies frequency sweeping excitation while measuring the admittance value under a series of excitation frequency points. As a result, one can obtain a curve of admittance versus frequency. The admittance curve reaches peak values at frequencies close to structural resonances. At these frequencies, the admittances are more sensitive to structural fault, and the measurements have much higher signal-to-noise ratio than those elsewhere.

In model-based fault identification using finite element discretization, a fault is usually characterized as the percentage change of a local structural property, e.g., local stiffness or mass. One typically divides the host structure into a large number of segments and assigns each segment with a fault index for a structural property of concern. This will help dealing with the situation where a fault may cover multiple

elements. Without loss of generality, here we divide the structure into *m* segments and let the potential fault be represented by local stiffness reduction in a certain segment. We let the stiffness matrix of the structure with fault be represented as $\mathbf{K}_d$ where the subscript 'd' refers to the damaged state, which is then expressed as

$$\mathbf{K}_d = \sum_{j=1}^{m} \mathbf{K}_{sj}(1 - D_j) \tag{4-5}$$

In Equation (4-5), $\mathbf{K}_{sj}$ is the stiffness sub-matrix of the *j*-th segment ($j = 1, \cdots, m$) under the healthy condition, D_j is the fault index that indicates the percentage change of its stiffness due to fault occurrence, and the summation sign refers to the direct summation operation involved in finite element formulation. For the *j*-th segment, if D_j is identified to be a non-zero value based on the inverse analysis to be presented, we can conclude that fault occurs at the *j*-th segment with severity level D_j. The segment stiffness is related to the original elemental stiffness sub-matrices $\mathbf{K}_{ek}$ under healthy status (where the subscript 'e' refers to element) in the following manner,

$$\mathbf{K}_{sj} = \sum_{k=1}^{p} \mathbf{L}_k^T \mathbf{K}_{ek} \mathbf{L}_k \tag{4-6}$$

where *p* is the number of finite elements in each segment, and $\mathbf{L}_k$ is Boolean matrix indicating how the elemental sub-matrices are assembled into the global stiffness matrix. The reason we introduce segmentation is we intend to present a general formulation applicable to cases with very large number of finite elements. The admittance of the system with fault can then be written as

$$Y_d(\omega) = \frac{\dot{Q}}{V_{in}} = \frac{\omega i}{k_c - \mathbf{K}_{12}^T (\mathbf{K}_d - \mathbf{M}\omega^2 + \mathbf{C}\omega i)^{-1} \mathbf{K}_{12}} \tag{4-7}$$

Our objective is to identify D_j ($j = 1, \cdots, m$) by using the admittance change measurements. Hereafter we introduce the following notation of fault index vector,

$$\mathbf{D} = [D_1, \cdots, D_m]^T \tag{4-8}$$

4.3.2 Pre-screening by correlating inverse sensitivity matrix with admittance measurements

From Equations (4-4) and (4-7), we can develop mathematically the relation between admittance change and the change of structural property. Structural fault to be identified is generally insignificant in size, so Taylor series expansion can be adopted. The admittance of the system with fault can be expressed as

$$Y_d(\mathbf{D}) \approx Y(\mathbf{D} = \mathbf{0}) + \sum_{j=1}^{m} \frac{\partial Y}{\partial D_j} |_{\mathbf{D}=\mathbf{0}} \, D_j \tag{4-9}$$

where

$$\frac{\partial Y}{\partial D_j} |_{\mathbf{D}=\mathbf{0}} = \omega i [k_c - \mathbf{K}_{12}^T (\mathbf{K} - \omega^2 \mathbf{M} + i\omega \mathbf{C})^{-1} \mathbf{K}_{12}]^{-2} \mathbf{K}_{12}^T [\frac{\partial (\mathbf{K}_d - \omega^2 \mathbf{M} + i\omega \mathbf{C})^{-1}}{\partial D_j} |_{\mathbf{D}=\mathbf{0}}] \mathbf{K}_{12} \tag{4-10}$$

In Equation (4-10), we have

$$\frac{\partial (\mathbf{K}_d - \omega^2 \mathbf{M} + i\omega \mathbf{C})^{-1}}{\partial D_j} |_{\mathbf{D}=\mathbf{0}} = (\mathbf{K} - \omega^2 \mathbf{M} + i\omega \mathbf{C})^{-1} \mathbf{K}_{sj} (\mathbf{K} - \omega^2 \mathbf{M} + i\omega \mathbf{C})^{-1} \tag{4-11}$$

Combining Equations (4-9), (4-10), and (4-11), we can derive the following linear relation between the admittance change and the fault indices,

$$\Delta Y(\omega) = Y_d - Y(\mathbf{D} = \mathbf{0}) = \sum_{j=1}^{m} [\omega i (k_c - \mathbf{K}_{12}^T \mathbf{Z}_s^{-1} \mathbf{K}_{12})^{-2} \mathbf{K}_{12}^T \mathbf{Z}_s^{-1} \mathbf{K}_{sj} \mathbf{Z}_s^{-1} \mathbf{K}_{12}] D_j \tag{4-12}$$

where $\mathbf{Z}_s$ denotes the dynamic stiffness of the structure, i.e.,

$$\mathbf{Z}_s = \mathbf{K} - \omega^2 \mathbf{M} + i\omega \mathbf{C} \tag{4-13}$$

Equation (4-12) is valid for impedance change acquired at one specific excitation frequency point. Assuming the admittance change information at a total of *n* frequency points is available and grouping

together all the relations between the admittance change and the fault index vector, we have the following matrix form expression

$$\Delta \mathbf{Y} = \begin{bmatrix} \Delta Y(\omega_1) \\ \vdots \\ \Delta Y(\omega_n) \end{bmatrix} = \mathbf{S}_{n\times m}\mathbf{D} \tag{4-14}$$

where $\Delta\mathbf{Y}$ is an *n*-dimensional vector containing admittance changes at ω_j ($j = 1,\cdots,n$), $\mathbf{D}$ is the *m*-dimensional fault index vector, and $\mathbf{S}_{n\times m}$ is the sensitivity matrix whose entries are given as

$$s_{jk} = i\omega_j[k_c - \mathbf{K}_{12}^T\mathbf{Z}_s(\omega_j)^{-1}\mathbf{K}_{12}]^{-2}\mathbf{K}_{12}^T\mathbf{Z}_s(\omega_j)^{-1}\mathbf{K}_{sk}\mathbf{Z}_s(\omega_j)^{-1}\mathbf{K}_{12} \tag{4-15}$$

Theoretically, under each set of admittance change $\Delta\mathbf{Y}$, one can find the fault index vector $\mathbf{D}$ through matrix inversion of Equation (4-14). In reality, however, *n*, the number of admittance measurement frequency points, is usually smaller than *m*, the number of segments in the finite element model. Indeed, structural fault effect is mostly reflected around the peaks of the admittance curves that correspond to the structural resonances. Only a relatively small number of frequency points around those peaks can yield satisfying signal-to-noise ratio in admittance measurements. The number of segments, on the other hand, usually is large because of the large number of finite elements involved in the numerical model of high-frequency admittance analysis. As such, the inverse problem is under-determined (Kim and Wang, 2014), and usually yields infinitely many solutions mathematically. While one may introduce additional, artificial constraint to yield for example the least square solution, such solution may not reflect the true fault scenario. This is the underlying reason that inverse finite element analysis using the sensitivity matrix has not been widely accepted in piezoelectric impedance/admittance-based sensing.

In this research, instead of matrix inversion, we exploit the matrix relation shown in Equation (4-15) to develop a pre-screening scheme that can reduce the computational cost necessary for identifying the location and severity of fault. When conducting SHM, we usually aim at early detection of structural fault. In such a case, the probability of multiple faults occurrence is normally significantly lower than that of

single fault occurrence. Therefore, here in this research we assume single fault occurrence. The situation with multiple faults will be studied in the future. Under this assumption, mathematically, only one element in the fault index vector **D** will be non-zero. Assuming only the *k*-th segment in the structure is subjected to fault occurrence, observing Equation (4-14) we can conclude that we must have

$$\Delta \mathbf{Y} = D_k \mathbf{s}_k \tag{4-16}$$

where $\mathbf{s}_k$ denotes the *k*-th column of the sensitivity matrix $\mathbf{S}_{n\times m}$. In other words, when the *k*-th structural segment has fault, the admittance change vector must be linearly dependent to the *k*-th column of the sensitivity matrix, and the ratio of these two vectors is equal to the fault severity level. This gives rise to the idea of performing a pre-screening of possible fault scenario (i.e., location and severity) by using $\mathbf{S}_{n\times m}$ and $\Delta\mathbf{Y}$ directly without resorting to matrix inversion, which is summarized as follows.

1) We start from treating each segment as potential fault location candidate, and compute an *estimated* fault index for the *k*-th segment that is defined as

$$D_k^{\text{est}} = \text{mean}\left(\frac{\mathbf{\Delta} Y(\omega_j)}{s_{jk}}\right) \qquad (k = 1, \cdots, m) \tag{4-17}$$

If for a certain *k*, D_k^{est} is greater than 1 or less than 0, we can conclude that fault cannot occur at this *k*-th segment (since an actual fault index cannot be greater than 1 or less than 0).

2) We then analyze the similarity of the remaining columns of the sensitivity matrix with respect to the admittance change vector, and define a similarity index as

$$SI_k = \arcsin\left(\frac{\mathbf{s}_k^T \Delta \mathbf{Y}}{|\mathbf{s}_k| \cdot |\Delta \mathbf{Y}|} - 1\right) \tag{4-18}$$

where SI_k represents the directionality or similarity of the two vectors (Tang, 2005). As mentioned, $\mathbf{s}_k$ is the *k*-th column vector of the sensitivity matrix and $\Delta\mathbf{Y}$ is the measured admittance change vector. If $\mathbf{s}_k$ is linearly dependent on $\Delta\mathbf{Y}$, i.e., two vectors are similar, the

directionality SI_k is equal to 0. Larger difference in these two vectors leads to larger value of directionality SI_k.

Since measurement noise and modeling uncertainties always exist, SI_k may not be 0 even when fault indeed occurs at the *k*-th segment. Subsequently, we define a *relative* similarity function for the *k*-th column vector of the sensitivity matrix with respect to the admittance change vector as

$$P_k = \frac{e^{-|SI_k|}}{\sum_{j=1}^{m} e^{-|SI_j|}} \tag{4-19}$$

The numerator reflects the similarity corresponding to the *k*-th column vector, while the denominator reflects the summation of the similarities. Equation (4-19) then represents a relative comparison of the vector similarities. We can rank P_k in the descending order, and larger P_k value indicates higher likelihood of fault occurring at the *k*-th segment. In practice, one can choose a threshold value based on the distribution of P_k values, which will further reduce the candidate locations of fault occurrence.

4.3.3 Bayesian inference for fault identification based on pre-screening

The above mentioned pre-screening scheme is based on the approximated linear relationship between $\Delta\mathbf{Y}$ and $\mathbf{D}$. However, the true underlying relationship is nonlinear. In order to take the exact relationship into consideration and avoid the direct matrix inversion that is oftentimes under-determined mathematically, we propose a fault identification method inspired by the Bayesian approach. This method naturally incorporates the measurement and uncertainties into the formulation. The Bayesian inference approach is built upon the Bayes theorem (Katafygiotis and Beck, 1998a),

$$P(\boldsymbol{\theta}_i \mid y) = \frac{P(y \mid \boldsymbol{\theta}_i) P(\boldsymbol{\theta}_i)}{\sum_{j=1}^{N} P(y \mid \boldsymbol{\theta}_j) P(\boldsymbol{\theta}_j)} \tag{4-20}$$

where $\boldsymbol{\theta}$ represents the parameters that we would like to estimate, which is a random vector picking values from $\boldsymbol{\theta}_1$ to $\boldsymbol{\theta}_N$. Variable *y* represents the observations we have. $P(\boldsymbol{\theta})$ is the prior distribution function of

$\boldsymbol{\theta}$ representing our prior knowledge of the parameters. $P(y|\boldsymbol{\theta}_i)$ is the probability that we observe y if $\boldsymbol{\theta}_i$ represents the true parameter values. $P(\boldsymbol{\theta}_i|y)$ is the posterior probability of $\boldsymbol{\theta}_i$ given the observation y. Based on the Bayes theorem, a simple parameter estimation method would be to compute the posterior probability $P(\boldsymbol{\theta}|y)$ for all the possible values of $\boldsymbol{\theta}$ and then select the value with the highest posterior probability as the estimated value. For the fault identification problem in this research, the parameter vector $\boldsymbol{\theta}$ is in fact the fault index vector **D**. Moreover, we use the directionality between the measured admittance change and model prediction as the observation y which will be further discussed later. We would also point out that **D** contains both fault location and severity information. The location is discrete in our case but the severity is actually continuous. However, to form a tractable problem, we discretize the continuous severity and treat it as discrete.

The Bayesian inference is sampling based, the essential idea of which is to sample the model parameter space and find the set of parameters that best match the observations/measurements. In the context of fault identification here, the model parameters designate both the location and severity of fault. Recall that a fault index vector **D** is defined in Equations (4-5) and (4-8). In that definition, a non-zero component of the fault index vector indicates the occurrence of fault in the corresponding segment, i.e., the location, and the value of that component represents the severity. When we cast the identification problem into the Bayesian framework, in addition to sampling the location information which is natural in finite element formulation, we need to sample the severity of fault at each segment. Without the pre-screening procedure outlined in Section 4.3.2, the combination of these two samplings will yield prohibitive computational cost. A large number of segments are all possible locations of fault occurrence. Meanwhile, each segment may be subjected to fault severity level that is between 0 to 1, which requires a large sample size for the accurate quantification of actual fault severity level.

The advantages of the pre-screening procedure outlined in Section 4.3.2 are multi-fold. First, this will reduce dramatically the number of segments as possible location candidates. Moreover, for those segments that are deemed possible candidates for fault occurrence location, we also obtain preliminary estimations

of the respective severity levels. As such, instead of sampling fault severity in the entire interval between 0 and 1, we can sample a specific severity level of a segment (susceptible of fault occurrence) in the vicinity of the estimated severity level (as shown in Equation (4-17)). This will not only reduce the sample size for fault severity, but also increase the faulty severity quantification accuracy.

In Equation (4-20), the denominator is just a normalization factor, which is identical for different $\boldsymbol{\theta}$ values. Furthermore, if the prior probability $P(\boldsymbol{\theta})$ is selected as the uniform distribution, which reflects that we do not have specific prior knowledge on the fault location and severity within the feasible range, then the ranking of the posterior probability for different values of $\boldsymbol{\theta}$ is solely determined by $P(y|\boldsymbol{\theta}_i)$. Thus, the key step in Bayesian inference is the formulation and calculation of the likelihood function $P(y|\boldsymbol{\theta}_i)$ that is used to evaluate the agreement between the measurements and model prediction under sampled fault parameters. First, we use the directionality (between two vectors) of the similarity index (Tang, 2005) again to quantify the difference between the measured admittance change and model prediction, i.e.,

$$y(\mathbf{D}_i) = \arcsin\left(\frac{\Delta\tilde{\mathbf{Y}}(\mathbf{D}_i)^T \Delta\mathbf{Y}}{\left|\Delta\tilde{\mathbf{Y}}(\mathbf{D}_i)\right| \cdot \left|\Delta\mathbf{Y}\right|} - 1\right) \tag{4-21}$$

where $\Delta\tilde{\mathbf{Y}}(\mathbf{D}_i)$ is the predicted admittance change under fault parameter sample $\mathbf{D}_i$, and $\Delta\mathbf{Y}$ is the measured admittance change. If $\Delta\tilde{\mathbf{Y}}(\mathbf{D}_i)$ and $\Delta\mathbf{Y}$ are the same, the directionality will be 0. Larger difference in these two vectors leads to larger value of the similarity index $y(\mathbf{D}_i)$. The likelihood function is then formulated as a normal distribution of fault parameters with respect to the measurement data (Katafygiotis and Beck, 1998a; Zhou and Tang, 2016),

$$P(y_m|\mathbf{D}) = \frac{1}{\sigma\sqrt{2\pi}} e^{-\frac{[y(\mathbf{D})-y_m]^2}{2\sigma^2}} \tag{4-22}$$

$$y_m = y(\mathbf{D}_{\text{act}}) + \varepsilon \tag{4-23}$$

where $P(y_m \mid \mathbf{D})$ is the probabilistic distribution function obtained through sampling **D**, the fault index vector, over the sample space, σ is the standard deviation of the directionality due to measurement noise. y_m is the directionality based on measurement which can be expressed as shown in Equation (4-23), where $y(\mathbf{D}_{\text{act}})$ represents the model response under actual fault parameter $\mathbf{D}_{\text{act}}$, and ε is due to measurement error. $y(\mathbf{D}_{\text{act}})$ should be zero according to Equation (4-21), and thus y_m will be zero under ideal situation (i.e., without measurement error). In reality, however, measurement noise and modeling uncertainties always exist and therefore y_m may not be 0. Equation (4-22) indicates that a larger likelihood function value will be produced when sampled admittance change is closer to the measured admittance change, based on which the fault parameters can be quantitatively analyzed in a probabilistic manner.

4.4 Simulation Case Studies

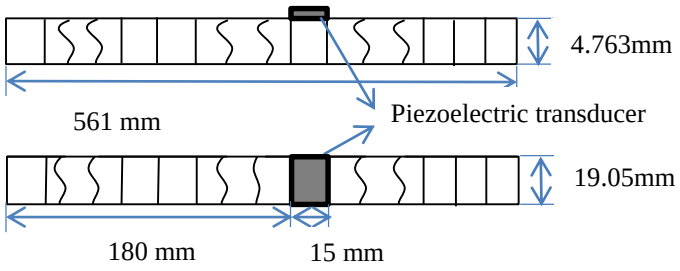

Figure 4-1. Case study setup.

In this section, we conduct case analysis using simulated data first, in order to highlight the effectiveness of the proposed approach. We intend to identify the fault location and severity of an aluminum plate with one edge fixed. The dimension of the plate is specified as: length 0.561 m, width 0.01905 m, and thickness 0.004763 m. The mass density and Young's modulus are, respectively, 2700 kg/m^3 and 68.9 GPa . A piezoelectric transducer is attached onto the plate as shown in Figure 4-1. The dimension of the transducer is: length 0.015 m, width 0.01905 m, and thickness 0.0014 m. The Young's moduli are $Y_{11} = 86$ GPa and $Y_{33} = 73$ GPa , the mass density is 9500 kg/m^3 , and the piezoelectric constant and

impermittivity constant are, respectively, $h_{31} = -1.0288 \times 10^9$ V/m and $\beta_{33} = 1.3832 \times 10^8$ m/F . The piezoelectric transducer is placed at 0.18 m from the fixed edge of the plate, and covers the entire width. The 20-node hexahedron element is used to develop the finite element model. The corresponding finite element model has 11,250 elements in total. The plate is then divided into 225 segments each containing 50 elements. Each segment is a possible fault location and we have 225 fault location candidates in total. The segments are numbered as shown in Figure 4-2.

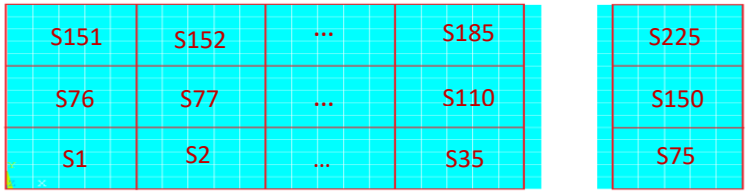

Figure 4-2. Finite element model of the plate and segmentation.

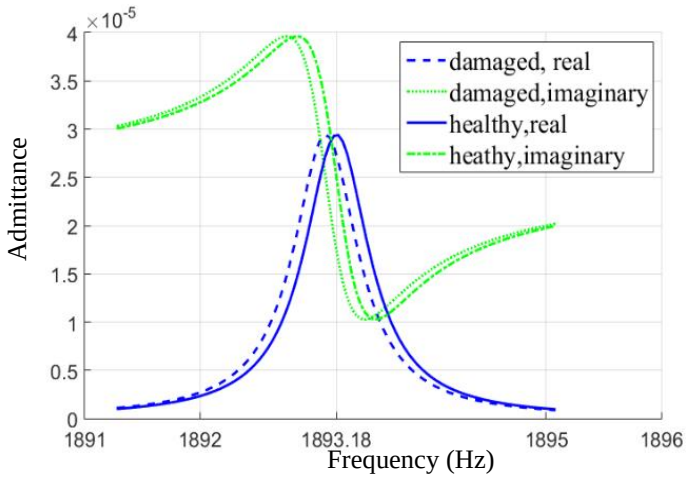

(a)Around the 14th natural frequency

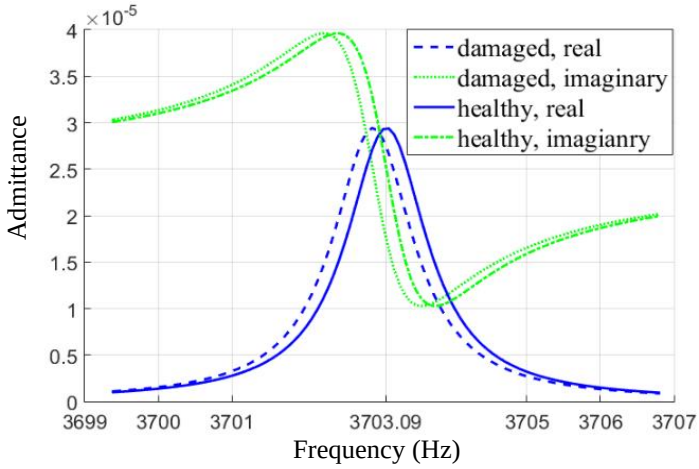

(b)Around the 20th natural frequency

Figure 4-3. Admittance curves before and after fault occurrence (Simulation).

In the first case analysis using simulated data, a fault with severity of 1.64% (of segment stiffness reduction) is injected to the 110th segment. As mentioned, the admittance changes due to fault occurrence are most observable around the admittance peaks. Here we collect the admittance data around the peaks corresponding to the 14th and 20th plate resonances, i.e., 1893.18 Hz and 3703.09 Hz. The admittance values at 100 frequency points around each resonant frequency are employed in the analysis. Figure 4-3 shows the admittance values before and after fault occurrence. We first conduct the pre-screening process. After the sensitivity matrix is computed, the estimated fault index for each segment is calculated based on the comparison of the admittance change vector with respect to each column of the sensitivity matrix (using Equation (4-17)), followed by the calculation of similarity index for each segment (based on Equation (4-18)). It is worth mentioning that the admittance values extracted are complex numbers with real and imaginary parts. Both the real part and imaginary part of the admittance are subjected to changes when fault occurs, and contain useful information for fault identification. Here we separately calculate the similarity indices for the real part and imaginary part, and obtain a cumulative similarity index using the multiplication of these two values. Figure 4-4 shows the relative similarity index value for each segment. We can observe that the actual fault location, i.e., the 110th segment, has the highest similarity index value

which indicates that it has high likelihood of being the fault location. The fault severity index values for segments with high relative similarity values are tabulated in Table 4-1. From Table 4-1, we can find that the estimated fault index value for the 110th segment is very close to the actual value. Nevertheless, from Figure 4-4 we can also observe that, besides the 110th segment, a number of other segments have high relative similarity values. For these segments, the pre-screening step predicts possible fault severity levels that are summarized in Table 4-1.

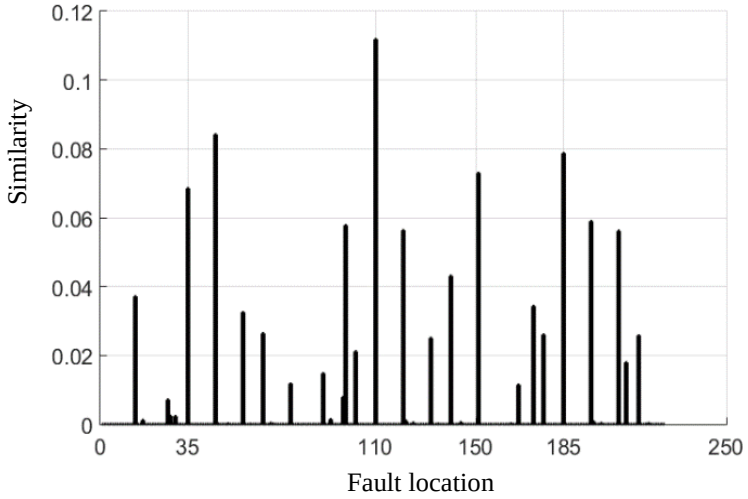

Figure 4-4. Similarity prediction through pre-screening (Simulated data, Case 1 in Section 4.4).

We now proceed to the second step of fault identification, the Bayesian inference. Recall that the purpose of the pre-screening step is to reduce the size of the parameter space to be sampled. The segments with high relative similarity index values (i.e., the similarity between the admittance change and a column of the sensitivity matrix) are possible candidates of fault location. We then take the top 10 segments shown in Figure 4-4 as the location candidates. For each fault location candidate, we also have obtained the estimated fault severity index. Hence, we only need to sample the fault severity in the vicinity of the estimated severity level. A total of 13 fault severity candidates centered around each estimated faulty index (with interval being 0.001%) are adopted. As such, the size of the reduced fault parameter space is 10×13. Apparently, without the pre-screening step, all 225 segments will need to be sampled, and an extremely

large number of severity levels need to be sampled if one wants to pinpoint the severity level. This will lead to prohibitive computational cost. We then conduct Bayesian inference within the reduced parameter space. In this case study, the measurement error of the directionality is assumed as ambient noise that can be modeled as a normal distribution with zero mean, and the corresponding variance is assumed as 1×10^{-6}. According to Equation (4-23), the measured directionality y_m is assumed to be zero. The prior probability is selected as the uniform distribution. By using Equation (4-20), we can eventually obtain the posterior distribution of the fault parameter as shown in Figure 4-5. We can see that the Bayesian inference yields the unique solution, and accurately predicts that the fault location is the 110th segment and the fault severity is 1.64%.

Table 4-1. Similarity prediction through pre-screening (Simulated data, Case 1 in Section 4.4)

Segment #	Similarity	Fault severity
110	0.115	0.01644
46	0.086	0.01350
185	0.081	0.01616
151	0.075	0.00381
35	0.070	0.01734
196	0.061	0.01396
98	0.059	0.03077
121	0.058	0.01402
207	0.058	0.01280
140	0.044	0.02572
14	0.038	0.02159
173	0.035	0.03156
57	0.033	0.01328
65	0.027	0.01103
177	0.027	0.00955

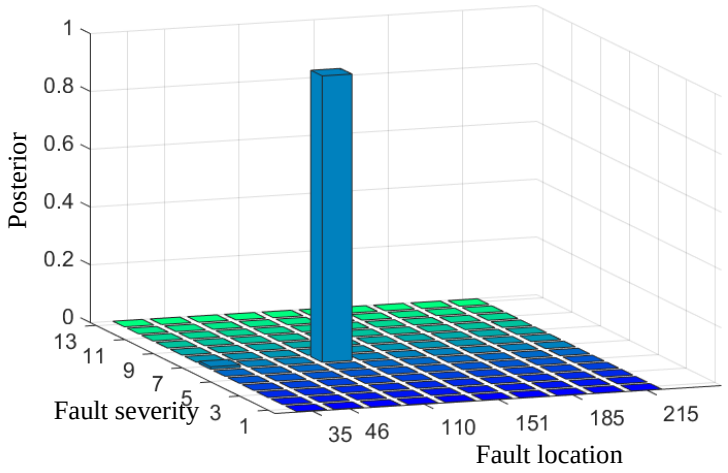

Figure 4-5. Posterior probability distribution from Bayesian inference (Simulated data, Case 1 in Section 4.4).

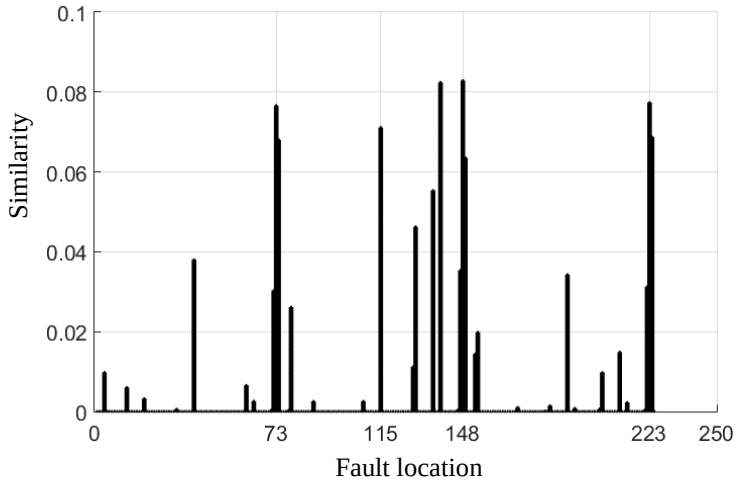

Figure 4-6. Similarity prediction through pre-screening (Simulated data, Case 2 in Section 4.4).

In the second case analysis using simulated data, the fault location is moved to the 115th segment, and the fault severity is set to be a larger value, 2.167%. We carry out the pre-screening process first. From Figure 4-6, we can find that the actual fault location has high relative similarity value, i.e., the 5th highest, but it is not the highest one. This is because of the approximation nature of the sensitivity matrix that

reflects only the linearized relation between the fault and the admittance change. As a result, the admittance change vector may not be precisely proportional to a certain column of the sensitivity matrix. The estimated fault index values are tabulated in Table 4-2. Similarly, we reduce the parameter space size by selecting the top 5 location candidates and using 11 fault severity levels centered around each estimated fault index (with interval being 0.001%) in Bayesian inference. The posterior distribution obtained is shown in Figure 4-7. Once again, the Bayesian inference yields the unique solution after comparing the admittance change with model predictions within the parameter space, and accurately predicts that the fault is located at the 115th segment and with a severity of 2.167%.

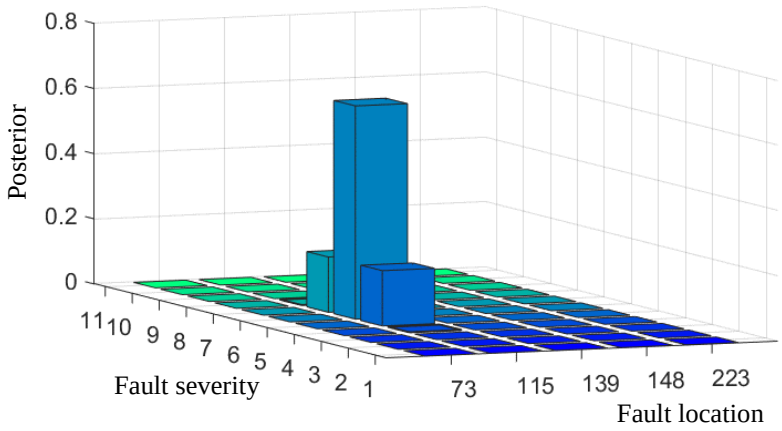

Figure 4-7. Posterior probability distribution from Bayesian inference (Simulated data, Case 2 in Section 4.4).

Table 4-2. Similarity prediction through pre-screening (Simulated data, Case 2 in Section 4.4)

Segment #	Similarity	Fault severity
148	0.083	0.06589
139	0.082	0.03050
223	0.077	0.06446
73	0.077	0.06351
115	0.071	0.02144
224	0.069	0.27518
74	0.068	0.27239
149	0.064	0.28541
136	0.055	0.03132
129	0.046	0.02477
40	0.038	0.02030
147	0.035	0.02698
190	0.034	0.02167
222	0.031	0.02660
72	0.030	0.02624

4.5 Experimental Validation

In this section we report experimental case analysis using actual piezoelectric admittance data measured. The setup of the experiment is consistent with that employed in Section 4.4, and all geometry and material parameters are the same. To extract the piezoelectric admittance, a small resistor R (100 Ω) is connected in serial to the transducer to measure the voltage drop across it (Figure 4-8(a)), and the current in the circuit can be obtained which then yields the admittance information. A signal analyzer (Agilent 35670A) with a source channel and the sweep sine capability is employed. The source channel is used to generate the sinusoidal voltage V_{in} sent to the piezoelectric transducer, and the output voltage V_{out} across the resistor is recorded. Hence, the experimentally exacted admittance is

$$Y_{\text{exp}} = \frac{I}{V_{\text{in}}} = \frac{V_{\text{out}} / R_{\text{s}}}{V_{\text{in}}} \tag{4-24}$$

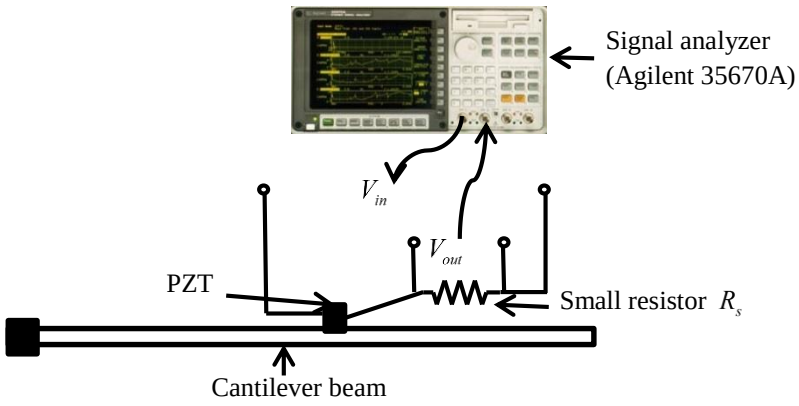

(a)

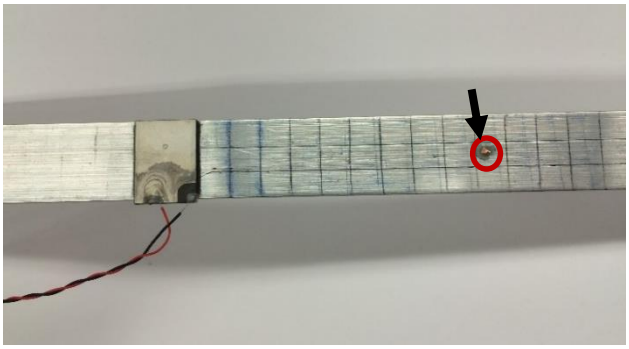

(b)

Figure 4-8. Experimental setup.

Since the fault identification algorithm proposed is model based, we need to calibrate the finite element model of the healthy structure to match the experimental testbed. In experiment, non-perfect boundary condition is one of the main factors inducing model error. We update the boundary condition of the plate with one edge fixed. A numerical optimization is performed to identify the stiffness values at the fixed edge to minimize the errors of the natural frequencies between the measurement and model prediction. In this testbed, there are 125 nodes on the fixed edge and each node has 3 degrees of freedom. The stiffness values corresponding to these 375 degrees of freedom are updated using the first 10 natural frequencies of the transversal modes of the plate. The natural frequencies of the plate before and after model updating are listed in Table 4-3.

Table 4-3. Natural frequencies Comparison

Experimental results (Hz)	Finite element results	
	Original (Hz)	Updated (Hz)
12.20	12.46	12.08
74.00	76.50	74.29
209.50	213.95	208.22
414.70	424.47	413.34
682.80	699.14	681.33
1017.10	1040.69	1015.93
1893.18	1936.73	1893.58
2428.44	2482.46	2429.08
3033.20	3104.30	3034.05
3703.09	3781.89	3704.05

Table 4-4. Similarity prediction through pre-screening (Experimental data, Case 1 in Section 4.5)

Segment #	Similarity	Fault severity
110	0.097	0.01590
35	0.095	0.01635
46	0.089	0.01286
185	0.087	0.01534
151	0.077	0.00363
173	0.069	0.02920
196	0.062	0.01333
65	0.061	0.01207
215	0.059	0.04800
121	0.050	0.01334
207	0.045	0.01216
140	0.035	0.02446
98	0.030	0.02951
14	0.025	0.02062
57	0.023	0.01259

In order to avoid the variation of boundary condition throughout the experimental study, instead of cutting the plate to reduce the local stiffness, here we add a small mass to the plate to emulate the fault condition. Mathematically, this can result in equivalently the same resonant frequency shift and admittance change as a local stiffness reduction would. In the first experimental case, a 0.6 g mass is attached onto the plate at location corresponding to the 110th segment in the model (Figure 4-8(b)), which causes the same resonant frequency change as that due to a 1.6% local stiffness loss. The admittances are measured around the 14th and 20th resonant frequencies. The admittance values at 100 frequency points around each resonant frequency are recorded before and after fault occurrence. Figure 4-9 shows the measured admittance changes. The measured admittance changes are used as input to the pre-screening procedure to provide preliminary estimations of fault location candidates and severity levels which are shown in Figure 4-10 and Table 4-4. The pre-screening indicates that the 110th segment has the highest similarity index. There are several other segments that have high similarity indices as well. The segments with the top 10 similarity index values are chosen as the location candidates for the following Bayesian inference. Meanwhile, a total of 13 fault severity levels for each fault location candidate are taken into account, which are centered around the corresponding estimated fault index values with interval being 0.001%. The measured directionality

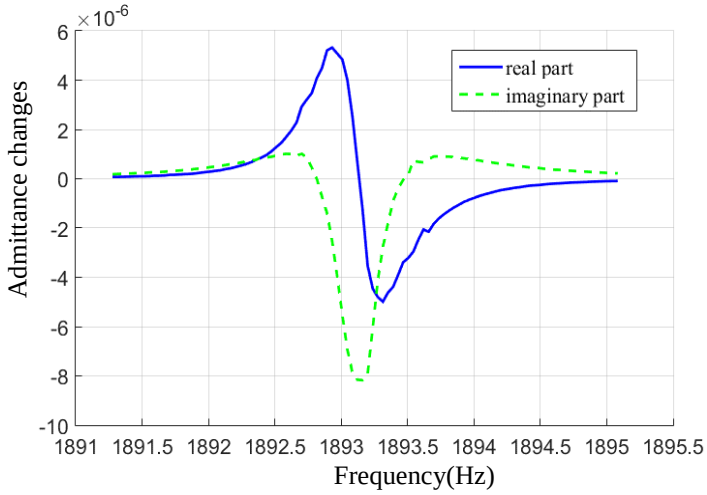

(a) Around the 14th natural frequency

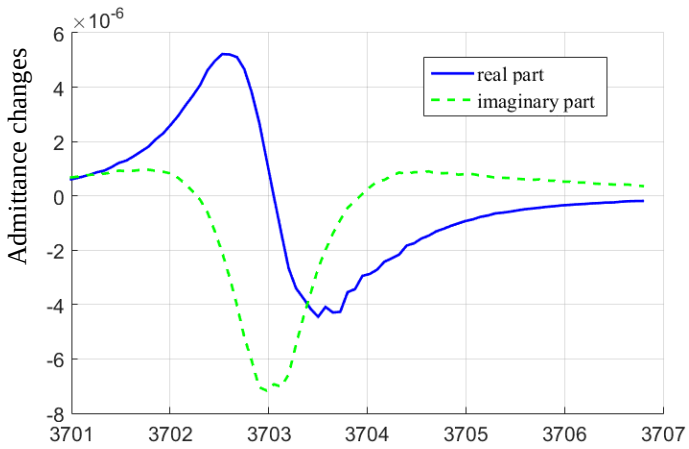

(b) Around the 20th natural frequency

Figure 4-9. Admittance change curves (Experiment).

y_m is the directionality between the experimental measured admittance and the admittance prediction for the heathy structure. The variance is again assumed to be 1×10^{-6}. Figure 4-11 shows the Bayesian inference results. Clearly, the probability of the actual fault parameter, i.e., severity level 5 at the 110th segment, is much higher than the other fault parameter. In other words, our approach predicts that a fault with severity 1.589% occurs at the 110th segment. This is very close to the actual fault condition.

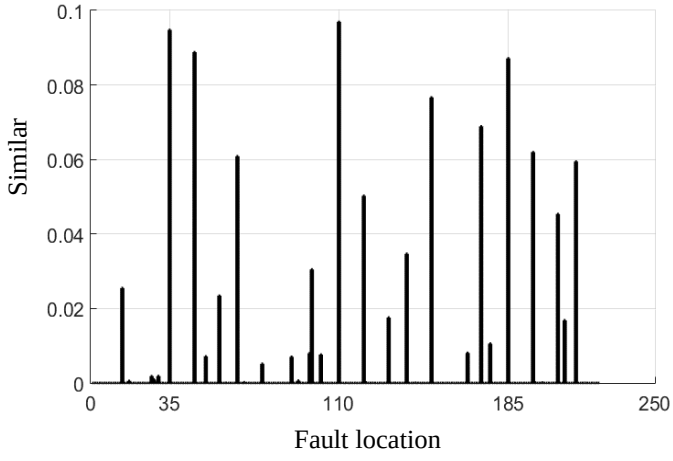

Figure 4-10. Similarity prediction through pre-screening (Experimental data, Case 1 in Section 4.5).

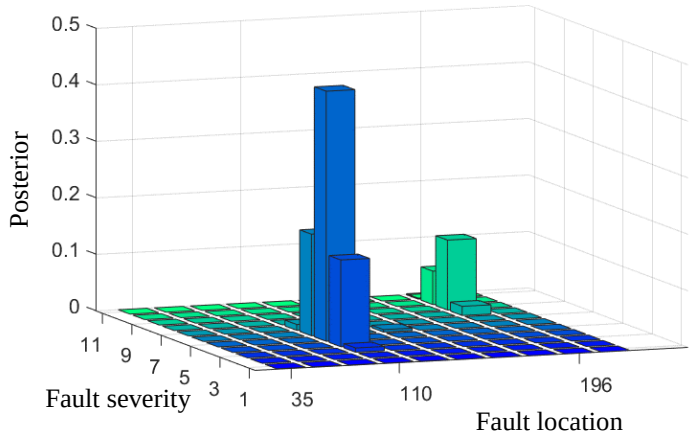

Figure 4-11. Posterior probability distribution from Bayesian inference (Experimental data, Case 1 in Section 4.5).

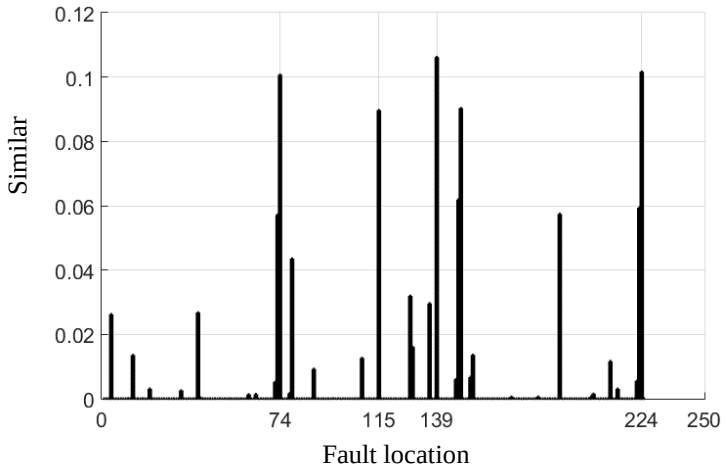

Figure 4-12. Similarity prediction through pre-screening (Experimental data, Case 2 in Section 4.5).

In the second experimental case, the 0.6 g mass is added onto the plate at the 115th segment, which causes the same resonant frequency change as that due to a 2.5% local stiffness loss at that location. Similarly, we collect the admittance measurements around the 14th and the 20th resonant frequencies. The pre-screening results are shown in Figure 4-12 and Table 4-5. In this case, since the fault severity estimations have larger values, we slightly increase the range of severity level parameter and employ 17

severity levels around the estimated severity values obtained from the pre-screening with interval being 0.002%. After conducting Bayesian inference, the posterior distributions of fault parameters are plotted in

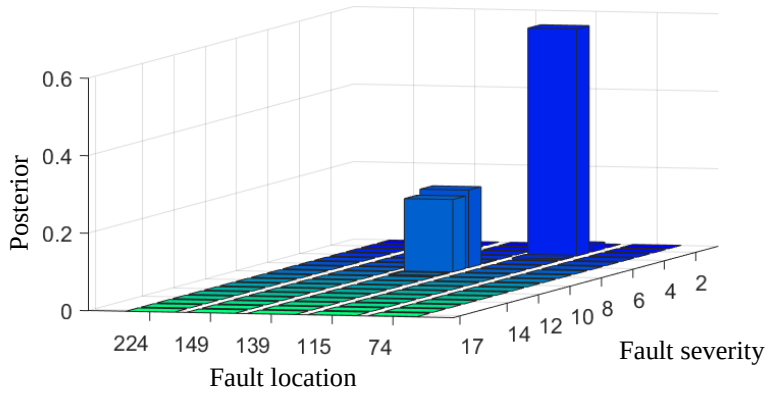

Figure 4-13. Posterior probability distribution from Bayesian inference (Experimental data, Case 2 in Section 4.5).

Table 4-5. Similarity prediction through pre-screening (Experimental data, Case 2 in Section 4.5)

Segment #	Similarity	Fault severity
139	0.106	0.03436
224	0.102	0.31259
74	0.101	0.30981
149	0.090	0.32868
115	0.090	0.02437
148	0.062	0.07478
223	0.059	0.07381
190	0.057	0.02798
73	0.057	0.07282
79	0.044	0.04024
128	0.032	0.08284
136	0.030	0.03709
40	0.027	0.03242
4	0.026	0.04603
129	0.016	0.02912

Figure 4-13. We can observe that the probability of the actual fault parameter, location at the 115th segment and severity level 2 corresponding to 2.425% fault severity is much higher than other combinations. This is again very close to the actual fault condition.

4.6 Concluding Remarks

In this research, a new fault identification algorithm is formulated for piezoelectric impedance/admittance-based structural health monitoring. Instead of directly inverting the sensitivity matrix, we employ the sensitivity matrix to conduct a pre-screening by comparing the admittance change vector with the columns of the sensitivity matrix. Such comparison can yield a small number of location candidates and severity estimations of the fault. We then apply the Bayesian inference framework to identify the actual fault location and severity within the much reduced fault parameter space. Our case studies indicate that the new approach can efficiently and accurately identify fault occurrence.

Chapter 5 Fault Identification Using Experimentally Extracted Sensitivity Matrix and Intelligent Inference

Piezoelectric impedance/admittance measurements have been widely used for fault detection, since they entertain high detection sensitivity owing to the high-frequency actuation/sensing nature. However, the actual identification of fault location and severity remains to be a challenging topic. High-frequency analysis requires high dimensionality in the model which often introduces a very large number of unknowns for the fault identification problem and renders the inverse analysis under-determined. The inevitable model errors further compound the difficulty in such model-based inverse analysis. A new fault identification algorithm is developed in this research for piezoelectric impedance/admittance based measurement. First, only a few columns of the sensitivity matrix are experimentally extracted. The Gaussian process is then employed to predict the sensitivity at all possible fault location. Next, Bayesian inference approach is incorporated to pinpoint the fault location and severity by taking advantage of the algebraic relation between the sensitivity matrix and the admittance change measurement. The proposed approach is examined and validated through case studies.

5.1 Introduction

Due to their advantages including high bandwidth, mostly linear property, and easy embedment within the host structures (Park et al, 2003), piezoelectric transducers have been widely adopted to facilitate structural health monitoring (SHM). While they have been used in vibration-based approaches (Jiang, et al, 2006; Zhao, et al, 2008) and wave propagation-based approaches (Giurgiutiu, 2005; Wang et al, 2008; Wandowski et al, 2011; Yu and Giurgiutiu, 2012; Yoon et al, 2012; Koduru and Rose, 2013), piezoelectric transducers have also been explored for impedance/admittance-based methods (Giurgiutiu, 1999; Park et al, 2008; Wang and Tang, 2010a; Madhav and Kiong, 2010; Zhou and Zuo, 2012; Annamdas and Radhika, 2013). Owing to the electro-mechanical coupling, when we integrate (bond/embed) a piezoelectric

transducer to a structure, the electrical impedance/admittance of the transducer is directly coupled with the mechanical impedance of the underlying structure. In an impedance/admittance-based fault detection scheme, a piezoelectric transducer is driven by a sinusoidal voltage sweep, and the electrical response (i.e., the resulted current) is measured to extract the impedance/admittance information. The change of piezoelectric impedance/admittance signature with respect to that under the healthy baseline state can be used as the fault indicator. This approach is based upon self-sensing interrogation, i.e., the piezoelectric transducer serves as the actuator and sensor simultaneously, thereby leading to highly sensitive fault detection.

An important module in an SHM system is decision making. For impedance/admittance-based fault detection, various fault indices built upon the comparisons of measurements before and after fault occurrence have been employed in the past to analyze the fault type/location/severity (Zagrai and Giurgiutiu, 2001; Tseng and Naidu, 2002; Min et al, 2012; Wang et al, 2013). These measurement data-based methods only provide phenomenological characterizations of the impedance/admittance changes under specific fault patterns, and oftentimes cannot accurately relate the fault indices to the changes of local structural properties such as mass, stiffness, and damping ratio, etc (Wang and Tang, 2010b). Alternatively, model-based methods have been formulated that use finite element or spectral element for discretization and employ inverse sensitivity analyses under the stationary condition (Wang and Tang, 2009; Kim and Wang, 2014). These model-based fault identification algorithms can result in the estimation of change of local, element-level structural properties such as mass and stiffness at the element level. There are, however, noteworthy challenges in inverse-sensitivity-based fault identification. While the piezoelectric impedance/admittance-based sensing mechanism entertains high sensitivity because of the high-frequency responses induced/measured, the modeling and analysis of high-frequency responses in the context of fault identification is non-trivial. In the general finite element analysis, a very large number of elements are needed to establish the baseline model for credible prediction of high-frequency responses. On one hand, the structural properties of each segment in the first-principle model have to be identified because each

segment or even each element is susceptible of fault occurrence, which yields a large number of unknowns. On the other hand, structural faults generally manifest themselves around the peaks of the piezoelectric impedance/admittance curves only, which means the input measurement information is relatively limited in practice. In such a situation, the inverse identification formulation may become under-determined (Kim and Wang, 2014). Although one may apply artificial constraints to seek for such as the least square solutions, these solutions may not reflect the true fault scenario. The inevitable measurement noise and modeling uncertainty further compound the difficulty in inverse analysis. Recently, Bayesian inference is adopted in the identification procedure to avoid the usual drawback of direct inversion being under-determined and to deal with the inherent noise/uncertainties (Vanik et al, 2000; Ching and Beck, 2004; Moore et al, 2011; Zarate et al, 2012). A typical Bayesian inference starts from pre-specifying the model parameters to be identified/updated with prior information in the form of probability density function (PDF). Then, by introducing measured response data, the assumed prior PDF is updated to the so-called posterior PDF that will be analyzed to yield the optimal model parameters. This avoids the problematic step of inverting the rank-deficient sensitivity matrix mentioned above, since the Bayesian model updating is facilitated through comparison of forward analysis results under certain model parameter sample. Moreover, the inference is built upon the probabilistic framework that can naturally incorporate various sources of uncertainties. It is worth noting that, despite its promising attributes, the application of Bayesian inference to piezoelectric impedance fault identification with finite element discretization remains to be challenging. Bayesian inference is a sampling-based approach, which requires repeated finite element analyses for all possible fault scenarios. Meanwhile, structural fault severity is continuous in nature. As such, in order to precisely quantify the severity of fault in one single segment, one would need to use a very large number of fault severity levels (Zhou et al, 2014). Combining the large number of fault severity levels with the usually large number of finite elements needed for high-frequency impedance/admittance analysis leads to a very large parameter space, and the computational cost involved for the repeated finite element analyses in this parameter space is simply prohibitive. Recently, a novel fault identification algorithm, which is built upon the combination of inverse sensitivity formulation and the Bayesian inference technique,

is developed to alleviate the computational burden (Shuai et al, 2016). The sensitivity matrix is employed to conduct a pre-screening by comparing the admittance change vector with the columns of the sensitivity matrix. Such comparison can yield a small number of location candidates and severity estimations of the fault. Then the Bayesian inference framework is applied to identify the actual fault location and severity within the much reduced fault parameter space.

5.2 Research Overview

However, there is a remaining challenge in such model based methods. Since these model based methods are implemented by comparison of model predictions and experimental measurements, the identification performance is highly depended on the model accuracy. Nevertheless, the discrepancies between model prediction and experimental measurements are inevitable, which are due to a number of factors, ranging from the noise in measurement, normal variation of the structure, to the error in the finite element model itself. Model updating of the deterministic model is a potential way to minimize these discrepancies (Mottershead and Friswell, 1993; Sinha and Friswell, 2002; Zarate and Caicedo,2008;). However, such model updating, which is based upon the difference between current model prediction and the corresponding response measurement under the same operating condition, is also an underdetermined inverse problem in general (Beck and Katafygiotis,1998; Beck and Au, 2002; Zhang et al,2011). By reviewing the model based fault identification method, we can observe that the sensitivity matrix is the desired mathematic model. If we can build the sensitivity matrix directly from experimental measurements, we may not just bypass the onerous job of building an accurately finite element model, but also intuitively avoid the discrepancies between the mathematic model and experiment. Then the goal of this research is to develop a new approach that can identify structural fault efficiently by using piezoelectric impedance sensing. This new algorithm is based on Shuai and Tang's work (Shuai et al, 2016), which adopt Bayesian inference in the identification procedure to avoid the usual drawback of direct inversion being under-determined and to deal with the inherent noise/uncertainties. The novelty lies in that the sensitivity matrix is built upon experimentally measured admittance changes and implemented by the Gaussian process (GP)

for regression. The rest of this paper is organized as follows. Section 5.3 outlines the mathematical model of piezoelectric impedance/admittance sensing as well as the new identification algorithm. Section 5.4 provides numerical case studies and computational insights. Section 5.6 summarizes the new findings.

5.3 Approach Formulation

5.3.1 Piezoelectric admittance-based fault identification by using sensitivity matrix

The linear constitutive relation for the piezoelectric transducer used in this research is expressed as (IEEE 1987),

$$T_{ij} = c_{ijkl} S_{kl} - h_{kij} D_k \tag{5-1a}$$

$$E_i = -h_{ikl} S_{kl} + \beta_{ik} D_k \tag{5-1b}$$

where T_{ij}, S_{kl}, E_i and D_k are, respectively, the stress component, the strain component, the electrical field, and the electrical displacement. c_{ijkl} is the elastic constant, β_{ik} is the impermittivity, and h_{kij} is the piezoelectric constant that couples the mechanical domain with the electrical domain. In this research, for illustration purpose a single piezoelectric transducer is bonded to a structure to facilitate impedance/admittance sensing. Following the usual finite element discretization built upon the above constitutive relation, we can obtain the equations of motion of the transducer-structure integrated system (Junior et al, 2009; Zhou et al, 2014),

$$\mathbf{M}\ddot{\mathbf{q}} + \mathbf{C}\dot{\mathbf{q}} + \mathbf{K}\mathbf{q} + \mathbf{K}_{12} Q = \mathbf{0} \tag{5-2}$$

$$k_c Q + \mathbf{K}_{12}^T \mathbf{q} = V_{\text{in}} \tag{5-3}$$

where $\mathbf{q}$ is the structural displacement, Q is the electrical charge on the surface of the piezoelectric transducer, $\mathbf{M}$, $\mathbf{K}$ and $\mathbf{C}$ are, respectively, the mass, stiffness, and damping matrices, k_c is the inverse of

the capacitance of the piezoelectric transducer, and $\mathbf{K}_{12}$ is the coupling vector between the mechanical and electrical responses. Here V_{in} is the input excitation voltage.

Under harmonic excitation, Equations (5-2) and (5-3) can be readily transferred to the frequency domain. While the impedance and the admittance are inverse with each other, in this research without loss of generality we use the admittance measurement to formulate the new approach. The piezoelectric admittance can be derived as (Wang and Tang, 2009)

$$Y(\omega) = \frac{\dot{Q}}{V_{\text{in}}} = \frac{\omega i}{k_c - \mathbf{K}_{12}^T(\mathbf{K} - \omega^2\mathbf{M} + i\omega\mathbf{C})^{-1}\mathbf{K}_{12}} \tag{5-4}$$

where ω is the voltage excitation frequency, and i is the imaginary unit. From Equation (5-4), one may observe that the piezoelectric admittance is coupled with the mechanical properties, i.e., the mass, stiffness and damping matrices, of the host structure. Therefore, the change of admittance information can be used to infer structural property changes. The admittance is a function of excitation frequency. In SHM practice, one applies frequency sweeping excitation while measuring the admittance value under a series of excitation frequency points. As a result, one can obtain a curve of admittance versus frequency. The admittance curve reaches peak values at frequencies close to structural resonances. At these frequencies, the admittances are more sensitive to structural fault, and the measurements have much higher signal-to-noise ratio than those elsewhere.

In model-based fault identification using finite element discretization, a fault is usually characterized as the percentage change of a local structural property, e.g., local stiffness or mass. One typically divides the host structure into a large number of segments and assigns each segment with a fault index for a structural property of concern. Without loss of generality, here we divide the structure into *m* segments and let the potential fault be represented by local mass density increasing. The mass matrix of the structure with fault is then expressed as

$$\mathbf{M}_d = \sum_{j=1}^{m} \mathbf{M}_{sj}(1 + D_j) \tag{5-5}$$

In Equation (5-5), $\mathbf{M}_{sj}$ is the mass sub-matrix of the *j*-th segment ($j = 1, \cdots, m$), D_j is the fault index that indicates the percentage change of its mass due to fault occurrence, and the summation sign refers to the direct summation operation involved in finite element formulation. For the *j*-th segment, if D_j is identified to be a non-zero value based on the inverse analysis to be presented, we can conclude that fault occurs at the j-th segment with severity level D_j. The admittance of the system with fault can then be written as

$$Y_d(\omega) = \frac{\dot{Q}}{V_{in}} = \frac{\omega i}{k_c - \mathbf{K}_{12}^T(\mathbf{K} - \mathbf{M}_d\omega^2 + \mathbf{C}\omega i)^{-1}\mathbf{K}_{12}} \tag{5-6}$$

Our objective is to identify D_j ($j = 1, \cdots, m$) by using the admittance change measurements. Hereafter we introduce the following notation of fault index vector.

$$\mathbf{D} = [D_1, \cdots, D_m]^T \tag{5-7}$$

From Equations (5-4) and (5-6), we can develop mathematically the relation between admittance change and the change of structural property. The structural fault to be identified is generally insignificant in size, so Taylor series expansion can be adopted. Assuming the admittance change information at a total of *n* frequency points is available and grouping together all the relations between the admittance change and the fault index vector, we have the following matrix form expression (Shuai and Tang, 2016)

$$\Delta\mathbf{Y} = \begin{bmatrix} \Delta Y(\omega_1) \\ \vdots \\ \Delta Y(\omega_n) \end{bmatrix} = \mathbf{S}_{n\times m}\mathbf{D} \tag{5-8}$$

where $\Delta\mathbf{Y}$ is an *n*-dimensional vector containing admittance changes at ω_k ($k = 1, \cdots, n$), $\mathbf{D}$ is the *m*-dimensional fault index vector, and $\mathbf{S}_{n\times m}$ is the sensitivity matrix whose entries are given as

$$s_{kj} = i\omega_k[k_c - \mathbf{K}_{12}^T\mathbf{Z}_s(\omega_k)^{-1}\mathbf{K}_{12}]^{-2}\mathbf{K}_{12}^T\mathbf{Z}_s(\omega_k)^{-1}(\omega_k^2\mathbf{M}_{sj})\mathbf{Z}_s(\omega_k)^{-1}\mathbf{K}_{12} \tag{5-9}$$

$$\mathbf{Z}_s(\omega_k) = \mathbf{K} - \omega_k^2\mathbf{M} + i\omega_k\mathbf{C} \tag{5-10}$$

Theoretically, under each set of admittance change $\Delta\mathbf{Y}$, one can find the fault index vector **D** through matrix inversion of Equation (5-8). In reality, however, only a relatively small number of frequency points around the peaks of the admittance curves (which correspond to the structural resonances) can yield satisfying signal-to-noise ratio in admittance measurements. On the other hand, the number of segments usually is large because of the large number of finite elements involved in the numerical model of high-frequency admittance analysis. This means that n, the number of admittance measurement frequency points, is usually smaller than m, the number of segments in the finite element model. As such, the inverse problem is under-determined (Kim and Wang, 2014), and usually yields infinitely many solutions mathematically. While one may introduce additional, artificial constraint to yield for example the least square solution, such solution may not reflect the true fault scenario. This is the underlying reason that inverse finite element analysis using the sensitivity matrix has not been widely accepted in piezoelectric impedance/admittance-based sensing.

Recently, a novel fault identification algorithm is proposed, which employ a forward analysis procedure instead of matrix inversion (Shuai et al, 2016). The matrix relation shown in Equation (5-8) is exploited to develop a pre-screening scheme by comparing the admittance change vector with the columns of the sensitivity matrix. Such comparison can yield a small number of location candidates and severity estimations of the fault. Then the Bayesian inference framework is applied to identify the actual fault location and severity within the much reduced fault parameter space. Based on this work, a new fault identification algorithm, which combines the pre-screening procedure and the Bayesian inference framework, is proposed in this research. When conducting SHM, we usually aim at early detection of structural fault. In such a case, the probability of multiple faults occurrence is normally significantly lower than that of single fault occurrence. Therefore, here in this research we assume single fault occurrence. The situation with multiple faults will be studied in the future. Under this assumption, mathematically, only one element in the fault index vector **D** will be non-zero. The fault identification procedure is summarized as follows.

1) We start from treating each segment as potential fault location candidate, and compute an *estimated* fault index for the *k*-th segment that is defined as

$$D_k^{\text{est}} = \text{mean}\left(\frac{\mathbf{\Delta}Y(\omega_j)}{s_{jk}}\right) \qquad (k = 1, \cdots, m) \tag{5-11}$$

Where $\mathbf{\Delta}Y$ is the measured admittance changes, s_{jk} is the element of the *k*-th column of sensitivity matrix. If for a certain *k*, D_k^{est} is less than 0, we can conclude that fault cannot occur at this *k*-th segment (since an actual fault index cannot be smaller than 0).

2) We then employ the Bayesian inference to identify the fault location. The Bayesian inference approach is built upon the Bayes theorem (Katafygiotis and Beck, 1998a),

$$P(\mathbf{D}_i \mid y) = \frac{P(y \mid \mathbf{D}_i) P(\mathbf{D}_i)}{\sum_{j=1}^{N} P(y \mid \mathbf{D}_j) P(\mathbf{D}_j)} \tag{5-12}$$

Variable *y* represents the observations we have. $\mathbf{D}_i$ represents the *i*-th sample of the fault index vector. $P(\mathbf{D})$ is the prior distribution function of $\mathbf{D}$ representing our prior knowledge of the fault index vector. $P(y \mid \mathbf{D}_i)$ is the probability that we observe *y* if $\mathbf{D}_i$ represents the true fault index vector. $P(\mathbf{D}_i \mid y)$ is the posterior probability of $\mathbf{D}_i$ given the observation *y*. Moreover, we use the directionality between the measured admittance change and model prediction as the observation *y* which can be formulated as (Tang, 2005),

$$y(\mathbf{D}_i) = \arcsin\left(\frac{(\mathbf{S}_{n\times m}\mathbf{D}_i)^T \Delta\mathbf{Y}}{\left|\mathbf{S}_{n\times m}\mathbf{D}_i\right| \cdot \left|\Delta\mathbf{Y}\right|} - 1\right) \tag{5-13}$$

where $\mathbf{S}_{n\times m}\mathbf{D}_i$ is the predicted admittance change vector under fault parameter sample $\mathbf{D}_i$ ($\mathbf{S}_{n\times m}$ is the sensitivity matrix), and $\Delta\mathbf{Y}$ is the measured admittance change vector. If $\mathbf{S}_{n\times m}\mathbf{D}_i$ and $\Delta\mathbf{Y}$ are the same, the directionality will be 0. Larger difference in these two vectors leads to larger value of the similarity index $y(\mathbf{D}_i)$. Based on the Bayes theorem, a simple parameter estimation method would be to compute

the posterior probability $P(\mathbf{D}|y)$ for all the possible values of the fault index vector $\mathbf{D}$ and then select the value with the highest posterior probability as the estimated value. Furthermore, if the prior probability $P(\mathbf{D})$ is selected as the uniform distribution, which reflects that we do not have specific prior knowledge on the fault location and severity within the feasible range, then the ranking of the posterior probability for different values of $\mathbf{D}$ is solely determined by $P(y|\mathbf{D}_i)$. Thus, the key step in Bayesian inference is the formulation and calculation of the likelihood function $P(y|\mathbf{D}_i)$ that is used to evaluate the agreement between the measurements and model prediction under sampled fault parameters. The likelihood function is then formulated as a normal distribution of fault parameters with respect to the measurement data (Katafygiotis and Beck, 1998a; Zhou and Tang, 2016),

$$P(y_m|\mathbf{D}) = \frac{1}{\sigma\sqrt{2\pi}} e^{-\frac{[y(\mathbf{D})-y_m]^2}{2\sigma^2}} \tag{5-14}$$

$$y_m = y(\mathbf{D}_{\text{act}}) + \varepsilon \tag{5-15}$$

where $P(y_m|\mathbf{D})$ is the probabilistic distribution function obtained through sampling **D**, the fault index vector, over the sample space, σ is the standard deviation of the directionality due to measurement noise. y_m is the directionality based on measurement which can be expressed as shown in Equation (5-15), where $y(\mathbf{D}_{\text{act}})$ represents the model response under actual fault parameter $\mathbf{D}_{\text{act}}$, and ε is due to measurement error. $y(\mathbf{D}_{\text{act}})$ should be zero according to Equation (5-13), and thus y_m will be zero under ideal situation (i.e., without measurement error). In reality, however, measurement noise and model uncertainty always exists and therefore y_m may not be 0. Equation (5-14) indicates that a larger likelihood function value will be produced when sampled admittance change is closer to the measured admittance change, based on which the fault parameters can be quantitatively analyzed in a probabilistic manner.

The fault identification is facilitated through comparison of model predictions and experimental measurements, then the identification performance is highly depended on the model accuracy. However,

the discrepancies between model prediction and experimental measurements are inevitable. From the proposed new algorithm, we can find that only the sensitivity matrix is explicitly involved into the fault identification procedure. If we can build the sensitivity matrix directly from experimental measurements, we may not only bypass the onerous job of building an accurately finite element model, but also intuitively avoid the discrepancies between the mathematic model prediction and the experimental measurement.

5.3.2 Sensitivity matrix building by experimental measurements and Gaussian process

From Section 5.3.1, we can observe that the *i*-th column of the sensitivity matrix actually represents the admittance changes induced by a unit fault (unit mass increase or unit stiffness reduction) in the *i*-th segment. This inspires the idea to experimentally built the sensitivity matrix. First, the monitored structure is divided into a group of segments, and each of them is treated as a possible location of fault occurrence. Then a small test mass, which will cause a local mass density increase D_t, is attached on the *i*-th segment. The admittance changes $\Delta\mathbf{Y}_i^{\exp}$ are measured at multiple frequency points. Then the *i*-th column $\mathbf{S}_i$ of the sensitivity matrix can be approximated by dividing the admittance change vector $\Delta\mathbf{Y}_i$ with the known mass density increase D_t.

$$\mathbf{S}_i = \frac{\Delta\mathbf{Y}_i^{\exp}}{D_t} \tag{5-16}$$

Attach the mass onto each segment of the monitored structure and repeat this process, we can experimentally obtain the entire sensitivity matrix. As you can see, no mathematic model is needed to extract the sensitivity matrix in the new procedure. Then the discrepancies between the mathematic model predictions and experimental measurements can be intuitively avoided. However, the new algorithm also poses a new challenge here. Since we usually aim at early detection of structural fault, which implies that the size of fault is small in general. Then in order to accurately localize the fault, the structure is divided into a large number of segments. For each segment, we need to attach the test mass and measure the admittance change information. It will be a huge workload to repeat the experiment and collect all the

experimental data. What's worse, some parts of a complex structure are even not accessible due to its complex configuration. At the same time, the measurement noise may be another barrier to prevent this new method in real word application. In order to overcome these limitations, the Gaussian process for regression is introduced here.

Gaussian processes are a data-based approach by which various spatial and temporal problems can be modeled. There has been a rich research literature on regression using Gaussian processes (Kennedy and O'Hagan, 2000; Rasmussen and Williams, 2006; DiazDelaO and Adhikari, 2010; Zhou et al, 2016). The basic idea behind Gaussian process is to extend the discrete multivariate distribution on a finite dimensional space to a random function defined on an infinite-dimensional space. As defined in the preceding section, the element of the sensitivity matrix s_{kj} is represented by a function $s_{kj} = f(\mathbf{x})$, where $\mathbf{x} = [\omega_k, L_j]$, ω_k is the frequency and L_j is the assumed fault location. Assume we have n known input-output relations (input $\mathbf{X}(\mathbf{x}_1, \mathbf{x}_2, \cdots \mathbf{x}_n)$, output $\mathbf{s}_{kj}(s_{kj,1}, s_{kj,2}, \cdots s_{kj,n})$). It is straightforward to predict the sensitivity $\mathbf{s}_{kj}^*$ over the target inputs $\mathbf{X}^*$, if the distribution of the corresponding observed sensitivity $\mathbf{s}_{kj}$ is assumed to be a multivariate Gaussian for any set of input points $\mathbf{X}$. The multivariate Gaussian distribution of a discrete subset of the range of the function can be extended to its entire range. Thus, the multivariate Gaussian distribution for a finite-dimensional case is generalized to an infinite-dimensional case. The function $s_{kj} = f(\mathbf{x})$ with the generalized Gaussian distribution of infinite dimensionality over its domain is referred to as a Gaussian process. The observed data set ($\mathbf{s}_{kj}$, $\mathbf{X}$) is presented in the standard form of the multivariate Gaussian distribution which is symbolically expressed as

$$\mathbf{s}_{kj} \sim N(\boldsymbol{\mu}(\mathbf{X}), \boldsymbol{\Sigma}(\mathbf{X}, \mathbf{X})) \tag{5-17}$$

where $\boldsymbol{\mu}$ and $\boldsymbol{\Sigma}$ represent the mean vector and covariance matrix, which respectively are defined as

$$\boldsymbol{\mu}(\mathbf{X}) = \begin{bmatrix} m(\mathbf{x}_1) & m(\mathbf{x}_2) & \ldots & m(\mathbf{x}_n) \end{bmatrix}^T \tag{5-18}$$

$$\boldsymbol{\Sigma}(\mathbf{X},\mathbf{X}) = \begin{bmatrix} k(\mathbf{x}_1,\mathbf{x}_1) & k(\mathbf{x}_1,\mathbf{x}_2) & ... & k(\mathbf{x}_1,\mathbf{x}_n) \\ k(\mathbf{x}_2,\mathbf{x}_1) & k(\mathbf{x}_2,\mathbf{x}_2) & ... & k(\mathbf{x}_n,\mathbf{x}_n) \\ .. & .. & .. & .. \\ k(\mathbf{x}_n,\mathbf{x}_1) & k(\mathbf{x}_n,\mathbf{x}_2) & ... & k(\mathbf{x}_n,\mathbf{x}_n) \end{bmatrix} \tag{5-19}$$

$m(\mathbf{x}_i)$ is the assumed mean function which returns the expected value of sensitivity $\mathbf{s}_{kj}$. $k(\mathbf{x}_i,\mathbf{x}_j)$ is the assumed covariance function which relates the sensitivity observed at $\mathbf{x}_i$ and $\mathbf{x}_j$. Since the fundamental assumption is that any set of the outputs of the system follows the multivariate Gaussian distribution, the predicted $\mathbf{s}_{kj}^*$ over the target input points $\mathbf{X}^*$ can be presented together with the observed data points in the standard form,

$$\begin{bmatrix} \mathbf{s}_{kj} \\ \mathbf{s}_{kj}^* \end{bmatrix} \sim N\left(\begin{bmatrix} \boldsymbol{\mu} \\ \boldsymbol{\mu}^* \end{bmatrix}, \begin{bmatrix} \boldsymbol{\Sigma} & \boldsymbol{\Sigma}^* \\ \boldsymbol{\Sigma}^* & \boldsymbol{\Sigma}^{**} \end{bmatrix}\right) \tag{5-20}$$

where $\boldsymbol{\mu}^*$ is the mean vector with respect to the predicted sensitivity $\mathbf{s}_{kj}^*$, $\boldsymbol{\Sigma}^*$ is the sub-covariance matrix of the observed $\mathbf{s}_{kj}$ and the predicted $\mathbf{s}_{kj}^*$, and $\boldsymbol{\Sigma}^{**}$ is the sub-covariance matrix of the predicted $\mathbf{s}_{kj}^*$. It can be shown that the probability distribution of the predicted sensitivity values $\mathbf{s}_{kj}^*$ over the target input points $\mathbf{X}^*$ conditional on the data set ($\mathbf{s}_{kj}$, $\mathbf{X}$) is also a multivariate Gaussian (Rasmussen and Williams, 2006)

$$\mathbf{s}_{kj}^* \mid \mathbf{X}^*, \mathbf{s}_{kj}, \mathbf{X} \sim N(\boldsymbol{\mu}^* + \boldsymbol{\Sigma}^{*T}\boldsymbol{\Sigma}^{-1}(\mathbf{s}_{kj} - \boldsymbol{\mu}), \boldsymbol{\Sigma}^{**} - \boldsymbol{\Sigma}^{*T}\boldsymbol{\Sigma}^{-1}\boldsymbol{\Sigma}^*) \tag{5-21}$$

As you can see, the Gaussian process is fully specified by the mean function $m(\mathbf{x}_i)$ and the covariance function $k(\mathbf{x}_i,\mathbf{x}_j)$. A wide body of conventionally used mean and covariance functions can be found in the literature (Rasmussen and Williams, 2006). The selection of mean and covariance functions will be discussed in the following case study.

5.4 Simulation Case Studies

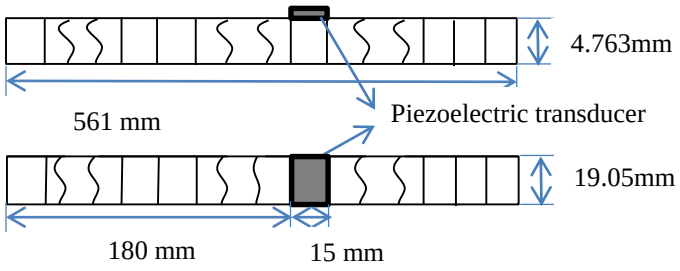

Figure 5-1. Case study setup.

In this section, we conduct case analysis using simulated data first, in order to highlight the effectiveness of the proposed approach. We intend to identify the fault location and severity of an aluminum cantilever beam. The dimension of the beam is specified as: length 0.561 m, width 0.01905 m, and thickness 0.004763 m. The mass density and Young's modulus are, respectively, 2700 kg/m^3 and 68.9 GPa . A piezoelectric transducer is attached onto the beam as shown in Figure 5-1. The dimension of the transducer is: length 0.015 m, width 0.01905 m, and thickness 0.0014 m. The Young's moduli are $Y_{11} = 86$ GPa and $Y_{33} = 73$ GPa , the mass density is 9500 kg/m^3 , and the piezoelectric constant and impermittivity constant are, respectively, $h_{31} = -1.0288 \times 10^9$ V/m and $\beta_{33} = 1.3832 \times 10^8$ m/F . The piezoelectric transducer is placed at 0.18 m from the fixed end of the beam, and covers the entire width. The beam is divided into 375 segments and each segment is a possible fault location. A finite element model is employed to analysis the coupled system and measure the admittance of the piezoelectric transducer. The admittance information is collected around peaks corresponding to 20th, 23rd and 27th beam resonance (3781.9 Hz, 4526.9 Hz and 6213.1 Hz). The admittance values at 100 frequency points around each resonant frequency are employed in the analysis.

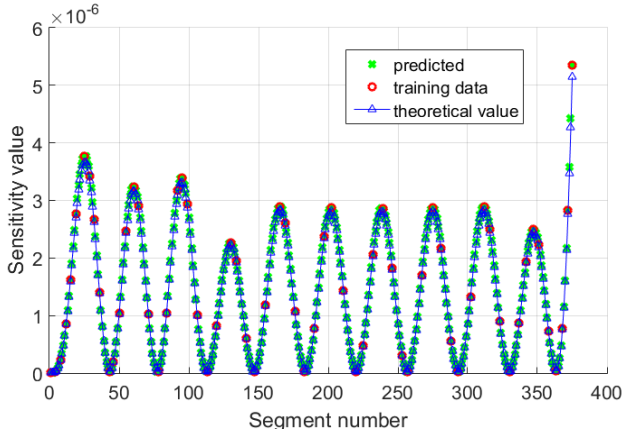

(a) around 20th natural frequency

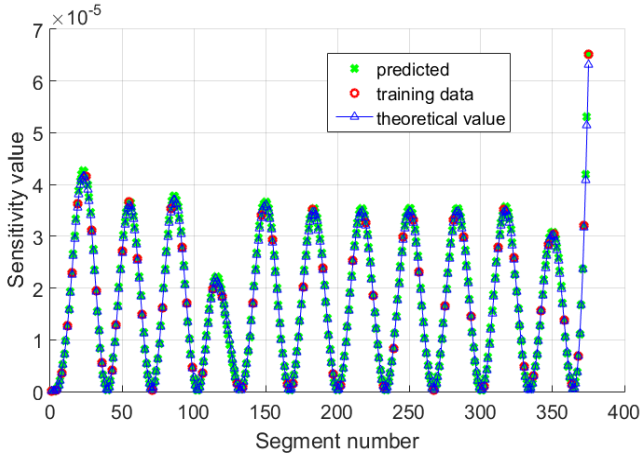

(b) around 23rd natural frequency

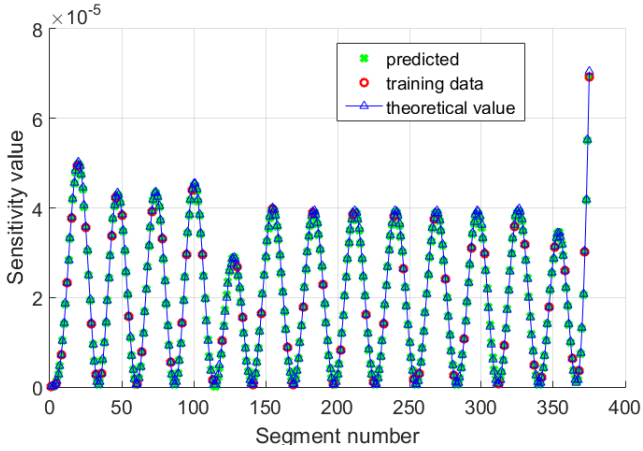

(c) around 27th natural frequency

Figure 5-2. Observed sensitivity and predicted sensitivity

At first, the admittance changes are derived by assuming a small mass density increase in some segments. In other words, the sensitivity values are obtained at some locations first by Equation (5-16). Use the observed sensitivities as the training data, the sensitivity values at other segments then can be predicted by Gaussian process. So only the fault location, which is represented by segment number, is considered as the input variable for the Gaussian process at one frequency point in this case study. Then the goal of Gaussian process is to model the sensitivity as a function of the fault location which is a 1-D modeling problem. At first, the theoretical sensitivity matrix is derived by the finite element analysis to give us some insights into the way we choose the mean function and the covariance function for the Gaussian process. Figure 5-2 shows the sensitivity around the 20th beam resonance. From Figure 5-2, we can observe that the sensitivity shows periodical property along the beam length direction. At the same time, there are also some small irregularities. Then a fix mean function which is equal to the average value of the observed sensitivity $\mathbf{s}_{kj}$, and a complex covariance function which combines two kinds of simple covariance function are employed here (Rasmussen and Williams, 2006). A periodic covariance function is used to model the overall sensitivity variations. A squared exponential covariance function is employed to allow a decay away from exact periodicity. The mean function and covariance function are finally derived as,

$$m(x_i) = ave(\mathbf{s}_{kj}) \tag{5-22}$$

$$k(x_i, x_j) = \theta_1^2 \exp(-\frac{(x_i - x_j)^2}{2\theta_2^2} - \frac{2\sin^2(\pi(x_i - x_j)/T)}{\theta_3^2}) + \sigma_n^2 \delta_{ij} \tag{5-23}$$

Where $[\theta_1, \theta_2, \theta_3, T]$ are the hyperparameters. θ_1 gives the magnitude, θ_2 the decay-time for the periodic component, θ_3 the smoothness of the periodic component and T the period. σ_n represents the noise variance. δ_{ij} is the Kronecker delta. The unknown hyperparameters are suggested to be optimized by maximizing the logarithm of the marginal likelihood (Kennedy and O'Hagan, 2000).

$$\log P(\mathbf{s}_{kj} \mid \mathbf{X}, m, k) = -\frac{1}{2}(\mathbf{s}_{kj} - \boldsymbol{\mu}(\mathbf{X}))^T \boldsymbol{\Sigma}^{-}(\mathbf{s}_{kj} - \boldsymbol{\mu}(\mathbf{X})) - \frac{1}{2}\log|\boldsymbol{\Sigma}| - \frac{n}{2}\log 2\pi \tag{5-24}$$

At one frequency point, the admittance changes are derived by assuming 1% mass density increase in 64 segments (the corresponding segment numbers are 1, 4, 8, 12, 15, 19, 25, 29, 32, 36, 43, 46, 50, 55, 61, 64, 71, 78, 84, 92, 95, 99, 106, 113, 120, 130, 134, 141, 147, 155, 165, 169, 176, 183, 190, 197, 202, 211, 220, 225, 232, 239, 246, 253, 257, 267, 275, 281, 288, 293, 302, 312, 316, 323, 330, 337, 342, 347, 351, 358, 363, 368, 372, 375 respectively). Then the 64 sensitivity values are used as the training data for Gaussian process to predict the other 311 sensitivity values. No measurement noise is considered here ($\sigma_n = 0$). The 'simulannealbnd' function in MATLAB, which use the simulated annealing algorithm, is

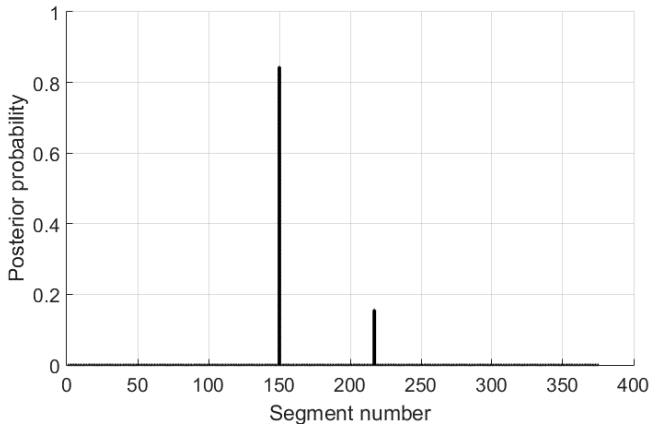

Figure 5-3. Posterior probability of fault location in first fault case

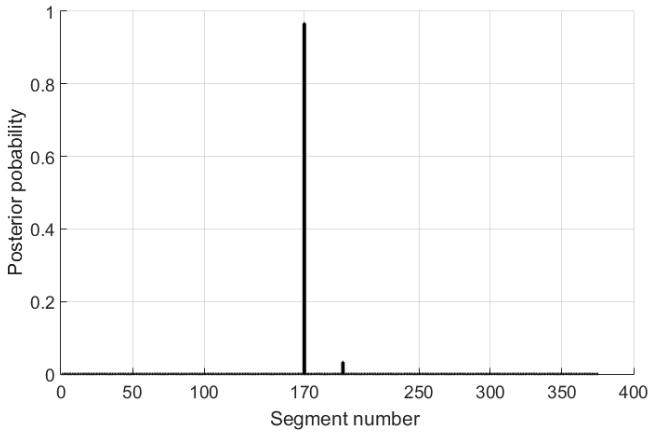

Figure 5-4. Posterior probability of fault location in second fault case

employed to obtain the optimized hyperparameters by minimizing the negative log marginal likelihood. After the mean function and covariance function are determined, the probability distribution of the sensitivity can be predicted by Equation (5-21). Figure 5-2 shows the mean of predicted sensitivity around the peak frequencies. We can observe that the mean values of the predicted sensitivity are very close to the theoretical values from finite element analysis. By repeating the Gaussian process at all the frequency points that we are interested in, we can derive the probability distribution of the sensitivities that we need. Then the mean values of the predicted sensitivity are employed to form the sensitivity matrix. Two fault cases are used to illustrate the accuracy of the predicted sensitivity matrix. For the first case, the fault is located in the 150^{th} segment and the fault severity is assumed as 0.8% mass density increase. For the second case, the fault is located in the 170^{th} segment and the fault severity is assumed as 0.9% mass density increase. The admittance curves for the fault cases are simulated by the finite element analysis. Following the procedure defined in Section 5.3.1, the Bayesian inference gives the posterior probability of the fault location as shown in Figure 5-3 and Figure 5-4. We can observe that the actual fault location, 150^{th} segment for the first case and 170^{th} segment for the second case, have the highest posterior probability which is also much higher than the probability of other locations. So we can conclude that the fault is occurred in150^{th} segment in first case and in 170^{th} segment in second case. By comparing the admittance change curves and the corresponding column of the sensitivity matrix, we also can estimate the fault severity by using Equation (5-11). For the first case, the estimated fault severity in 150^{th} segment is about 0.809%. And the estimated fault severity in 170^{th} segment is about 0.895% for the second case. The estimated fault severity is also very close to the actual value. From the simulated case study, we can find that the proposed algorithm can accurately predict the sensitivity matrix by Gaussian process when only a small number of measurements are available. The proposed fault identification procedure can also precisely pinpoint the fault location and estimate the fault severity.

5.6 Concluding Remarks

In this research, a new fault identification algorithm is formulated for piezoelectric impedance/admittance-based structural health monitoring. First, some elements of the sensitivity matrix are extracted from experimental measurements. Then the whole sensitivity matrix is predicted by Gaussian process. After that, the Bayesian inference framework is employed to identify the fault location and severity by comparing the admittance change vector with the columns of the sensitivity matrix. Our case studies indicate that the new approach can efficiently and accurately identify fault occurrence.

Chapter 6 Conclusion and Future Work

Structural health monitoring is an essential practice in engineering, which aims at detection and identification of fault location/severity/type. The impedance-based structural health motoring, which features high detection sensitivity, easy integration and large detection/monitoring range, has shown some promising aspects. In this dissertation research, a series of effective algorithms are developed and performed for the impedance-based structural health monitoring. Four research tasks are presented and the preliminary analyses have shown promising results, which validates the feasibility of those algorithms.

The first contribution is to develop the mathematical model of a magnetic transducer used in impedance-based structural fault detection. Indeed, there have been efforts on the mathematical modeling of magneto-mechanical interaction between a magnetic transducer and the structure. However, a common drawback of current modeling methods is that experimental testing is required to extract key parameters. Since these parameters are lift-off distance dependent, a large database would need to be established for a given magnetic transducer, to record these parameters under different lift-off distance values. In order to overcome current limitation, an accurate mathematical model of the magnetic transducer interacting with the structure is developed in Chapter 2, in which the dynamic interaction due to magneto-mechanical coupling is explicitly expressed as a function of the lift-off distance. The particular magnetic transducer consists of a coil inserted with a permanent magnetic known as an EMAT. As the magneto-mechanical coupling is lift-off distance-dependent, our focus is on the capability of directly predicting impedance response under given lift-off distance. A key hypothesis made is that the eddy current induced by the coil, that forms closed circular loops in the structure, will act as flowing in fictitious coils embedded in the structure with different radii. Building upon this hypothesis, a complete mathematical model describing the sensor-structure interaction is formulated which includes the mutual inductance prediction under given lift-off distance. As the lift-off distance between the transducer and the structure can be easily measured in practice, this modeling strategy will provide the predictive capability in model-based fault detection and

identification. It will further help elucidate the underlying physics in sensor-structure interaction and yield guidelines for impedance sensor optimization.

The second contribution is to propose a new data analysis approach of transformed impedance that is immune to the lift-off distance oscillation during measurements. The non-contact feature is a potential advantage of the magnetic transducer. However, it also induces an important issue which is the so called lift-off distance oscillation. The coupling between the magnetic transducer and the structure is significantly influenced by the lift-off distance which may be subject to oscillation induced by environmental disturbances. The lift-off distance variation can also alter the impedance of the transducer, which will be appeared as the noise effect and may bury the impedance changes induced by the fault. The problem, furthermore, appears to be actually more challenging for fault identification. In model-based approach, the lift-off distance is needed as input information for the model to compute or predict the transducer impedance. Thus a high precision displacement sensor would be needed to accurately record the exact lift-off distance at every single frequency point during impedance measurements. In data-oriented approach, an extremely large database would be required in order to calibrate the impedance measured under different lift-off distances at each frequency point. This requires precisely measure and record the baseline impedance information in advance at all possible lift-off distances and also requires the accurate measurement of lift-off distance during fault detection. In Chapter 3, a new lift-off effect compensation method based on data analysis is proposed. This approach is based on the research discovery in Chapter 2, in which the relation between both the imaginary part and real part of transducer impedance and the lift-off distance is explicitly identified. The new method uses a scale factor to transform the transducer impedance. A properly chosen scale factor can make the transformed impedance immune to the lift-off variation. It is illustrated that this scale factor can be a constant which is determined by the electrical properties of the magnetic transducer and the structure, the initial given lift-off distance and the interested frequency range. Since the scale factor is independent of the lift-off oscillation, there is no need to measure and record the lift-off distances throughout measurements.

The third contribution is to formulate an efficient fault identification algorithm for piezoelectric impedance/admittance based measurement. Currently, the impedance-based fault identification is mainly dependent on the sensitivity matrix inverse-based optimization. However, the inverse problem is underdetermined in most cases, since the useful impedance/admittance information are far less than unknowns. In order to overcome the limitation on such inverse-based fault identification approach, the Bayesian inference framework is introduced which necessitates employing statistical analysis and inference to solve the forward problem instead of the inverse problem. The Bayesian inference is a sampling based method, which requires to generate an associated database by repeated evaluation for each updated model with respect to each parameter sample. However, the size of the parameter space is generally huge. Because there are too many possible fault locations and fault severity scenarios, it will need extremely high computational cost. In Chapter 4, a new fault identification approach is developed by using piezoelectric impedance sensing, which combine inverse sensitivity formulation and the Bayesian inference technique. First, a prescreening scheme is devised by taking advantage of the mathematical relation between the sensitivity matrix and the impedance measurements in the presence of structural fault. Instead of directly inverting the sensitivity matrix, we employ the sensitivity matrix to conduct a pre-screening by comparing the admittance change vector with the columns of the sensitivity matrix. Indeed, when a structural fault occurs, the impedance change vector in theory must be proportional to a column vector of the sensitivity matrix, and the ratio between these two vectors represents the fault severity. While the actual result may be complicated by measurement noise and uncertainties, this feature can reduce dramatically the size of the parameter space involved in Bayesian inference. We then apply the Bayesian inference framework to identify the actual fault location and severity within the much reduced fault parameter space. The case studies indicate that the new approach can efficiently and accurately identify fault occurrence.

However, there are still remaining works to accomplish systematically. In an earlier study, a tunable inductor is integrated into the low cost measurement circuit, which is serially connected with the resistor element, to improve fault detection performance (Wang and Tang 2009b). It has been demonstrated that,

with the proper tuning of the inductance value, the magnitude of the circuitry admittance can be significantly amplified, which yields much increased signal-to-noise ratio in the sensor measurement. The induced inductance will add another degree of freedom into the coupled system and can introduce additional resonant frequencies at arbitrary frequency bands. By tuning the inductance to different values, a family of impedance/admittance information can be obtained. This is helpful to increase the useful impedance/admittance information (J Zhao et al, 2008). However, the inductance is intuitively tuned to make the resonant frequency of the circuit close to the structural resonant frequency. So it is essential to find a way to theoretically guide how to adjust the inductance to achieve better fault detection and identification performance.

Bibliography

Annamdas, V.G., and Radhika, M.A., 2013, "Electromechanical impedance of piezoelectric transducers for monitoring metallic and non-metallic structures: A review of wired, wireless and energy-harvesting methods," Journal of Intelligent Material Systems and Structures, V24, 1021-1042.

Antoni, J., Fessel, P., and Zhang, E.L., 2011, "A comprehensive Bayesian approach for model updating and quantification of modeling errors," Probabilistic Engineering Mechanics, V26, 550-560.

Auld, B.A., and Moulder, J.C., 1999, "Review of advances in quantitative eddy current nondestructive evaluation," Journal of Nondestructive Evaluation, V18, 3-26.

Beck, J.L., and Au, S.K., 2002, "Bayesian updating of structural models and reliability using Markov chain Monte Carlo simulation," Journal of Engineering Mechanics, V128, 380-391.

Beck, J.L., and Katafygiotis, L.S., 1998, "Updating models and their uncertainties. I: Bayesian statistical framework," Journal of Engineering Mechanics, V124, 455-461.

Becker, W., Oakley, J.E., Surace, C., Gill, P., Rowson, J., and Worden, K., 2012, "Bayesian sensitivity analysis of a nonlinear finite element model," Mechanical Systems and Signal Processing, V32, 18-31.

Brauer, J.R., 2006, Magnetic Actuators and Sensors, John Wiley & Sons.

Ching, Jianye and Beck, James L., 2004, "New Bayesian model updating algorithm applied to a structural health monitoring benchmark," Structural Health Monitoring, V3, 313-332.

Cheng, D.K., 1992, Field and Wave Electromagnetics, Addison-Wesley.

DiaDelaO, F.A., and Adhikari, S., 2012, "Bayesian assimilation of multi-fidelity finite element models," Computers and Structures, V92-93, 206-215.

Dixon, S., and Palmer, S.B., 2004, "Wideband low frequency generation of Rayleigh and Lamb waves using electromagnetic acoustic transducers," Ultrasonics, V42, 1129-1136.

Dominique, P., and Isabelle, D., 1997, “Eddy current sensors for nondestructive inspection of graphite composite materials,” NDT and E International, V30, 1676-1682.

Giguere, S., Lepine, B.A. and Dubois, J.K.S., 2001, “Pulsed eddy current technology: characterizing material loss with gap and lift-off variations,” Research in Nondestructive Evaluation, V13, 119-129

Giurgiutiu, V., 1999, “Experimental investigation of E/M impedance health monitoring for spot-welded structural points,” Journal of Intelligent Material Systems and Structures, V10, 802-812.

Giurgiutiu, V., 2005, “Tuned Lamb wave excitation and detection with piezoelectric wafer active sensors for structural health monitoring,” Journal of Intelligent Material Systems and Structures, V16, 291-305.

Hashizume, H., Yamada, Y., Miya, K., Toda, S., Morimoto, K., Araki, Y., Satake, K., and Shimizu, N., 1992, “Numerical and experimental analysis of eddy current testing for a tube with cracks,” IEEE Transactions on Magnetics, V28, 1469-1472.

Hoshikawa, H. and Koyama, K., 2001, “A new eddy current surface probe without lift-off noise,” Review in Progress Quantitative NDE, V20A, 969-976

Huang, S.L., Zhao, W., Zhang, Y.S., and Wang, S., 2009, “Study on the lift-off effect of EMAT,” Sensors & Actuators: A Physical, V153, 218-221.

Javier, G.M., Jaime, G.G., and Emesto, V.S., 2011, “Non-destructive techniques based on eddy current testing,” Sensors, V11, 2525-2526.

Jian, X., Dixon, S., Edwards, R.S., and Morrison, J., 2006, “Coupling mechanism of an EMAT,” Ultrasonics, V44, E653-E656.

Jiang, L. J., Tang, J., and Wang, K. W., 2006, “An enhanced frequency-shift-based damage identification method using tunable piezoelectric transducer circuitry,” Smart Materials and Structures V15, 799-808.

Junior, C.D.M., Erturk, A., and Inman, D.J., 2009, “An electromechanical finite element model for piezoelectric energy harvester plates,” Journal of Sound and Vibration, V327, 9-25.

Katafygiotis, L.S., and Beck, J.L., 1998a, "Updating models and their uncertainties. I: Bayesian statistical framework," Journal of Engineering Mechanics, V124, 455-461.

Katafygiotis, L.S., and Beck, J.L., 1998b, "Updating models and their uncertainties. II: Model identifiability," Journal of Engineering Mechanics, V124, 463-467.

Kim, J., and Wang, K.W., 2014, "An enhanced impedance-based damage identification method using adaptive piezoelectric circuitry," Smart Materials and Structures, V23, 095041.

Koduru, J.P., and Rose, J.L., 2013, "Transducer arrays for omnidirectional guided wave mode control in plate like structures," Smart Material and Structures, V22, 015010.

Lefebvre, J.H.V. and Mandache, C., 2006, "Pulsed eddy current measurement of lift-off," AIP Conference Proceedings, V820, 669-676

Madhav, A.V.G., and Kiong, S.C., 2010, "Application of electromechanical impedance technique for engineering structures: review and future issues," Journal of Intelligent Material Systems and Structures, V21, 41-59.

Mandache, C., and Lefebvre, J.H.V., 2006, "Transient and harmonic eddy currents: lift-off point of intersection," NDT and E International, V39, 57-60.

Min, J., Park, S., Yun, C.B., Lee, C.G., and Lee, C., 2012, "Impedance-based structural health monitoring incorporating neural network technique for identification of damage type and severity," Engineering Structures, V39, 210-220.

Moore, E.Z., Murphy, K.D. and Nichols, J.M., 2011, "Crack identification in a freely vibrating plate using Bayesian parameter estimation," Mechanical Systems and Signal Processing, V25, 2125-2134.

Morrison, J.P., Dixon, S., Potter, M.D.G. and Jian, X., 2006, "Lift-off compensation for improved accuracy in ultrasonic lamb wave velocity measurements using electromagnetic acoustic transducers (EMATs)," Ultrasonics, V44, E1401-E1404

Mottershead, J.E., and Friswell, M.I., 1993, “Model updating in structural dynamics: a survey,” Journal of sound and vibration, V167, 347-375.

Mthembu, L., Marwala, T., Friswell, M.I., and Adhikari, S., 2011, “Model selection in finite element model updating using the Bayesian evidence statistic,” Mechanical System and Signal Processing, V25, 2399-2412.

Naidu, A., and Soh, C., 2004, “Identifying damage location with admittance signatures of smart piezo-transducers,” Journal of Intelligent Material Systems and Structures, V15, 627-642

Naidu, A., Soh, C., and Pagalthivarthi, K., 2006, "Bayesian network for E/M impedance-based damage identification," Journal of Computing in Civil Engineering, V20, 227-236.

Park, G., Kabeya, K., Cudney, H.H., and Inman, D.J., 1999, “Impedance-based structural health monitoring for temperature varying applications,” JSME Internal Journal Series A-Solid Mechanics and Material Engineering, V42, 249-258.

Park, G., Farrar, C.R., Rutherford, A.C., and Robertson, A.N., 2006, “Piezoelectric active sensor self-diagnostics using electrical admittance measurements,” ASME Journal of Vibration and Acoustics, V128, 469-476.

Park, G., Sohn, H., Farrar, C.R., and Inman, D. J., 2003, “Overview of piezoelectric impedance-based health monitoring and path forward,” The Shock and Vibration Digest, V35, 451-463.

Park, S., Yun, C.B. and Inman, D.J., 2008. “Structural health monitoring using electro‐mechanical impedance sensors,” Fatigue & Fracture of Engineering Materials & Structures, V31, 714-724.

Peairs, D. M., Inman, D.J., and Park, G., 2007, “Circuit analysis of impedance-based health monitoring of beams using spectral elements,” Structural Health Monitoring, V6, 81-94.

Raju, V., Park, G., and Cudney, H.H., 1998, “Impedance-based health monitoring technique of composite reinforced structures,” Proceedings of the Ninth International Conference on Adaptive Structures and

Technologies, 448-457.

Rosado, L.S., Janeiro, F.M., Ramos, P.M., and Piedade, M., 2013, "Defect characterization with eddy current testing using nonlinear-regression feature extraction and artificial neural networks," IEEE Transactions on Instrumentation and Measurement, V62, 1207-1214.

Rose, J. L., 1995, "Recent advances in guided wave NDE," Proceedings of IEEE Ultrasonics Symposium, 761-770.

Shu, L., Songling, H., Wei, Z., Peng, Y., 2008, "Improved immunity to lift-off effect in pulsed eddy current testing with two-stage differential probes," Russian Journal of Nondestructive Testing, V44, 138-144.

Shuai, Q., Liang, G., and Tang, J., 2016, April. "Piezoelectric admittance-based damage identification by Bayesian inference with pre-screening," Proc. SPIE 9799, Active and Passive Smart Structures and Integrated Systems 2016, 97990C (April 15, 2016); doi:10.1117/12.2219159.

Shuai, Q. and Tang, J., 2014, "Enhanced modeling of magnetic impedance sensing system for damage detection," Smart Materials and Structures, V23(2), 025008.

Sinha, J.K., and Friswell, M.I., 2002, "Model updating: a tool for reliable modeling, design modification and diagnosis," The Shock and Vibration Digest, V34, 27-35.

Sodano, H.A., Bae, J.S., Inman, D.J., and Belvin, W.K., 2005, "Concept and model of eddy current damper for vibration suppression of a beam," Journal of Sound and Vibration, V288, 1177-1196.

Sodano, H.A., and Inman, D.J., 2008, "Modeling of a new active eddy current vibration control system," ASME Journal of Dynamics Systems, Measurement and Control, V130, 21009.

Standards Committee of the IEEE Ultrasonics, Ferroelectrics, and Frequency Control Society, 1987, An American National Standard: IEEE Standard on Piezoelectricity The Institute of Electrical and Electronics Engineers, ANSI/IEEE Std176-1987, New York.

Tang, J., 2005, "Frequency response based damage detection using principal component analysis," IEEE

International Conference on Information Acquisition.

Tang, J., and Wang, K.W., 2001, "Active–passive hybrid piezoelectric networks for vibration control: comparisons and improvement," Smart Materials and Structures, V10, 794-806.

Tian, G.Y. and Sophian, A., 2005, "Reduction of lift-off effects for pulsed eddy current NDT," NDT & E International, V38, 319-324.

Thomas, S., Obayya, S.S.A., Taneja, R., and Balachandran, W., 2009, "A coupled electromagnetic and mechanical analysis of electromagnetic acoustic transducers," International Journal for Computational Methods in Engineering Science and Mechanics, V10, 124-133.

Tseng, K.K.-H., and Naidu, A.S.K., 2002, "Non-parametric damage detection and characterization using smart piezoceramic material," Smart Materials and Structures, V11, 317-329.

Vanik, M.W., Beck, J.L., and Au, S., 2000, "Bayesian probabilistic approach to structural health monitoring," Journal of Engineering Mechanics, V126, 738-745.

Wandowski, T., Malinowski,P., and Ostachowicz, W.M., 2011, "Damage detection with concentrated configurations of piezoelectric transducers," Smart Materials and Structures, V20, 025002.

Wang, D., Song, H., and Zhu, H., 2013, "Numerical and experimental studies on damage detection of a concrete beam based on PZT admittances and correlation coefficient," Construction and Building Materials, V49, 564-574.

Wang, HB. and Feng, ZH., 2013, "Ultrastable and highly sensitive eddy current displacement sensor using self-temperature compensation," Sensors and Actuators A-Physical, V203, 362-368.

Wang, X., 2010, Impedance-Based Damage Detection and Identification Enhancements Using Circuitry Effects (Doctorate Dissertation), University of Connecticut.

Wang, X., Lu, Y., and Tang, J., 2008. "Damage detection using piezoelectric transducers and the Lamb wave approach: I. System analysis," Smart Materials and Structures, V17, 025033.

Wang, X. and Tang, J., 2009, “Damage identification using piezoelectric impedance approach and spectral element method,” Journal of Intelligent Material Systems and Structures, V20, 907-921.

Wang, X. and Tang, J., 2010a, “Damage detection using piezoelectric admittance approach with inductive circuitry,” Journal of Intelligent Material Systems and Structures, V21, 667-676.

Wang, X. and Tang, J., 2010b, “An enhanced piezoelectric impedance approach for damage detection with circuitry integration,” Smart Material and Structures, V19, 045001.

Wang, X. and Tang, J., 2012, “Modeling and analysis of magnetic impedance sensor with circuitry integration for damage detection,” Journal of Intelligent Material Systems and Structures, V23, 1799-1812.

Wilcox, P.D., Lowe, M.J.S., and Cawley, P., 2005, “The excitation and detection of Lamb waves with planar coil electromagnetic acoustic transducers,” IEEE Transaction on Ultrasonics, Ferroelectrics and Frequency Control, V52, 2370-2383.

Xia, Y., and Hao, H., 2003, “Statistical damage identification of structures with frequency changes,” Journal of Sound and Vibration, V263, 853-870.

Xu, P., Huang, S.L., and Zhao, W., 2010, “Differential eddy current testing sensor composed of double gradient winding coils for crack detection,” 2010 IEEE Sensors Applications Symposium, 59-63.

Yoon, H.S., Jung, D., and Kim, J.H., 2012, “Lamb wave generation and detection using piezoceramic stack transducers for structural health monitoring applications,” Smart Materials and Structures, V21, 055019.

Yu, L., and Giurgiutiu, V., 2012, “Piezoelectric wafer active sensors in lamb wave-based structural health monitoring,” Journal of the Minerals, Metals & Materials Society, V64, 814-822.

Zagrai, A.N., 2009, “Magneto-mechanical impedance of metallic structures,” The Journal of the Acoustical Society of America, V125, EL1-EL7.

Zagrai, A.N., and Giurgiutiu, V., 2001, “Electro-mechanical impedance method for crack detection in thin plates,” Journal of Intelligent Material Systems and Structures, V12, 709-718.

Zagrai, A.N., and Hakan, C., 2010, “Magneto-mechanical impedance identification and diagnosis of metallic structures,” International Journal of Engineering Science, V48, 888-908.

Zarate, B.A. and Caicedo, J.M., 2008, “Finite element model updating: multiple alternatives,” Engineering Structures, V30, 3724-3730.

Zarate, B.A., Caicedo, J.M., Yu, J., and Ziehl, P., 2012, “Bayesian model updating and prognosis of fatigue crack growth,” Engineering Structures, V45, 2125-2134.

Zhang, E.L., Feissel, P., and Antoni, J., 2011, “A comprehensive Bayesian approach for model updating and quantification of modeling errors,” Probabilistic engineering mechanics, V26, 550-560.

Zhao, J., Tang, J., and Wang, K.W., 2008, “Enhanced statistical damage identification using frequency shift information with tunable piezoelectric transducer circuitry,” Smart Material and Structures, V17, 065003.

Zhou, K., Cao, P., and Tang, J., 2015, “Efficient Uncertainty Quantification in Structural Dynamic Analysis Using Two-Level Gaussian Processes,” Proceedings of ASME 2015 Conference on Mechanical Vibration and Noise, DETC2015-47724.

Zhou, K., Shuai, Q., and Tang, J., 2014, “Adaptive damage detection using tunable piezoelectric admittance sensor and intelligent inference,” Proceedings of ASME 2014 Conference on Smart Materials, Adaptive Structures and Intelligent Systems, SMASIS2014-7624.

Zhou, K., and Tang, J., 2016, “Highly efficient probabilistic finite element model updating using intelligent inference with incomplete modal information,” Journal of Vibration and Acoustics, V138, 051016.

Zhou, W. and Zuo, L., 2012, “Sensitivity-enhanced admittance-based structure health monitoring using a higher-order resonant circuit,” Smart Materials and Structures, V21, 105023.